

VILNIUS GEDIMINAS TECHNICAL UNIVERSITY
INSTITUTE OF MATHEMATICS AND INFORMATICS

Povilas TREIGYS

DEVELOPMENT AND APPLICATION
OF METHODS IN THE GRAPHICAL
OPHTHALMOLOGICAL AND
THERMOVISUAL DATA ANALYSIS

DOCTORAL DISSERTATION

TECHNOLOGICAL SCIENCES,
INFROMATICS ENGINEERING (07T)



LEIDYKLA
VILNIUS TECHNIKA 2010

Doctoral thesis was prepared at Institute of Mathematics and Informatics in 2005–2010

Scientific Supervisors

Prof Dr Habil Gintautas DZEMYDA (Institute of Mathematics and Informatics, Technological Sciences, Informatics Engineering – 07T) (2007–2010),
Prof Dr Habil Vydūnas ŠALTENIS (Institute of Mathematics and Informatics, Technological Sciences, Informatics Engineering – 07T) (2005–2007).

<http://leidykla.vgtu.lt>

VG TU leidyklos TECHNIKA 1735-M mokslo literatūros knyga

ISBN 978-9955-28-540-3

© VG TU leidykla TECHNIKA, 2010

© Treigys, P., 2010

treigys@ktl.mii.lt

VILNIAUS GEDIMINO TECHNIKOS UNIVERSITETAS
MATEMATIKOS IR INFORMATIKOS INSTITUTAS

Povilas TREIGYS

GRAFINIŲ OFTALMOLOGINIŲ IR
TERMOVIZINIŲ DUOMENŲ ANALIZĖS
METODŲ KŪRIMAS IR TAIKYMAS

DAKTARO DISERTACIJA

TECHNOLOGIJOS MOKSLAI,
INFORMATIKOS INŽINERIJA (07T)



LEIDYKLA
VILNIUS TECHNIKA 2010

Disertacija rengta 2005–2010 metais Matematikos ir informatikos institute.

Darbo moksliniai vadovai

prof. habil. dr. Gintautas DZEMYDA (Matematikos ir informatikos institutas, technologijos mokslai, informatikos inžinerija – 07T) (2007–2010),

prof. habil. dr. Vydūnas ŠALTENIS (Matematikos ir informatikos institutas, technologijos mokslai, informatikos inžinerija – 07T) (2005–2007).

Acknowledgement

I sincerely appreciate the help of the scientific supervisors Prof Dr Habil Gintautas Dzemyda and Prof Dr Habil Vydūnas Šaltenis (deceased) for valuable scientific advice and consistent guidance, patience and assistance with research.

I would like to express thanks for thesis reviewers Prof Dr Antanas Leonas Lipeika and Dr Olga Kurasova who have carefully read the thesis and gave valuable advice and critical comments.

I thank the staff and colleagues of Institute of Mathematics and Informatics, Department of Systems Analysis, and the staff of Vilnius College in Higher education for helpful advice and friendly assistance. Great gratitude to Dr Valerijus Barzdžiukas and Dr Vincentas Veikutis for medical background consultation and to Janina Kazlauskaitė for tireless efforts in editing the text.

I sincerely thank my family and friends for their moral support, patience and understanding.

I thank the Lithuanian State Science and Studies Foundation for providing financial support during the preparation of the thesis.

I also thank all the others who directly or indirectly contributed to this work.

Povilas Treigys

Abstract

The dissertation investigates the issues of medical data analysis that can be visualized by optical spectra. The main topics of research include digital recordings of human eye fundus images as well as thermovisual data of cardiac surgery. The purpose of the dissertation is to employ such image analysis methods and algorithms for automated eye fundus image and thermovisual data examination which allows us to follow the changes depending on the problem domain.

The dissertation approaches a few major tasks such as detecting the optic nerve disc in eye fundus images, as well as visualization of the thermal anisotropy zone of the heart tissue during the radiofrequency ablations.

The dissertation consists of Introduction, five sections including Conclusions, References, and 3 Annexes.

The introduction reveals the investigated problem, importance of the thesis and the object of research. It describes the purpose and tasks of the dissertation, research methodology, scientific novelty, the practical significance of the results examined in the paper and defended statements. The introduction ends with the list of author's publications on the subject of the dissertation.

In the first section, a short overview of data mining, pattern recognition and knowledge discovery in terms of medical practice is provided. In addition, the basic means of medical image acquisition are discussed as well.

In the second section, investigation of the eye fundus vasculature is taken into account. Namely, the methods for vasculature elimination from the eye fundus image are presented.

In the third section, the task for optic nerve disc localization and approximation by the elliptical cone is discussed.

In the fourth section, the problem of eye fundus image registration is investigated.

Finally, in the fifth section, the analysis of proposed algorithms is provided. The thermovisual data analysis of cardiac surgery is also presented in this section. The discussion on the tissue anisotropy zone is provided here.

10 articles that focus on the subject of the dissertation are published: 3 publications are included in the Institute of Scientific Information Citation Index Expanded (*ISI Web of Science*) list; 1 publication is printed in the journal that is included in the Institute of Scientific Information Conference (*ISI Proceedings*) list; 1 publication printed in journal approved by Lithuanian Science Council; 5 publications are printed in the national and international conference proceedings. The main results of the work have been presented and discussed at 12 national and international conferences, workshops, seminars.

Reziumė

Disertacijoje nagrinėjami vaizdiniai medicininiai duomenys. Pagrindinė tyrimų sritis yra susijusi su vaizdais gaunamais oftalmologinėje ir kardiochirurginėje praktikoje. Didžiausias dėmesys disertacijoje yra skiriamas akies dugno vaizdų apdorojimui. Yra nagrinėjami tokie objektai kaip akies dugno kraujagyslių tinklas, regos nervo diskas, jo aptikimas bei aproksimavimas kreive. Taip pat antroje disertacijos pusėje pateikiama termovizinių duomenų analizė siekiu identifikuoti širdies audinio anizotropijos zonas veikiant audinį radiodažninėmis abliacijomis.

Įvade atskleidžiama nagrinėjamos problematikos svarba, įvardinamas tyrimų objektas. Aprašomi keliami tikslai bei uždaviniai, mokslo naujumas ir praktinė rezultatų reikšmė.

Pirmasis skyrius skirtas duomenų ir žinių gavybos apžvalgai. Taip pat šiame skyriuje trumpai pateikiami būdai vaizdiniais medicininiais duomenims suformuoti.

Antrame skyriuje nagrinėjami būdai, kurie leidžia automatinio būdu šalinti bei išskirti kraujagyslių struktūras iš akies dugno vaizdų.

Trečias skyrius skirtas regos nervo disko automatinio atpažinimo ir aproksimavimo kreive klausimams nagrinėti.

Ketvirtame skyriuje nagrinėjama akies dugno vaizdų pozicionavimo problema.

Penktame skyriuje pateikiama probleminių sričių duomenų analizė. Taip pat šiame skyriuje atliekama termovizinių duomenų analizė siekiant automatiškai identifikuoti širdies audinių temperatūrinės anizotropijos zonos dinamiką.

Disertaciją sudaro penki skyriai ir literatūros sąrašas. Bendra disertacijos apimtis 108 puslapiai, 57 paveikslai ir 8 lentelės, neįskaitant priedų.

Tyrimų rezultatai publikuoti 10 mokslinių leidinių: 3 straipsniai leidiniuose, įtrauktuose į Mokslinės informacijos instituto (*ISI Web of Science*) sąrašą, 1 straipsnis leidinyje, įtrauktuose į Mokslinės informacijos instituto konferencijos darbų (*ISI Proceedings*) sąrašą, 1 straipsnis Lietuvos mokslų tarybos patvirtintame leidinyje, 5 straipsniai konferencijų pranešimų medžiagoje. Tyrimų rezultatai buvo pristatyti ir aptarti 12-oje respublikinių ir tarptautinių konferencijų ar seminarų.

Notations

Symbols

C_x – Ellipsis centre coordinate along the x axis.

C_y – Ellipsis centre coordinate along the y axis.

E_{Angle} – Ellipsis rotation angle in radians.

E_{Area} – Ellipsis area.

$E_S(x, y)$ – Edge strength at a particular point.

$E_o(x, y)$ – Gradient direction at a particular point.

E_{param} – Vector of cone parameters.

$F_I(x, y)$ – Inverse two-dimensional Fourier transformation at a particular point.

$G_\sigma(x, y)$ – Two-dimensional Gaussian function at a particular point.

$I_j(x, y)$ – Intensity of a particular point in the j th intensity image.

$I_x(x, y)$ – Gradient along the x axis at a particular point.

$I_y(x, y)$ – Gradient along the y axis at a particular point.

R_x – Semi-minor ellipsis axis.

R_y – Semi-major ellipsis axis.

T_i – i th binary image.

$X^{p'}$ – Object in a p' -dimensional space.

Y_i – i th feature vector.

Y^p – Object in a p -dimensional space.

u_i – i th eigen-vector.

$\Theta_X(E_{param})$ – Minimisation function of cone parameters with respect to a set of coordinates.

λ_i – i th eigen-value.

$\mu_j(\tau_i)$ – Intensity mean of the j th class.

$\sigma_B^2(\tau_i)$ – Variance between classes.

τ_i – i th threshold level.

$\{B\}$ – Two-dimensional matrix of intensity values of the blue channel.

$\{C\}$ – Two-dimensional matrix of intensity values of the cyan channel.

$\{G\}$ – Two-dimensional matrix of intensity values of the green channel.

$\{K\}$ – Two-dimensional matrix of intensity values of the black channel.

$\{L\}$ – Two-dimensional matrix of intensity values of the lightness channel.

$\{M\}$ – Two-dimensional matrix of intensity values of the magenta channel.

$\{R\}$ – Two-dimensional matrix of intensity values of the red channel.

$\{Y\}$ – Two-dimensional matrix of intensity values of the yellow channel.

$\{a\}$ – Two-dimensional matrix of intensity values from red to green.

$\{b\}$ – Two-dimensional matrix of intensity values from blue to yellow.

$h(x, y)$ – Discrete approximation of two-dimensional Gaussian function at a particular point.

$B(x, y)$ – Intensity of a particular point in the blue channel.

C – Matrix of constraints.

$C(I, Z)$ – Mathematical morphological closing.

D – Design matrix.

$D(I, Z)$ – Mathematical morphological dilation.

$E(I, Z)$ – Mathematical morphological erosion.

$F(p, q)$ – Discrete two-dimensional Fourier transformation at a particular point.

$F(E_{param}, X)$ – General representation of a cone.

$F(X_i)$ – Algebraic distance from the i th coordinate to a cone.

$G(x, y)$ – Intensity of a particular point in the green channel.

I, A, I_j – Two-dimensional arrays representing an image.

$O(I, Z)$ – Mathematical morphological opening.

$R(x, y)$ – Intensity of a particular point in the red channel.

S – Scatter matrix.

W – Vector of weights.

X – Set of two-dimensional point coordinates.
 Y – Set of feature vectors.
 Z – Structuring element.
 c – Constant.
 $f(D_A)$ – Transformation function of image A intensity values.
 $f(s)$ – Activation function.
 r – Circle radius.
 s – Weighted sum.
 $\nabla I(x, y)$ – Gradient at a particular point.
 λ – Eigen-value.
 σ – Standard deviation.
 $\omega(\tau_i)$ – Probability of separating two classes.

Abbreviations

BRKU – Department of Ophthalmology of the Institute for Biomedical Research of Kaunas University of Medicine.
CIE – International Commission on Illumination.
CMYK – Colour System (Cyan, Magenta, Yellow, Black).
DFT – Discrete Fourier Transform.
DNA – Deoxyribonucleic Acid.
EKS – Excavation.
FPA – Focal Plane Array.
HSL – Colour System (Hue, Saturation, Lightness).
HSV – Colour System (Hue, Saturation, Value).
HVS – Human Visual System.
 $Lab(CIELab)$ – Colour System (Luminance, a is the red-green axis, b is the blue-yellow axis).
 Lch – Colour System (Lightness, Chroma, Hue).
MRI – Magnetic Resonance Imaging.
NR – Neuroretinal Rim.
OND – Optic Nerve Disc.
PCA – Principal Component Analysis.
PSNR – Peak Signal to Noise Ratio.
RFA – Radio Frequency Ablations.
RGB – Colour System (Red, Green, Blue).
RNA – Ribonucleic Acid.

SSE – Sum of Squared Error.

YIQ – Colour System (Y – luminance, I and Q have a relation to the modulation method used to encode the carrier signal).

Contents

INTRODUCTION	1
The Investigated Problem.....	1
Importance of the Thesis	2
The Object of Research.....	2
The Goal of the Thesis	3
The Tasks of the Thesis.....	3
Research Methodology.....	4
Importance of Scientific Novelty	4
Practical Significance of Achieved Results	4
The Defended Statements.....	5
Approval of the Results.....	5
Structure of the Thesis.....	6
1. KNOWLEDGE DISCOVERY AND MEDICAL IMAGING.....	7
1.1. Data Mining.....	7
1.1.1. Components of the Data Mining Process.....	10
1.1.2. Data Mining Tasks	10
1.1.3. Data Mining Tools	12
1.2. Pattern Recognition	14
1.3. Knowledge Discovery	16
1.4. Medical Imaging.....	18
1.4.1. Electron Microscopy	19

1.4.2. Projection Radiography.....	20
1.4.3. Magnetic Resonance Imaging	22
1.4.4. Ultrasound.....	23
1.4.5. Photo Acoustic Imaging.....	25
1.4.6. Thermovisual Imaging	26
1.4.7. Ophthalmology Imaging	27
1.5. Conclusions for the First Section	29
2. INVESTIGATION OF BLOOD VESSELS IN EYE FUNDUS IMAGES	31
2.1. Survey of Methods for Vasculature Processing in Eye Fundus Images	31
2.2. Elimination of Vasculature from Colour Eye Fundus Images	33
2.2.1. Mathematical Morphology on Binary Images	34
2.2.2. Mathematical Morphology on Intensity Images	36
2.2.3. Mathematical Morphology on Colour Images	38
2.2.4. Recombination of the Results	39
2.3. Extraction of Vasculature from Eye Fundus Images	40
2.3.1. Image Pre-processing.....	41
2.3.2. Equalization of Histogram	41
2.3.3. Otsu Threshold.....	43
2.4. Conclusions for the Second Section	45
3. INVESTIGATION OF OPTIC NERVE DISC IN EYE FUNDUS IMAGES	47
3.1. Survey of Methods for Optic Nerve Disc Localization in Eye Fundus Images...	47
3.2. Localization of the Optic Nerve Disc	50
3.2.1. Edge Detection.....	50
3.2.2. Edge Gradient Detection.....	51
3.2.3. Image Binarization.....	52
3.2.4. Hysteresis Threshold.....	52
3.2.5. Hough Transform.....	53
3.3. Optic Nerve Disc Approximation by the Ellipse	55
3.3.1. Least Squares Method	56
3.4. Evaluation of Localization and Approximation Results	57
3.5. Conclusions for the Third Section	60
4. POSITIONING OF OVERLAPPING EYE FUNDUS IMAGES.....	61
4.1. Survey of Methods for Eye Fundus Registration	61
4.2. Medial Axis Transformation	63
4.3. Transformation to the Frequency Domain.....	63
4.4. Evaluation of Positioning Results	66
4.5. Conclusions for the Fourth Section	67
5. DATA ANALYSIS: SOFTWARE TOOLS AND APPLICATIONS.....	69
5.1. Software Implementation	69
5.2. Analysis of the Optic Nerve Disc Parameters	74
5.2.1. Artificial Neural Network as a Disease Classifier.....	78

5.3. Analysis of Thermovisual Data	84
5.3.1. Analysis of the Anisotropy Zone	88
5.3.2. Analysis of Heart Tissue Damage Dynamics.....	89
5.4. Conclusions for the Fifth Section	93
CONCLUSIONS.....	95
REFERENCES	97
THE LIST OF SCIENTIFIC AUTHOR'S PUBLICATIONS ON THE SUBJECT OF THE DISSERTATION	107
ANNEXES.....	109
Annex A. Analysis Results of the OND Parameters	109
Annex B. Parameters of Thermal Camera.....	116
Annex C. Lesion Area Dynamics With Respect to Time	117

Introduction

The Investigated Problem

The most important challenge for an information society is to serve for a human, and in particular, most important, to serve for his/her essential needs. Health is an invaluable not only human, but also national public asset. Recently, health care services have become quite successful in the development of information technologies, as well as in the accumulation of experience while developing methods for medical diagnosis. Every day a huge amount of heterogeneous data is generated where the heterogeneity is associated with the complexity of a human body. In the past decades, the technological improvements enabled us to collect the data in digital form, regardless of the manner the data are represented: no matter whether it is a blood pressure, electro-cardiogram, magnetic resonance or eye fundus images. The aggregation of such heterogeneous data further can be used to predict the state of the investigative domain according to some problem. However, despite the fact that the most productive source of heterogeneous data is modern medicine, perception of the gathered data is not straightforward and it is a matter of research. Perception of data itself is a fairly complex task, especially when the data indicate a complex object, a phenomenon that can be described by a set of parameters or in a visual form.

Significance of the Thesis

Nowadays the amount of information the physician has to deal with is huge. Thus, a careful analysis of such a data set is hardly possible.

Eye fundus examination is one of the most important diagnostic procedures in ophthalmology. A high quality colour photograph of the eye fundus helps in the accommodation and follow-up of the development of the eye disease. Evaluation of the eye fundus images is complicated because of the variety of anatomical structure and possible fundus changes in eye diseases. Sometimes it requires high-skilled experts for evaluation. However, as the investigation in this dissertation shows, even high-skilled expert's assumptions on the same object, shown in the images, differ. The problem arises while making a medical decision when the state of a patient has to be assigned to the initially known class. For clarity, the class can be defined as ailing or healthy. However, the boundary between the alternatives of diagnosis is not straightforward in most cases and the decision for the disease presence can be made very subjectively. In the medical context it is a topical problem. If an ailing patient is classified as healthy, the results could be unpredictable. In this dissertation the methods for an automated eye fundus images processing is presented with the aim to ease the evaluation of important features.

In cardiac surgery, corrections of many cardiac disorders are treated by applying some destructive energy sources. One of the most common sources and the related methodology is to use radio-frequency ablations. In medical practice treatment capabilities have expanded almost to the whole area of the cardiac texture zones. However, despite the latest technical, navigational methods for localizing the affected zone, the rate of the risk of complications including a disease recurrence remains very high. The drawback of the methodology used is that the suchlike surgery procedure cannot be monitored by a visual spectra. This fact concludes in the inability to control the treating procedure. With the aim to understand the nature of possible complications and to control the treating process the means of thermovision is used. The dissertation discloses the lesion area dependency on time and electric current power parameters at different heart tissues.

The Object of Research

The research object of this work is analysis of visual medical digital data, as well as the ways of improving data understanding of the subject matter:

- Eye fundus images:

- Eye fundus vasculature.
- Optic nerve disc.
- Eye fundus registration.
- Thermovisual data:
 - Pulmonary vein and atrium tissue lesion area dynamics under the sway of radio-frequency ablations.

The Goal of the Thesis

The target of the thesis is to develop state-of-the-art algorithms for automated medical image processing that could be used in ophthalmologists' or cardiac surgery practice. Thesis focus on the automated means for the visual information processing that could lead to a decision support.

The main goal can be decomposed as follows:

1. To eliminate/extract the tree of vasculature form colour eye fundus images in an automated way.
2. To locate and parameterize the optic nerve disc in colour eye fundus images in an automated way.
3. To register eye fundus images in an automated way.
4. To identify the heart tissue thermal anisotropy by thermovisual data.

The Tasks of the Thesis

The tasks of the thesis are methods of image processing for structure segmentation and parameterization. Thus, the related subjects to the tasks are:

1. Pixel-wise operations.
2. Mathematical morphological image processing.
3. Image thresholding.
4. Image segmentation.
5. Object topology extraction.
6. Edge detection.
7. Cone fitting.

8. Non-linear colour system conversions.

Research Methodology

The methods for image processing are applied in this thesis, especially, the methods of mathematical morphology, edge detection, and topology extraction. Besides, the methods of statistical analysis, clustering and classification are also applied in data evaluation.

Importance of Scientific Novelty

Many blood vessel detection methods are available, but the results are not always satisfactory due to time-consuming computation or the segmentation quality. This dissertation presents an automated, robust kernel-based methods for blood vessel elimination/extraction in colour retinal images. Methods rely on mathematical morphology operations and pixel-wise analysis. They does not incorporate any Laplace or Gaussian image threshold or cross-section calculations. Also, there is no need to invoke artificial neural networks computation methods for matched filter computing. Next, the task is expanded to the image registration problem. An efficient algorithm of two image registration is presented. Finally, an automated algorithm is introduced for optic nerve disc localization and parameterization by an ellipse that can be used by the physicians as a reference one for optic nerve disc size estimation.

At the end of the dissertation, the algorithm for automated heart tissue thermal anisotropy zone identification is presented. The analysis of the data obtained let us evaluate the dependency of anisotropy area according to electrodes impulse current power and lesion time.

Practical Significance of Achieved Results

The results of this research revealed new viewpoints in the evaluation of the optic nerve disc boundary parameterization. Also, the uniqueness of the structures of the eye fundus was explored. Furthermore, analysis of the thermovisual data disclosed the heart tissue lesion dynamics according to time and impulse current power parameters. Research were partly supported by the Lithuanian State Science and Studies Foundation projects:

- "Information technologies for human health – support for clinical decisions (eHealth), IT health (No. C-03013)" Start date: 09-2003; finish date: 10-2006.
- "Information technology tools of clinical decision support and citizens wellness for e.Health system (No. B-07019)" Start date: 09-2007; finish date: 12-2009.
- "Development of special data mining methods to explore the anisotropy of texture's temperatures of the heart (No. T-08153)" Start date: 04-2008; finish date: 12-2008.

The Defended Statements

1. Disc-shaped structuring element can be used for blood-vessel removal and extraction in colour eye fundus images.
2. Recombination of the eye fundus image channels into a colour representation does not introduce colour distortion after the mathematical morphological processing. This results in an algorithm that leads to a high accuracy of automated optic nerve disc localization in eye fundus images.
3. It suffices a linear transformation of an image to solve the eye fundus registration problem when used the topology of eye fundus vasculature.
4. The heart tissue thermal anisotropy dynamics remains almost the same during heating and cooling stages at different impulse current power settings.

Approval of the Results

The main results of the investigation are published in 10 scientific publications; 3 publications are included in the Institute of Scientific Information Citation Index Expanded (*ISI Web of Science*) list; 1 publication is printed in the journal that is included in the list of the Institute of Scientific Information Conference (*ISI Proceedings*); 1 publication printed in journal approved by Lithuanian Science Council; 5 publications are printed in the national and international conference proceedings. The research results were presented and discussed in the following national and international conferences, workshops and seminars in Lithuania and abroad:

- Scientific conference "*Information Technologies*", 2005. Kaunas, Lithuania.
- Scientific conference "*Computer Days*", 2005. Klaipėda, Lithuania.
- International conference "*Biomedical Engineering*" 2005, 2008. Kaunas, Lithuania.
- Lithuanian Eye Physician Congress, 2005. Palanga, Lithuania.
- Workshop of Academy of Sciences of the Czech Republic. Institute of Computer Science, Department of Computational Methods, 2005. Praha, Czech Republic.
- 6th Nordic conference on eHealth and telemedicine "*From Tools to Services*", 2006. Helsinki, Finland.
- Lithuanian conference of young scientists "*Operation Research and Application (LOTD)*", 2007. Vilnius, Lithuania.
- Workshop of informatics summer school "*Modern Data Mining Technologies*", 2007. Druskininkai, Lithuania.
- International conference "*Advancing Science through Computation*", 2008. Krakow, Poland.
- Seminar at AvayaLabs "*Feature Extraction from Medical Images*", 2008. Basking Ridge, New Jersey, United States of America.
- International workshop "*GraVisMa: Computer Graphics, Vision and Mathematics*", 2009. Plzen, Czech Republic.

Structure of the Thesis

The thesis consists of the Introduction, five sections, and the summary of the results. There are three annexes, as well.

The volume of work is 108 pages, excluding annexes; are used 36 numbered formulas, 57 figures, and 8 tables in the text. The thesis lists 140 references.

1

Knowledge Discovery and Medical Imaging

Perception of data is a difficult task, especially when the data indicate a complex object whether it is presented in a parametric form or in spatial domain as an image. The analysis of the data with a view to obtain an information is comprehensive task and can be defined by the phases of knowledge discovery process. In the first part of this section the short overview of the principal phases of knowledge discovery process is presented. In the second part, the ways that forms the medical images are discussed as well.

1.1. Data Mining

The aim of data mining is to make sense of large amounts of mostly unsupervised data, in some domain (Cios *et al.* 2007). The statement that describes data mining is easy to understand. As usual, users of data mining are the experts of the problem domain. These experts not only collect data, but also have an understanding of data meaning as well as the process, which generated it. However, a better understanding of data to an expert is not the primary task.

The experts desire to gain additional knowledge about the problem domain, which may lead to a novel, possibly better way of problem solving.

In practice the term make sense has a different meaning, since it is closely related to the user's experience in the domain. It is obvious that the sense should incorporate knowledge as well. This implies that, in order to describe the sense, we have to address a series of the attributes such as understandable, valid, novel, and useful (Fayyad *et al.* 1996). The attribute of the greatest importance for data owners in order to get knowledge is understandable, since they aim at gaining some advantage. This results in a model of the data which can be outlined in easy to understand terms, let us say, by introducing the production rules:

IF abnormality (obstruction) IN optic nerve disc
THEN eye disease.

For this kind of example the input data may be images of the eye fundus. If the initial data have already been examined by an ophthalmologist, then such data (images of the eye fundus) are called learning or training data. There are data mining techniques as described by (Apte and Weiss 1997), which do generate the production rules and the ophthalmologist can accept or reject them after the analysis. However, not all the rules generated by data mining may be known to the physician. These rules which were unknown for the data owners, but perform well on the not yet used data are known as test data.

Assume that the provided example and the rules generated by the data mining methodology are already known for data users. Of course, this validates the data mining methodology, but, in terms of knowledge novelty, it would be useless and the project results would end in failure, since the data owners have already gained the knowledge in the past. By taking into account the new unseen or unfamiliar rules we arrive at the third attribute which describes the term making sense. This attribute is of utmost importance – namely the discovered knowledge has to be novel. Further, assume that the knowledge how to diagnose the patient has been gathered not by the rule production technique, but from the neural networks. The neural network itself would not be acceptable for the physician, since, in a broad sense, it is a black box that in general is hard to understand. However, if the neural network is trained and proved to act well in many cases and is used to automate the analysis (pre-screening) of the eye fundus images before the patient comes to the ophthalmologist, then it would be acceptable. After the simple analysis provided above, we find the fourth attribute. In this manner, one can associate the term making sense with the requirement that the disclosed knowledge has to be useful. However the meaning of usefulness has to be preserved regardless of the type of data mining model used.

Especially one should note that the data mining techniques deal with a large amount of data. The scope of data mining does not cover the small data sets that can be easily managed manually.

As usual, one of the last definitions describes the type of data used in data mining. It is obvious that to collect unsupervised data is much easier and less expensive, because when dealing with supervised data one has to know the inputs with the appropriate output determined by the problem domain specialist.

Naturally, the process of unsupervised data collection rises a problem, what should we do with the data collected? This issue is most difficult in terms of data mining. It demands to use such algorithms that are able to find existing groupings or clusters of the data, moreover, it has to find the relationship or associations in the data provided by the data owners. If we are lucky and clusters are found in the data and they are labelled by the experts, then it transforms the initial problem to a resulting problem which is evaluated in a much easier way, since our data become supervised. Basically it does not matter which data mining technology we are using. If one uses the clustering technique, then this approach lacks of the a priori knowledge on clusters that are present in the data. Similarly, by using association-rule mining algorithms, it is required to specify some parameters that allow the generation of an appropriate number of high-quality associations. In both cases it is necessary to apply aggregate algorithms.

In medical practice it is very common to have only a few images of the eye fundus that have been diagnosed. The situation above, where the available data are semi-supervised, means that there are only a few known training data points with respect to a plenty unsupervised data points. Intuitively one can doubt if these few data points can be somehow used to make sense of the entire data set. In principle, there exist methods for semi-supervised learning (Vatsavai *et al.* 2005), which take the advantages of these few training data points. However, the majority of data mining techniques works well using the supervised data, but not all of them are scalable. Scalability is the property of the data mining technique which works well on both a small or large data set. Yet there are only a few of them.

The final term in the definition of data mining is domain. The success of the project depends on the obtained level of the domain knowledge. At this stage it is very important that data miners and domain data owners work together in order to gain the required understanding of the problem domain. This process is highly interactive and iterative, because at every iteration one has to evaluate the knowledge obtained and to incorporate this information into the next iteration. Hence, it is impossible to take a successful data mining system designed for some domain and apply it to another in the hope of good results.

Data mining is not just about making sense of the data. It is important to realize that the data mining methods are data driven, not the model driven. For example, in statistics one tries to find the smallest data size that gives satisfactory estimates over the whole data set. However, in data mining one tries to find a not too complex model that would well describe a huge data set. This task is extremely difficult, thus we always need to look for the balance between model completeness and model complexity.

1.1.1. Components of the Data Mining Process

Data mining seeks to find models which fit or determine the patterns from the data observed. Typically, in this problem the human interaction is required in order to make a decision whether the model reflects the knowledge or not. According to (Mitra *et al.* 2002) data mining algorithms are basically tripartite:

1. The model: The function of the model such as classification or clustering together with its representational form which can be linear, say, discriminant or neural networks. All these models have parameters that must be determined from the data.
2. The preference criterion: One has to know the preference criterion of one set of parameters over another. Of course, this has to be done by taking into account the initial data. The criterion describes how well the model fits to the provided data. However, the criteria have to be selected such that preserved model over fitting or avoidance of too many model parameters.
3. The search algorithm: The search algorithm has to find the model parameters, and the preference criterion for the given data. Typically, the algorithm of data mining is the instance of the model, preference, and the search components.

1.1.2. Data Mining Tasks

Data mining and analysis involve a mass of algorithms. The analysis of the literature exposed that those algorithms depend on the nature of the problem domain. In this context, algorithms attempt to find models that have suchlike characteristics as the data provided. In the aggregate the current tasks or functions of data mining include:

1. The analysis of association rules. Analysis of the association rules tends to describe the relationship among the attributes of the problem domain. Typically, these attributes belong to different classes. A well known

example of the association rule discovery is the market basket case. Suppose that the market basket is an aggregate of the items, the buyers of items, and it is an individual transaction for the specific customer. The analysis over the transaction database can show items or sets of items that frequently emerge. Thus, each extracted object consists of the items and, moreover, one can count how much items has been sold. This knowledge can be incorporated into business to improve the placement of items in a store (Dunham 2002). Though by increasing the number of the attributes such a problem formulation makes the task a challenging one. The analysis of the association rule discovery process has to imply that associations do not show the functional dependency of the attributes.

2. Clustering. The term clustering is used to describe the methods which map data objects to clusters or groups according to the provided similarity metrics or probability density models (Fayyad *et al.* 1996). As an instance of the data object could be the description of the state of a patient either in textual or in spatial (image) form. Then the clustering algorithm will try to find natural groupings of similar patients together by maximizing the differences between different groups of patients. It should be noted that the outlier analysis is a special clustering case. Usually outliers do not belong to predefined or extracted natural groupings and originate as a noise in the data or as supplementary data for uncommon situations seen in the problem domain.
3. Classification. The aim of the classification is to identify descriptive parameters of the class to which an object belongs. This task differs from clustering. A distinction is that, in the classification case, one has to know categorical classes or the classes have to be defined a priori (Mitra *et al.* 2001). This technique can be used to solve some prognosis tasks.
4. Sequence analysis. The sequence analysis models objects that are connected to others in some predefined way. This analysis does not take into account the type of object connectivity, it explores a group of the objects attributes or trends in a time, spatial or textual domain. The investigative data for such an analysis can be time-series in order to evidence the trends. Moreover, the sequence analysis aims to find the repetitive small sequences, let say, in the sequence of RNA or DNA, which could probably indicate unwanted changes or a disease. This particular task is very important in the background of bioinformatics (Kuisienè *et al.* 2008).

5. Regression. The principle of regression is well known: in order to predict new data values, already the known ones are used. Basically regression uses standard statistical methods, such as linear, non-linear regression. However, in most cases the data in a linear manner cannot be expressed by the previous data, thus the sophisticated method has to be used (Noda *et al.* 1999).
6. Summarization. The task of summarization describes the data we are dealing with. Before we start to shape a model, we have to realize the data we are going to investigate. This realization can be expressed in terms of statistics: mean, variance, deviation or even histogram mode, quantiles, etc. One has to make a hypothesis which of them we will have to support or reject during the process of data mining (Bernatavičienė 2008).
7. Dependency modelling. Dependency modelling analyses important dependencies among variables or the attributes of data.

In a view of the image processing, most important task is classification. Basically, the classification task of is solved by converting the colour or intensity image to the black and white where the boundaries of the classes are explicitly defined. Then the sequence analysis can be introduced to attribute the feature pixel to some object. However, the problem is that the result of the classification depends on the clustering algorithm used. Clustering algorithm, in turn, does depend on the summarization task. If the data is misunderstood the model will not reflect the existence of the classes and the clustering algorithm will not be able to distinguish the boundary between them.

1.1.3. Data Mining Tools

There is a wide number of data mining algorithms described in literature. They cover such fields as statistics, pattern recognition, machine learning, or even databases. On the face of it, these algorithms represent a lengthy list of unrelated methods. However some representative groups can be identified (Hand *et al.* 2001):

1. Statistical models. The models of statistical analysis, for example linear discriminants (Ye 2007; Hastie *et al.* 2009) make number analysis on the provided dataset. This analysis enables us to conclude on the impact relationships of a variety of attributes. The results achieved can be applied to describe the functionality of the exploratory phenomenon or to estimate the trends of further evolution.

2. Probabilistic graphical dependency models, for example, Bayesian networks or hidden Markow models. Such models are graphical when a probability can be broken down into a combination of several elementary contributions and it can then be represented as a graph (Moreau *et al.* 2003).
3. Decision trees and rules. In the case of models and rules of decision trees, first of all a tree, which models the process of classification, is created. In the tree structure, leaves represent classifications and branches represent conjunctions of features that lead to those classifications. Thus, these algorithms segment the input space and each segment describes the investigative classes (Dunham 2002; Fielding 2006).
4. Inductive logic programming based models. In order to describe the inductive logic we have to separate the kind of arguments. There are deductive and inductive arguments. The premises of deductive arguments are aimed to guarantee the truth of their conclusions, while inductive arguments involve some risk of their conclusions being false, even if all of their premises are true (Hurley 2005). Thus, the inductive logic programming based models are based on the latter ones.
5. Example-based methods. The common example of the example-based methods is a method of nearest neighbours. The classification task of element grouping is solved not according to the rules identified during the analysis, but the task is subject to likeness of element properties to the properties of neighbours. This implies that the base of these methods is a comparison of the investigative object to the set of already known ones (Bernatavičienė *et al.* 2006).
6. Neural network-based models. The primary objective of the neural network theory is not to model biological neurons in detail, but to describe and apply the principal mechanisms of biological neurons with a view to achieve more effective systems of information processing. Currently these models score a great success, since they are capable to model sophisticated either classification-based or proposing functions (Medvedev 2007; Bernatavičienė *et al.* 2005).
7. Fuzzy set, fuzzy system models. Fuzzy systems offer a very powerful framework for approximate reasoning since they attempt to model the human reasoning process at a cognitive level. Such systems acquire knowledge from domain experts and this is encoded within the algorithm in terms of the set of If-Then rules. Fuzzy systems employ

this rule-based approach and interpolative reasoning to respond to the new inputs (Khan and Abraham 2003).

8. Rough set theory-based models. Now it is obvious that the data can be acquired from some measurements or from the experts of the problem domain. The main goal of the rough set analysis is to synthesize the approximation of concepts from the acquired data. Later on, this synthesis evolves towards information granules under the tolerance relation (Komorowski *et al.* 1999).
9. Genetic algorithm-based models. There are a lot of problems for which computational algorithms show themselves poor. Basically, problems arise in the class of algorithms which are in some global optimization search within a large space. It is often possible to find an effective and computationally practical algorithm the solution of which is relatively optimal. One approach which deals with such problems is to use genetic algorithms which are based on the principles of natural evolution (Berry and Browne 2006).
10. Hybrid and soft computing models (Kecman 2001). These models describe an innovative approach to construct computationally efficient and intelligent hybrid systems, consisting of an artificial neural network, fuzzy logic, approximate reasoning and derivativeless optimization methods, such as genetic algorithms (Khan and Abraham 2003).

All the data mining algorithms describe the flexibility of the algorithm and interpretability of a model to the problem domain specialist. The more complex model, the better it describes or fits the provided data (Han and Kamber 2005). However the complexity has its own drawbacks. It decreases the understandability of the model, moreover, it does not guarantee the reliability. None of the groups of models are universal or perfect. By selecting a model, one has to consider the operational or logical complexity, the cost of computational time and the resource consumption, and, especially, the reliability of the analysis. Moreover, reliability of the analysis in medical practice has to be comprehensively evaluated.

1.2. Pattern Recognition

Pattern is compact and rich in semantics representation of raw data (Taniar 2007). The process of pattern recognition mainly deals with a problem of designing algorithms or methodologies which can be applied in the computer

systems in order to accomplish the recognition tasks that human have to in everyday life. The motivation is self-explanatory, computers can perform a task more accurately, faster and in most cases more economically than the problem domain specialists. Thus, the aim of the pattern recognition is to find the ways and means to automate some decision making process, which further will lead to classification and recognition (Witten and Frank 2005).

As stated in earlier in this section, the aim of data mining is to make sense of large amounts of mostly unsupervised data, in some domain (Cios *et al.* 2007). Moreover, data mining analyses huge data sets from the problem domain but excludes the knowledge interpretation part. Usually these massive data sets are characterized not only by numeric values, but also can be textual, symbolic, pictorial or sonic and even more they can be mixed. In addition, they may have redundancy problems, imprecise data, missing data, and so on. This implies that in order to gain some new knowledge, one has to deal with heterogeneous data. Namely the pattern recognition plays an important role in the knowledge discovery process. Therefore, from this perspective, data mining can be viewed as application of pattern recognition and machine learning principles in the context of voluminous, possibly heterogeneous data sets (Pal 2001).

Basically, the machine recognition of pattern is comprised of two tasks. One task consists of learning the common properties of a set of samples which describes the class in the problem domain. The other task is to decide if a new sample is a possible instance of the class. The decision should be made according to the similarity criterion between the instance attributes and the class attributes. Generally, the task can be described as a transformation from the measurement space to the feature space, and finally to the decision space (Cios *et al.* 1998). Mostly a typical pattern recognition system joins three phases (Pal and Mitra 2004):

- Data acquisition phase: Generally, the data structures, from the problem domain data sets, that are used in pattern recognition systems, are of two types object data vectors and relational data:
 - Object data or a set of numerical vectors are represented in the sequence as $Y^p = \{y_1, y_2, \dots, y_n\}$, a set of n feature vectors in the p -dimensional measurement space.
 - Relational data are a set of numerical relationships between pairs of objects.
- Feature selection/extraction: is a process of selecting a map of the form $X^p = f(Y^p)$, by which a sample $Y^p \in \{y_1, y_2, \dots, y_p\}$ in the p -dimensional measurement space is transformed into the point

$X^{p'} \in \{x_1, x_2, \dots, x_{p'}\}$ in the p' -dimensional feature space, where $p' < p$.

Feature selection or extraction is usually apprehensible as a process of finding such a subset of features from the features of the original set that forms patterns in a given data set, according to the optimal defined goal and criterion of feature selection (Suraj and Delimata 2006). This leads to two aspects: formulation of a suitable criterion to evaluate the goodness of a feature set and search of the optimal set in terms of the criterion. The good criterion for the feature selection is such that does not change under any possible variation of attributes within a predefined class while emphasising some differences which are important to distinguish two different patterns. The major mathematical measures are mostly statistical and can be broadly classified into two categories: feature selection in the measurement space and feature selection in a transformed space (Pal and Mitra 2004). The first category reduces the dimensionality of the measurement space by discarding redundancy or least information carrying features. Those in the second category use information contained in the measurement space to obtain a new transformed space. Hence it maps a higher pattern to a lower one, in terms of dimensionality.

- Classification/Clustering phase. This phase incorporates the methods described in Sections 1.1.2 and 1.1.3.

Typically, data sets are selected using a set of sensors. Then the data are passed to the phase of feature selection or extraction. At this phase, the dimensionality of the initial data from the problem domain is reduced. As described above, the process of reduction should preserve only the key features or properties from the initial data set according to some criteria. Namely, the phase of feature selection-extraction is crucial in entire recognition process. Finally, in the classification-clustering phase, the selected-extracted features are passed on to the classifying-clustering system that evaluates the incoming information and makes a final decision. This phase basically establishes a transformation between the features and the classes-clusters (Pal and Mitra 2004).

1.3. Knowledge Discovery

Knowledge discovery is a nontrivial process of identifying valid, novel, potentially useful, and ultimately understandable patterns in data, provided by the problem domain specialists (Pal and Mitra 2004).

As described by (Shapiro and Frawley 1991), assume that one deals with the given facts or raw data, some certainty, and the language. Then the pattern can be described as a statement in language that determines the relationship between two sets: subset of facts according to statement, and the initial set of raw facts. Furthermore, determined relationship has to meet the desired certainty. Then, identification of pattern is valid only if pattern is simpler than the enumeration of all the facts in subset of initial facts. Moreover, the pattern has to be interesting, according to the provided interest measure, and certain enough. The term interestingness of a pattern involves validity, novelty, usefulness, and understandability. In other words, the interestingness selects a number of discovered patterns that incorporate novelty and understandability or can be used by the problem domain specialist in everyday practice. Whether the pattern is novel depends on the frame of reference. It can be the scope of the system's knowledge or that of the user.

Basically the interestingness of the pattern can be determined by an objective or subjective approach. In the objective approach, the rule interestingness is estimated of the pattern structure. However, this approach suffers from the pattern discovery process, since it fails to capture the process complexity. On the other hand, in the subjective approach, the measure of interestingness is subject to the user that examines the pattern.

Thus, data mining is only a step in the knowledge discovery process. This step incorporates data analysis and discovery algorithms that are able to enumerate the patterns in the given data set. The enumeration is accomplished by taking into account acceptable computational limitations. The principal scheme of the knowledge discovery process is presented in Fig. 1.1.

Usually it involves the following steps (Pal and Mitra 2004):

1. Data cleaning and pre-processing. This step includes operations such as noise or outlier removal, pre-processing of missing data. This step is introduced to proceed the real world data that are often inconsistent, incomplete or erroneous. The low quality data should be cleaned before data mining process takes place.
2. Data condensation and projection. The process is intended to find the features or samples that can be useful or used for a better data representation. This step includes the methods for dimensionality reduction or transformation if it is required by the object of the task.
3. Data integration and wrapping. In the real world, mostly all the data are heterogeneous. Heterogeneity is introduced by using different means for data acquisition devices. Thus, the aim of this step is to provide description of the heterogeneous data that could ease the future use.

4. Choosing the data mining function(s) and algorithm(s). Basically, this step is aimed at determining the purpose of the model that is required by the data mining algorithm. The purpose can be classification, clustering, association rules, etc. Also, selection of methods or models used in search of a pattern in data has to be considered as well. A brief description of such methods is presented in Section 1.1.3.
5. Data mining. The step of data mining consists in search of patterns of interest. This search is aimed at achieving a particular representational form or even a set of such representations.
6. Interpretation and visualization: This step is self explanatory; it includes the interpretation and/or visualization of discovered patterns. The purpose of the activity is to identify really interesting/useful patterns for the user.
7. Using discovered knowledge. Incorporation of the knowledge achieved in everyday practice that improves the problem domain understanding.

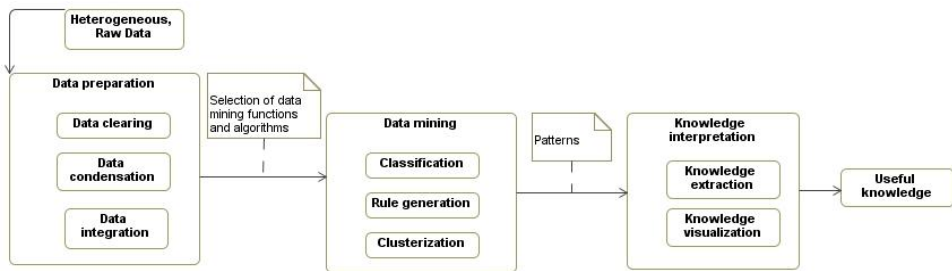


Fig. 1.1. Scheme of knowledge discovery process (Pal and Mitra 2004)

Thus, the aim of the knowledge discovery process is to map the initial data, provided by the experts, to a higher level where some useful and interesting knowledge can be achieved from the data.

1.4. Medical Imaging

Technology now allows us to capture and store vast quantities of data. Finding patterns, trends, and anomalies in these datasets, and summarizing them with simple quantitative models, is one of the grand challenges of the information age – turning data into information and turning information into knowledge (Witten and Frank 2005). Images are the principal sensory pathway to knowledge about the natural world (Hendee and Ritenour 2003) Thus, one has to

look for the new data mining techniques or modify existing ones in order to enumerate existing patterns in the provided data. Finally, this can lead to new knowledge discovery. Further in this sub-section a short review of basic imaging techniques used in medicine will be carried out.

1.4.1. Electron Microscopy

Electron microscopy studies objects that cannot be studied in the optical way. This effect has a pure physical explanation, i. e., the wavelength of a photon is much larger than the wavelength of an electron. Basically, there are two types of microscopes: transmission electron microscope, and scanning electron microscope (Bozzola and Lonnie 1998).

Usually, an optic telescope is an aggregate of a light source, condenser, that focuses the light to the investigative object, object holder, lens, and ocular. The same principle results in an electron microscopy. However, the light source is replaced by an electron gun, the object holder is replaced by a metal grid, and instead of lenses electrostatic and electromagnetic lenses are used (Dykstra and Reuss 2003).

Transmission electron microscope. The electron beam is accelerated by high voltage at the cathode. This generates a great difference of potentials with respect to the anode. This beam is passed to the anode through the electrostatic and electromagnetic lenses. The purpose of these lenses is to turn the beam through the investigative object to the anode. The major part of electrons goes through the investigative object. The specimen is in part transparent to electrons and in part scatters them out off the beam. Thus, after emerging from the investigative object the beam carries the information about the structure of the specimen. Then the resulting beam is magnified by the lenses and after all, kind of, a spatial image is projected on the fluorescent screen. It is worth noting that electron microscopes operate only in vacuum, since the electrons have a very low permittivity. This property of electrons requires a specimen to be ultra thin (about 50nm). Spatial image produced by transmission electron microscope is presented in Fig. 1.2 on the left-hand side.

Scanning electron microscope. Contrary to the transmission electron microscope, the electron beam emerged does not carry the complete spatial image information on the investigative object. The microscope probes the specimen surface over the rectangular area by applying a raster scan pattern. Raster scan is a method when the rectangular area is covered by parallel lines. Yet the microscope scans the specimen line by line with the beam of electrons. Similarly as the transmission electron microscope, the investigative object is in part transparent and in part not to the electrons. When the beam hits the sample it loses its energy. This loss evidences in heat, emergence of secondary

electrons, light emission, and X-rays. Thus, by mapping the scattered energy as intensity onto the display in a position corresponding to the position of the beam when the signal was generated, we obtain the spatial image (Fig. 1.2 right-hand side) of the investigative object.

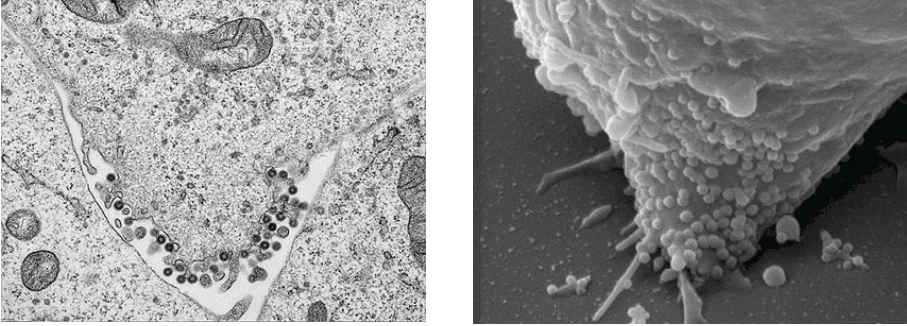


Fig. 1.2. The transmission (*right-hand side*) and scanning electron microscope (*left-hand side*) images, source: (Analytical Imaging Facility 2005)

Generally, the scanning electron microscope produces images of lower magnitude than those acquired by the transmission electron microscope. However, the former microscope enables us to explore investigative objects in more detail and also the specimen can reach the size of 15 centimetres. However both types of microscopes cannot examine living objects since they operate in a vacuum.

1.4.2. Projection Radiography

The process of object exposure by high-energy form of electromagnetic radiation and capturing the remnant beam as a latent image is called a projection radiography (Farr and Allisy-Roberts 1996). In this case, X-rays are used as electromagnetic radiation. The X-rays have a unique property which enables them to be used as a non-invasive, surgery-free method for patient screening. The wavelength of X-rays is from 0.01 to 10 nanometres, while the wavelength of visible light is from 380 to 750 nanometres. One can notice the similarity of the X-rays to the gamma rays in terms of wavelength, since they overlap each other. The distinction of the two types of electromagnetic radiation is that X-rays are electrons emitted outside the nucleus, and gamma rays are emitted by the nucleus (Gruppen *et al.* 2005).

Usually, if we are talking about the visible electromagnetic spectrum, such a light can be characterized by the properties of refraction or even by using the

lens it can be focused. However, X-rays also refract but the refraction is hardly notable, thus the technique of beam focusing is not used in practice. As described in Section 1.4.1 considering the electron permittivity, to produce the X-rays, the vacuum lamp is needed. In the usual type of the X-ray tube, an incandescent filament supplies the electrons and thus forms the cathode, or negative electrode, of the tube. X-rays are produced when electrons, travelling at a high speed, collide with matter or change direction. A high voltage applied to the tube drives the electrons to the anode, or the target. The sudden stop of these rapidly moving electrons on the surface of the target results in the generation of X-radiation (Quinn 1980). Generated radiation then passes through the less dense material such as fat, muscles, air, or other tissues, while the more dense tissues as bones, lungs, effected by pneumonia, scatter the radiation. Radiation arising from the investigative patient then strikes the fluorescent phosphorus screen and exposes the film. The darker the region on the film, the more X-radiation that region has absorbed (Fig. 1.3. left-hand side). The X-rays are used not only to expose the dense tissues of the human body. They allow us to monitor some structures in motion in real time. In this case, the radio-contrast agent has to be absorbed by the patient. The purpose of the radio-contrast is to make the investigative tissues denser. This allow us, for example, to monitor the blood flow in arteries and veins (Parsons *et al.* 2005). Such a technique is called fluoroscopy and the fluoroscopy of the arteries and veins are called angiography. A characteristic image is shown in Fig. 1.3, on the right-hand side.

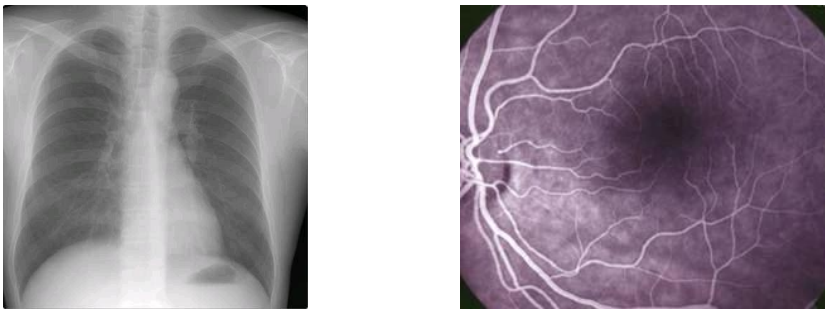


Fig. 1.3. Chest X-ray (*left-hand side*), source: (RadiologyInfo 2010).
Angiogram of the eye fundus (*right-hand side*),
source: (New York Eye and Ear Infirmary 2010)

Another appliance of the X-rays is the technique called tomography or computed tomography. During this type of patient screening the X-ray tube is not fixed but rotates in a circle while the patient is lying still. On the opposite side of the X-ray tube the detector rotates as well. Thus, by rotating the X-ray generator along with the detector in 360° degrees a slice of a body can be

obtained in digital form. During the investigation a detector registers the attenuation of X-rays when they pass through an object. Basically, object is modelled as a two-dimensional X-ray attenuation constant and the total attenuation suffered by a beam of X-rays. Finally, digitalization of the image is computed using the Radon transformation (Carlton *et al.* 2005). Nowadays the computed tomography can produce a three-dimensional representation of an investigative object as well.

1.4.3. Magnetic Resonance Imaging

Magnetic resonance imaging (MRI) is quite a new technology. It aims to visualize the internal structure and function of a body (Žitkevičius 2007). This technology is mainly based on three complementary parts: magnet, resonance, and, finally, data visualization part (Todd 2000).

Usually, the magnetic resonance imaging technique can be established by three types of magnets. It should be noted that, in the magnetic resonance imaging, the power of the magnet varies from the 0.5 to 2.0 Tesla (1 Tesla equals 10,000 Gauss). For comparison the Earth's electromagnetic field is equal to 0.5 Gauss.

The resistive magnet is a compound of coils or cylinders around which wires are wrapped. Then, in passing the electricity through the wires, a magnetic field is generated. This type of magnet has a relatively low cost and the magnetism disappears when the electricity is shut down. However, to maintain the magnetic field it consumes a huge amount of electricity. Permanent magnets are the same as the resistive ones, but the magnetic field is generated constantly, thus it costs nothing to maintain the electromagnetic field that is generated all the time at full strength. The main drawback of such a magnet is that, depending on the power of the magnet, the weight increases dramatically. Finally, the last type of magnets is semiconducting magnets which are most commonly used. These types of magnets are like the resistive ones, yet the wires are placed in the liquid helium at the temperature about 452 °C below zero. This causes a drop in natural wire resistance to almost zero and dramatically decreases the electricity consumption, what makes the operation of the device more economical.

Another principle on which the technology depends is the resonance property of nuclei (Mitchell and Cohen 2004). A body consists of billions of different atoms, however the most important is the hydrogen. The hydrogen atom has two important properties that make it interesting, namely, one proton and a large magnetic moment. The magnetic moment means that the atom has a strong tendency to line up with the direction of the magnetic field. Another thing to be mentioned is that the nucleus of an atom precesses about an axis and has two spin eigenstates. In the normal conditions, where there is no magnetic field

the sum of the eigenstate energies are equal to zero. Yet things change when the magnetic field is introduced. By putting some tissue in a strong magnetic field, it gets magnetized, i. e., protons align along the magnetic field axis in either parallel or anti-parallel direction. The greatest part of the protons aligns in parallel to the magnetic field direction. Thus, the tissue gets magnetized. The parallelism of the protons depends on the Lamb shift (Lamb and Retherford 1947). Those protons which are anti-parallel have lower energy and are most interesting

(Brown and Semelka 2003). After applying the radiofrequency wave, these protons reach a high level by absorbing wave energy. This feature is known as a resonance. When the radiofrequency wave is cut, the protons, that absorbed energy, slowly emit the absorbed energy in a resonant wave frequency while returning to the natural position. By registering the frequency and phase of a resonant wave and applying the inverse Fourier transform, the achieved signal information can be visualized in a spatial domain. Some pictures of magnetic resonance imaging are presented in Fig. 1.4.

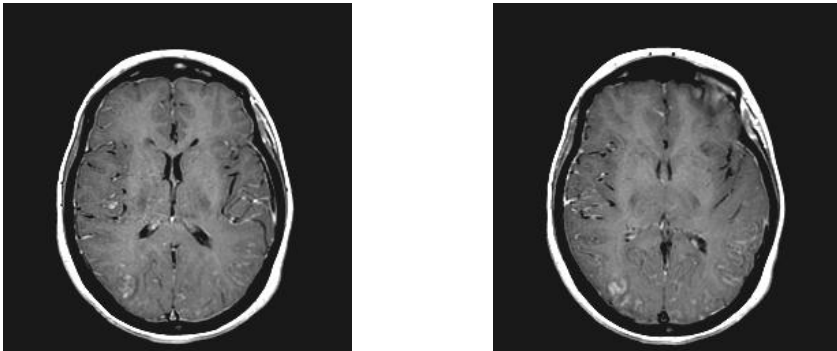


Fig. 1.4. MRI images, source: (Johnson and Becker 1999)

1.4.4. Ultrasound

Ultrasound as the name implies is the high frequency acoustic waves. It should be mentioned that acoustic waves are longitudinal. This means that waves shift the particles in the same direction as the wave is passing. Yet this type of waves cannot pass through the vacuum and need a supporting medium, unlike the waves of a visible spectrum. In the medical context, the frequency of the waves varies from the 2 to 15 megahertz, and it is obvious that sound waves travel at different speeds (Thrush and Hartshorne 1999). In this case, the speed depends on the density of the material, however within same material it remains constant. The more denser the material the slower a wave travels through it. Thus, the privity of sound speed is needed in order to get knowledge how far the wave has

travelled in the tissue. In the medical context, in most systems it is assumed that the speed of sound is constant for all tissues and equals to 1540 meters per second.

The ultrasound is generated using a piezoelectric effect. Usually, piezoelectric materials vibrate as the voltage is applied over them. Then, by varying the voltage, the frequency of the vibration varies as well. The thickness of piezo-material describes the resonant frequency, i. e., the most effective vibration. Then, again, the piezoelectric effect is introduced, which is aimed to gather the reflected vibrations from the tissue and convert into an electrical signal. It should be noted that all the ultrasound devices operate using pulsed generation of sound waves. If a continuous wave is passed to the tissue, then the reflecting waves will also be continuous along the passing path and thus it will be impossible to predict where the returning echoes reflect from. Each pulse consist of a range of frequencies of different amplitudes. When the generated ultrasound beam hits the tissue, some portion of ultrasound will be transmitted further, and some portion reflected back to the transceiver (Mačiulis *et al.* 2009). If two tissues have a similar density then most part of the signal will be transmitted, otherwise, reflected back.

Yet in terms of gathering the reflected beam, the position of the transceiver with respect to the investigative tissue is crucial in order to reconstruct the image. It is desirable that the transceiver and the investigative tissue were perpendicular to each other. If this condition is not met, the effect of refraction and angular reflection can be observed. This would result in a loss of the tissue-reflected signal registration and the resulting image in less detail. The rough boundary of the investigative object and the particles that are smaller than the wavelength of a beam also result in reflecting beam scattering.

Finally, by registering the reflected sound wave one can reconstruct an image. Image reconstruction is based on the assumption that in the tissue sound waves travels at a constant speed. This assumption enables us to calculate the distance the wave has travelled from the reflective boundary to the transducer. The amplitude of the received signals will depend on the back-scattered signal and on the amount of the attenuated signals along its path. Usually, there can be two types of the scan modes that yields in a different meaning of the images produced, that is: B-scan, and M-scan. If serial ultrasound pulses are produced along the adjacent path and displayed in an image as adjacent scan lines, then such image is called B-mode image (Fig. 1.5, left-hand side). On the other hand, if consecutive ultrasound pulses are sent along the same path and the returning echoes are displayed as adjacent scan lines, an M-mode image is generated that enables us to investigate the tissue motion (Fig. 1.5, right-hand side).

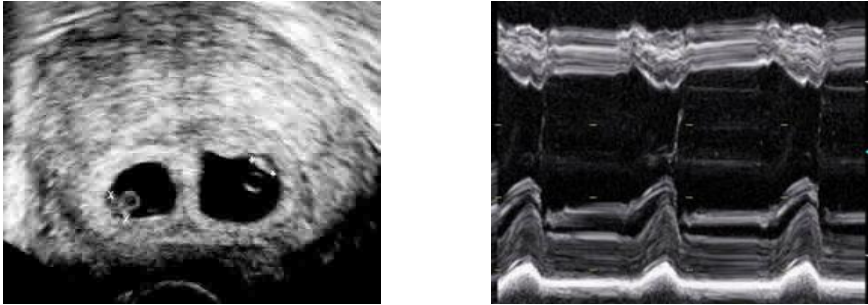


Fig. 1.5. B-scan ultrasound image (*left-hand side*), source: (The Advanced Fertility Center of Chicago 2010). M-scan ultrasound image (*right-hand side*), source: (George 2006)

In other words, the M-scan image represents pixel intensity over the time at the x axis and depth at the y axis, and the B-scan image represents pixel intensity over the distance at the x axis and the depth at the y axis of the investigative tissue.

1.4.5. Photo Acoustic Imaging

Photo acoustic imaging is a relatively new hybrid imaging modality that combines the physics of optical and ultrasound imaging (Zhang *et al.* 2009). Photo acoustic imaging is a promising complement to pulse-echo ultrasound imaging, since it provides a contrast between areas with different light absorption characteristics (Fig. 1.6.).

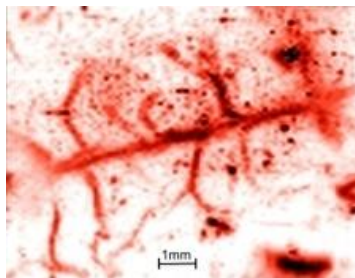


Fig. 1.6. Photo acoustic image, source: (Medical Physics and Bioengineering 2010)

Specifically, the regions with a higher blood concentration can be identified, which is useful for imaging vascularisation and the early detection of cancer (Wygant *et al.* 2005). It provides both the high contrast and spectroscopy based

specificity of optical techniques and the high spatial resolution of ultrasound. The technique involves delivering nanosecond pulses of near infrared laser or visible laser light to the surface of the skin (Zhang *et al.* 2009). Absorption of the laser energy results in a rapid thermo-elastic expansion and the emission of broadband pulses of ultrasound. Later, propagated ultrasound pulses to the surface where are detected at different spatial points using either an array of ultrasound receivers or a single mechanically scanned detector. By measuring the times-of-arrival of the ultrasound pulses at the surface and knowing the speed of sound in a tissue, an image of the absorbed optical energy distribution can be reconstructed. Spatial resolution is defined by the physics of ultrasound propagation and is limited by the frequency-dependent attenuating characteristics of a soft tissue. The image contrast, on the other hand, is based largely on optical absorption, which means that the technique is particularly well suited to imaging blood vessels due to the strong optical absorption of haemoglobin.

1.4.6. Thermovisual Imaging

Thermovisual imaging can also be referred as infrared (medium or long wavelength infrared) imaging and it is not a new concept in the evaluation of objects. Basically, infrared imaging, also known as thermovisual imaging, converts thermal fluxes into a human perceptual form. In other words, every physical body radiate varying length infrared waves if the temperature of the body is higher than absolute zero (Fig. 1.7.).



Fig. 1.7. Thermovisual image

The intensity of the radiated energy is proportional to the body temperature or molecular kinetic energy and also depends on the substance itself. New technological achievements in infrared imaging, such as advanced uncooled microbolometer focal plane array (FPA), detector technology, delivers high resolution long wave infrared images that allow us to determine thermal variances as low as 0.12 °C. Real time scanning at standard video rates (up to

60 Hertz) enable us to see rapid, thermally transient events, which gives an opportunity to visualize temperature dynamics of the investigative object (Lekas *et al.* 2009). However, it is necessary to note that a thermal image shows the emitted, transmitted and reflected infrared energy from the object. This property can be efficiently used in testing the electric component connectivity (Izmailov *et al.* 2009) or in building heat emission (Avdelidis and Moropoulou 2003). Another wide context in which thermovisual imaging can be used is medicine. (Veikutis *et al.* 2008) diagnose ischemic damage of myocardium and state that it is an important problem to see the coronary arteries blood circulation in open-heart surgery. Insufficient blood circulation results in tissue temperature dropdown which can be monitored by means of thermovisual imaging. The dropdown of temperature may lead to a serious influence on post-operation complications or even mortality. Other investigations of the same author disclose the characteristics of non-contact temperature registration method and the possibility to estimate the effect of application of radiofrequency energy to different heart structures, using standard intra-cardiac electrodes (Veikutis *et al.* 2008b).

1.4.7. Ophthalmology Imaging

The majority of perceptual information humans get using their eyes. A human eye is a complicated system of neuro-receptors which is able to receive and analyse the electromagnetic waves from the visible part of electromagnetic spectrum. The reliable and early diagnosis of the eye disease typically depends on the observation of even minimal or slight alterations in eye structures. When the functional disorders comes in play there is nothing more than patients reaction to the pathological process. These disorders are informative for the diagnostic process itself, however, for an ophthalmologist the morphological criteria are more important (such as the optic nerve disc size, the size of excavation, etc.). These criteria allow us to distinguish a healthy eye tissue or structure from the diseased one (Janulevičienė *et al.* 2008). The main and most informative way of investigating the optic nerve disc and eye fundus is ophthalmoscopy. Basically, there are four main methods for the eye fundus examination.

First and the simplest one, is when physician investigates eye fundus with a powerful magnifying lens. Lens provides an inexpensive, fast, and easy way of investigation, however, it has some drawbacks. Depending on the distance between the investigative eye and the lens, the magnification errors may occur, especially when a high degree of refraction is present. Another drawback of this method is that in the case of myopia, the optic nerve disc is seen too small, and in the case of hypermetropy it is seen too large.

Second method relies on the laser scanning technology. This principle filters out all the reflected laser beams which do not come from the focal plane object. Thus, laser has to scan the whole fundus point by point. This is done by two vibrating lenses which are arranged on the path of reflecting beam. This is a fast and objective technique to investigate the eye fundus and does not require to apply a pupil mydriasis procedure. But the main disadvantage of this technique is that the physician has to subjectively measure the size of optic nerve disc.

The third method is optical coherence tomography. The operation of a tomograph is based on the near-infrared laser wavelength interval. It uses two beams to investigate the eye fundus. Basically, owing to the different reflection times of the beams from different structures of the eye it is possible to compute the depth. Thus, by scanning region by region of the eye, one can construct a three-dimensional model of the fundus. This method automatically calculates the size of the optic nerve disc, but it is very expensive and needs a mydriasis procedure, and the scanning template is fitted to the average eye axis length.

The fourth method is an eye fundus photography. The image of the patient's eye fundus is taken by a special camera connected to the microscope, if eye drops are applied in dilation. Then the microscope saves the obtained image for further investigation. This method is relatively cheap and fast, however, the size of the optic nerve disc has to be measured subjectively.

A high quality colour photograph of the eye fundus (Fig. 1.8.) is helpful in the accommodation and follow-up of the development of the eye disease.

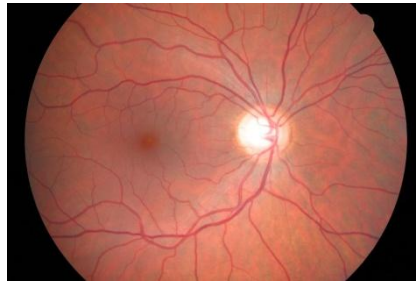


Fig. 1.8. Eye fundus image

However, evaluation of the eye fundus images is complicated because of the variety of anatomical structure and possible fundus changes in eye diseases (Osarech 2004). Sometimes it requires high-skilled experts for evaluation.

The ways of a better fundus image evaluation is the use of modern information technologies for processing and parameterization of the main structures of the eye fundus (Treigys *et al.* 2006). There are three main structures in the eye fundus image, used for making a diagnosis in ophthalmology (Treigys *et al.* 2008b):

- Optic nerve disc.
- Blood vessels (retinal arteries and veins).
- Retina.

The optic nerve disc appears in the normal eye fundus image as a yellowish disc with whitish central cupping (excavation) through which the central retinal artery and vein pass.

The eye fundus images used in this dissertation were collected in the Department of Ophthalmology of the Institute for Biomedical Research of Kaunas University of Medicine (BRKU), using the fundus camera *Canon CF-60UVi*, at a 60° angle. 6.3 Mpixel images (image size 3072 by 2048 pixels) were taken. The magnification quotient is 0.0065248 mm/pixels, common magnification quotient for the system eye fundus camera is 0.556782 ± 0.000827 (mean \pm SD). The scale (mm to pixel) for the fundus camera is 0.01171875 mm per pixel.

1.5. Conclusions for the First Section

New information technologies provide a possibility of collecting a large amount of medical images into databases. The greatest part of the collected data in medical practice is unsupervised. This fact naturally raises a doubt about data usefulness. The aim of pattern recognition is to find the ways and means to automate the decision making process, which later could lead to a better unsupervised data classification or pattern recognition. Thus, the techniques of data mining, pattern recognition, and knowledge discovery can be efficiently used and allow us to automate processing of images for clinical decision.

The overview of medical image formation principles provides the idea for a new knowledge discovery. The collected data cannot be examined in detail by a human since the amount is too large, however, it provides the crucial information on the state of the patient.

For example, changes in the eye fundus can be associated either with numerous vision threatening diseases such as glaucoma, optic neuropathy, swelling of the optic nerve disc, or related to some systemic disease. Finally, tracking the progress of a possible disease of the patient becomes very difficult due to numerous anatomical structures, such as tree of blood vessels, fovea, macula, excavation, etc. Moreover, the structures does not have the predefined place or the size and may emerge in the image at different locations.

Investigation of Blood Vessels in Eye Fundus Images

The initial source of information on the state of disease of patient ophthalmologists obtains from the eye fundus images. When examining eye fundus, it is very important for an ophthalmologist to recognize the optic nerve disc as well as qualificatory parameters in the colour retinal images quickly. Later, these parameters could be used to identify numerous ophthalmologic disease cases. However, in the automated case of optic nerve disc identification, the problems that cause the tree of eye fundus vasculature should be overcome. The opposite task of the blood vessel tree extraction will be considered as well.

2.1. Survey of Methods for Vasculature Processing in Eye Fundus Images

In everyday clinical practice a physician describes or sketches eye fundus taken under examination. In this case, the eye fundus examined is a matter of subject. The eye fundus imaging is an objective method which can further be evaluated by hand. Presently, eye fundus images can be stored in digital form and furthermore such images can be analysed by automated means.

One of the main tasks in the ophthalmologist practice is parameterization of the optic nerve disc. This is only possible in vivid (qualitative, explicit anatomical structure) images. This makes the task very difficult, since automated methods have to locate the position of the optic nerve disc and apply some parametric form in order to observe the possible changes in the future examinations.

In order to search for the optic nerve disc in retinal images, it is important to eliminate the noise. The noise in automated localization and parameterization is apprehensible as a structure of vasculature, since vessels pass through the optic nerve disc (Treigys 2005b). Thus, the analysis of methods for removing blood vessel forms one of section task. Basically, almost all segmentation methods work on a gradient image and lock onto homogeneous regions enclosed by strong gradient information. This task is extremely difficult in our context since the region of the optic nerve disc, as mentioned before, is invariably fragmented into multiple regions by the blood vessels. By applying some mathematical morphological operations we will show that this technique is suitable for the vasculature extraction and elimination tasks.

Mathematical morphological operations for the colour images have not been widely explored. According to (Mendels *et al.* 1999) mathematical morphological operations were applied on luminance images of YIQ colour system. However the initial data set of the eye fundus pictures was scanned from the slide photos of the eye with the resolution of 285 by 400 pixels. This definitely results in loss of information or signal distortion by the scanner itself. Another lack is that the authors do not prove the necessity of conversion from RGB to as well as application of mathematical morphology operations only to luminance domain.

The HSL (hue, saturation, lightness) colour space tends to describe perceptual colour relations in more detail than the RGB colour space does. The mathematical morphology has been investigated in this colour space by (Peters 1997; Handbury and Serra 2001). It is a computational cost-effective model for colour representation. However, most problematic is the hue domain described by $H \in [0, 2\pi)$, though domain lightness and saturation are linear components and can be ordered as real numbers. It means that component H is a unit circle that has neither relevant order nor dominant position. It follows that we cannot construct a lattice on a unit circle if we do not assign it to some arbitrary origin (Vardavoulia *et al.* 2002). The same problem results in the HSV (hue, saturation, value) colour space (Louverdis *et al.* 2002). Depending on the hue origin, different orders and intuitive sense of what is lower or higher disappear. Moreover, the lexicographical order should be introduced when we talk about the pair of points that lie on the same surface. There are many techniques for the automated hue origin selection (Handbury and Serra 2001),

but all of them have disadvantages – we need a priori information about the colour to be preserved in the image. For example, if the origin is set to 0, then it means that the overall image will be processed taking into account the red colour representation.

Later on, the principles described above were applied to the *Lab* colour space, where $\{L\}$ is luminance, $\{a\}$ stands for the distance between the red and green colours, and $\{b\}$ is the distance between the yellow and blue colours. Also, the authors have adapted the scheme to the *Lch* colour space as well. Here c stands for $c = \sqrt{a^2 + b^2}$ and h stands for $h = \tan^{-1} \frac{b}{a}$ (Handbury and Serra 2002).

The opposite task is automated extraction of the vasculature from eye fundus images. The methods for extracting vasculature can be assigned to one of the three groups: kernel-based, classifier-based and tracing-based (Vermer *et al.* 2004). In the kernel-based methods, an image is convolved with a predefined kernel in most cases. Further, the Gaussian filter is introduced in order to model cross-section of the vessels. Afterwards the vessel identification filters (Hoover and Goldbourn 2003) are applied. Such a class of vasculature structure extraction algorithms is commonly modelled together with artificial neural networks (Matsopoulos *et al.* 2004) and is a very time-consuming task. Classification-based methods are composed of two steps. During the first step, segmentation of an image is performed. Segmentation (Staal *et al.* 2004; Soares *et al.* 2006) is basically accomplished by the kernel-based methods. In the second step, a set of features has to be provided for the algorithm. Such a set describes the vessels visible in the image. These methods that belong to this class allow processing of the objects with complex structures (Chanwimaluang *et al.* 2006). This enables algorithms to run faster, however, these algorithms cannot be automatic in most cases. In the tracing-based class of algorithms (Dongxiang *et al.* 2000), the algorithm traces the structure of a vessel between predefined points. Basically tracing ends at the provided reference points. It is common that these reference points are provided interactively by the human.

2.2. Elimination of Vasculature from Colour Eye Fundus Images

The main disadvantage in the ophthalmologist practice and automated eye fundus processing is that the optic nerve disc can appear anywhere in the image. The size of the optic nerve disc varies and, moreover, it is invariantly segmented by the vessels. Thus, the use of mathematical morphological operations was introduced, since they do not depend neither on location of the objects in the

image nor on the size of the object to be preserved. Mathematical morphological operations typically process an image with a small shape or template known as a structuring element. The four basic morphological operations are erosion, dilation, opening, and closing (Soille 1999). Further, we will explore the basics of mathematical morphological operations.

2.2.1. Mathematical Morphology on Binary Images

Each image naturally can be described by a heap or set of discrete or continuous coordinates. Assume that subsets in the set represent some points of objects. In Fig. 2.1, two objects I and Z are presented. It should be noted that the presence of the coordinate systems is necessary (Young *et al.* 2003).

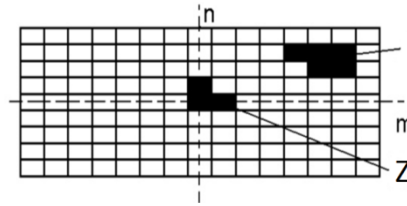


Fig. 2.1. Two objects on the Cartesian grid, source: (Young *et al.* 2003)

Further, assume that object I is comprised of points o , all of which satisfy the same property $I = \{o | \text{property}(o) = \text{True}\}$. According to the coordinate system, object Z is described by the coordinates: $\{[0,0], [1,0], [0,1]\}$ (Fig. 2.1).

The basic operations that can be associated with object I are: translation, union, intersection, and complement.

The translation $(I + x)$ of object I can be defined by $I + x = \{o + x | o \in I\}$, when x stands for a vector and I is an object. It should be noted that some restrictions have to be applied to the vector x , since the digital image is composed of pixels at the integer coordinate positions.

It is substantial to observe that every element that comprises set Z is not only a pixel, but also a vector, since it has a precise position with respect to the origin of $[0,0]$. If we have two sets I and Z , then the Minkowski addition and subtraction can be defined as follows:

$$I \oplus Z = \bigcup_{z \in Z} (I + z), \quad (2.1)$$

$$I \ominus Z = \bigcap_{z \in Z} (I + z). \quad (2.2)$$

In view of the Minkowski equations fundamental operations of the mathematical morphology, such as erosion and dilation, will be depicted as:

$$D(I, Z) = I \oplus Z = \cup_{z \in Z} (I + z), \tag{2.3}$$

$$E(I, Z) = I \ominus (-Z) = \cap_{z \in Z} (I - z). \tag{2.4}$$

where $(-Z) = \{-z | z \in Z\}$. The result of dilation and erosion is presented in Fig. 2.2. Finally, the complement of set I is assumed to be a background and is defined as $I^c = \{o | o \notin I\}$.

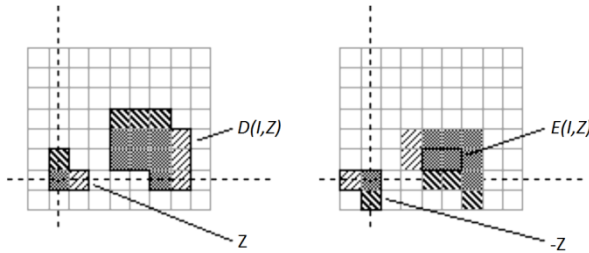


Fig. 2.2. Dilation (left-hand side), erosion (right-hand side), source: (Young *et al.* 2003)

Both of the sets, I or Z , can be treated as an image, however, in practice set I is assumed to be the image and set Z is called a structuring element.

Dilation and erosion on binary images are closely related to the convolution operations over the Boolean algebra. Hence it can be described in terms of logical operations. There is a similarity between the convolution operations and that of mathematical morphology, both of them analyse neighbouring pixels according to the provided structuring element. The structuring element essentially describes the structure to be kept in the image. If one uses a round-shaped structuring element, then the structure of round objects will be kept in the image. In a separate case, a rectangular structuring element preserves a linear structure, however, it namely depends on the orientation of rectangular structuring element whether the structure preserved will be horizontal or vertical.

Let us explore the erosion in detail, assuming that the structuring element is described by $[1,1,0]$ and is of horizontal orientation. The value of the point under analysis depends on the logical multiplication followed by addition. That is, the investigative point becomes equal to 1 only if all the points overlaid by the structuring element (including the investigative itself) are equal to one. In the opposite case, the investigative point becomes 0. The scheme of erosion is presented in Fig. 2.3. Here the origin is at coordinates $(0,0)$.

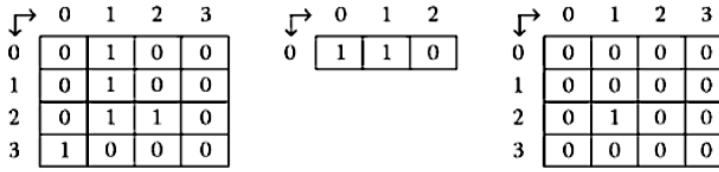


Fig. 2.3. The scheme of the binary erosion, source: (Shih 2009)

A dilation operation is example of the opposite effect. Let the structuring element to be of form [1,0,1]. This operation will cause the white regions in the binary image to shrink. Actually, not necessary are the white regions, they also can be black; since it depends on the agreement whether white means 1 or 0. All the circumstances under which the erosion is acting are valid for dilation as well. Yet the logical operations applied are addition followed by multiplication. The scheme of dilation is presented in Fig. 2.4.

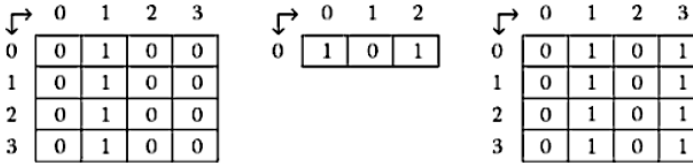


Fig. 2.4. The scheme of the binary dilation source: (Shih 2009)

Fig. 2.4 and Fig. 2.3 shows the initial binary image on the left-hand side, in the middle there is a structuring element, and on the right-hand side we see the binary image after erosion and dilation. A combination of the dilation and erosion operations allows building higher order mathematical morphological operations:

$$C(I, Z) = E(D(I, -Z), -Z), \tag{2.5}$$

$$O(I, Z) = D(E(I, Z), Z). \tag{2.6}$$

Here $C(I, Z)$ stands for closing and $O(I, Z)$ stands for opening operations.

2.2.2. Mathematical Morphology on Intensity Images

Basically mathematical morphological operations are applicable to binary images, but the operations such as erosion, dilation, closing, and opening can be applied to intensity images as well. Erosion and dilation in intensity images matches the non-linear search for minimum or maximum.

The intensity image erosion can be described as a calculation of the minimum pixel value within the structuring element centred on the current pixel $O_{i,j}$. Denoting an intensity image by I and a structuring element by Z , the erosion operation is defined at a particular pixel (x, y) as:

$$E(I, Z) = \min_{(i,j) \in Z} (I_{x+i,y+j}), \tag{2.7}$$

where i and j are index of the pixel of Z .

The intensity image dilation is considered in a dual manner and thus can be written as:

$$D(I, Z) = \max_{(i,j) \in Z} (I_{x+i,y+j}). \tag{2.8}$$

The scheme of the search for the maximum is presented in Fig. 2.5

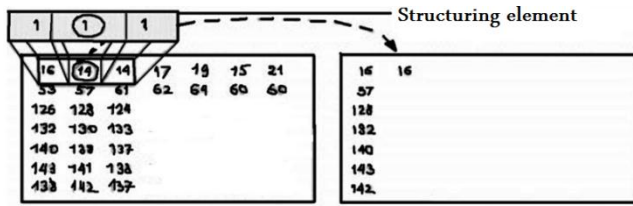


Fig. 2.5. Dilation of intensity images, source: (The MathWorks 2010)

Fig. 2.5 represents the scheme of the dilation operation. Boxed rectangles on the background are assumed to be the image before the dilation (left-hand side) and the resulting image after the dilation (right-hand side). The numbers in rectangles mean intensity values. In the foreground a rectangular structuring element is shown. A rounded middle cell of the structuring element means that the intensity value can be changed in the resulting image. The intensity value of the rounded element will be changed to the maximum value of the neighbouring values overlaid by the structuring element.

By introducing dilation and erosion we arrive at higher order mathematical morphological operations. The opening of an image is defined as erosion followed by dilation:

$$O(I, Z) = D(E(I, Z), Z) = \max_{(i,j) \in Z} (\min_{(i,j) \in Z} (I_{x+i,y+j})). \tag{2.9}$$

In a dual manner the image closing includes dilation followed by erosion. Thus, the mathematical morphological operation as closing can be defined as follows:

$$C(I, Z) = E(D(I, Z), Z) = \min_{(i,j) \in Z} (\max_{(i,j) \in Z} (I_{x+i,y+j})). \tag{2.10}$$

The closing operator usually smoothes away the small-scale dark structures from intensity retinal images. As closing only eliminates the image details smaller than the structuring element used, it is convenient to set the structuring element large enough to cover all possible vascular structures, but still small enough to keep the actual edge of the OND. However, the fundamental concepts of mathematical morphology operations in intensity images cannot be directly applied to colour ones (Goutsias *et al.* 1995).

2.2.3. Mathematical Morphology on Colour Images

It is well known that every pixel in a colour image can be described by three components, namely: red $\{R\}$ channel, green $\{G\}$ channel, and blue $\{B\}$ channel pixel intensity values. Then, every image that consists of N by M pixels can be described by three separate matrices: $\{R\}$, $\{G\}$, and $\{B\}$, where $x = 1, \dots, N$; $y = 1, \dots, M$. If we assume that each of these matrices represents the intensity image I (Fig. 2.6), then we can apply the mathematical morphological closing operation (2.10) to each matrix with some structuring element.

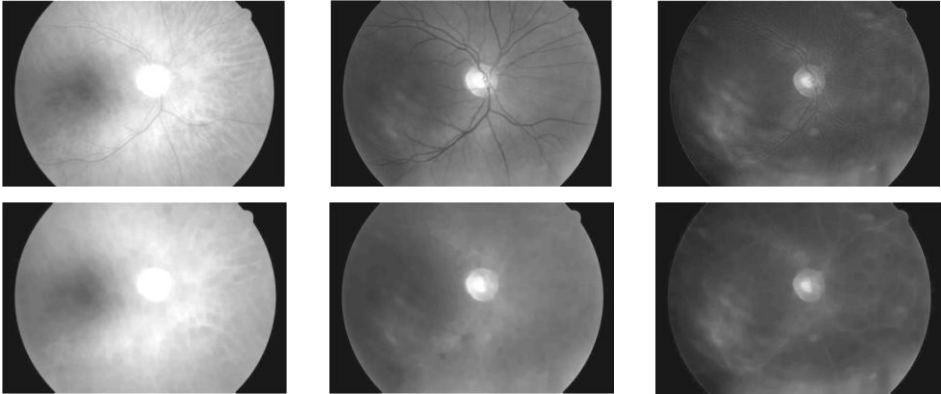


Fig. 2.6. Colour image decomposed into colour vectors (*top row*), images after mathematical morphological closing (*bottom row*)

As mentioned in Section 2.2.1, the structuring element describes the shape of the objects to be preserved in the image. In our case, since we want to remove the linear-shaped elements, i. e., the tree of the vasculature, we used a disc-shaped structuring element (Fig. 2.7). It should be noted that zeros in the figure represent pixels covered by the structuring element in the image and do not have any effect on the operation (2.10). The meaning of the element in the figure is the same as that explained in Fig. 2.5 (see Section 2.2.2). The intensity

value at the location of the point of interest may be changed according to the surrounding pixel intensity values. It is exactly the surrounding pixels that describe the structuring element's members set to one.

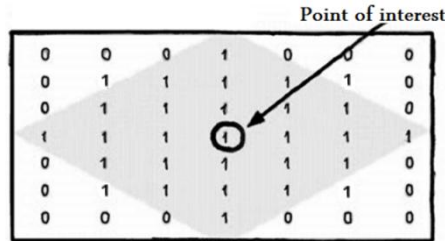


Fig. 2.7. Disc-shaped structuring element with the diameter of 7 pixels, source: (The MathWorks 2010)

Fig. 2.7 shows a disc-shaped structuring element. The diameter of the structuring element should not be smaller than the widest vessel underlying in the image. After a careful analysis, the diameter of the disc-shaped structuring element was chosen experimentally equal to 14 pixels. We explored that the vessels in the eye fundus images, provided by the medics, were not wider than 14 pixels.

2.2.4. Recombination of the Results

After decomposing the retinal image into $\{R\}$, $\{G\}$, $\{B\}$ channels and processing each channel separately, we can recombine the results. However, a recombined result is not valid in general.

As described by (Peters 1997), let us consider a separate erosion of $\{R\}$, $\{G\}$, and $\{B\}$ channels, using the structuring element Z . Each pixel after erosion $E(\{R\}, Z)$ is the minimum value of initial R within the structuring element neighbourhood of the pixel. Descriptions of $E(\{G\}, Z)$ and $E(\{B\}, Z)$ are similar. The problem is that the minimum is valid only for the separate $\{R\}$, $\{G\}$, and $\{B\}$ bands. After we recombine those separate bands into a structure for colour representation, it becomes not clear which minimum should be used. Thus, this fact violates the property of erosion (2.7), where the minimum has to be over all the three channels within the structuring element Z . The same scheme is valid for dilation.

However, the recombination of processed bands of the retinal image does not introduce a colour distortion and we achieve a closed colour retinal image (Fig. 2.8). The colour distortion is avoided because, in general, the mathematical morphological closing fills the dark holes in bright regions. Further, the optic nerve disc is a bright region in the retinal image, and the brighter the region, the

higher the value of each band's pixel brightness. Hence, by selecting an appropriate structuring element's size, we eliminate dark regions formed by the vasculature and replace them by the surrounding brighter region, located around the vessels replaced.

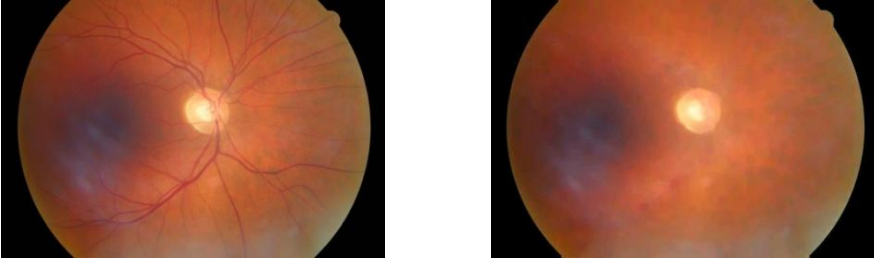


Fig. 2.8. The initial (*left-hand side*) and closed (*right-hand side*) retinal images

In this sub-section the principles of mathematical morphology operations were discussed. The first step for the blood vessel removal from eye fundus is to decompose the image to separate colour channels. Then the mathematical morphology closing operation with disc-shaped structuring element was applied over them. The analysis of the structuring element size showed that it is sufficient to use the element with the radius of 7 pixels. Despite the fact that the recombination of the processed channels into a colour representation is not valid in terms of mathematical morphology we were able to remove the structure of the blood vessels from the optic nerve disc area.

2.3. Extraction of Vasculature from Eye Fundus Images

The structure of the eye fundus vasculature in the retinal images is very important in terms of making medical diagnoses (Šaltenis and Treigys 2005). In some medical aspects, the structure of vasculature is the main objective of investigation, in other – it becomes nothing more than noise (Treigys 2005a). It depends on the topics of investigation. Yet the information provided by the structure of the vasculature can be used by ophthalmologist in various ways. The practice shows that this information can be used to diagnose the stage of a predefined disease or as supplementary information to diagnose the disease itself. The analysis based on the information from the eye fundus vasculature can benefit in watching the pathological changes influenced by such diseases as

diabetes, hypertension, atherosclerosis (Thitiporn and Guoliang 2003; Lowell *et al.* 2004).

2.3.1. Image Pre-processing

In order to calculate the monochrome luminance (conversion to intensity image) of a colour image, we need to apply coefficients related with the eye's sensitivity to each of the RGB channel. This is performed according to (Johnson 2006) and can be expressed by:

$$I(x, y) = 0.3R(x, y) + 0.59G(x, y) + 0.11B(x, y). \quad (2.11)$$

for each $x = 0, \dots, N - 1$; $y = 0, \dots, M - 1$. Here, functions $R(x, y)$, $G(x, y)$, and $B(x, y)$ returns the specific intensity value of the channel at the position of (x, y) . I is the intensity image with integer values ranging from the minimum of zero, to the maximum of 255.

Let the variable I_1 represent the initial eye fundus image converted to the monochrome luminance. Also, let the variable I_2 represent the monochrome luminance image after the mathematical morphological closing operation (see Section 2.2.2). The results of conversion from the colour representation to the monochrome luminance and the closing operation are presented in Fig. 2.9.

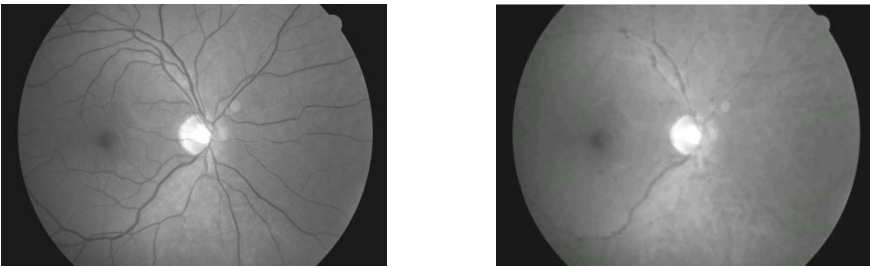


Fig. 2.9. Intensity retinal image (*left-hand side*), closed intensity retinal image (*right-hand side*)

2.3.2. Equalization of Histogram

In order to see the differences of two spatial images, the technique of intensity value subtraction is frequently used. This operation can be defined as follows: $A(x, y) = |I_1(x, y) - I_2(x, y)|$. After this operation (for each $x = 0, \dots, N - 1$; $y = 0, \dots, M - 1$), if, at a particular time there are no changes in the spatial domain, the subtracted intensity values acquire the value of 0, otherwise, if there are some differences, the intensity value does not become 0. In order to visualize the subtracted image, we have to apply the intensity adjustment procedure (Fig. 2.10). This is needed because the vessel intensity values in colour images

are very low compared to the surrounding background of the retinal image. This result from the subtraction operation where the image achieved is nothing more than a black rectangle.

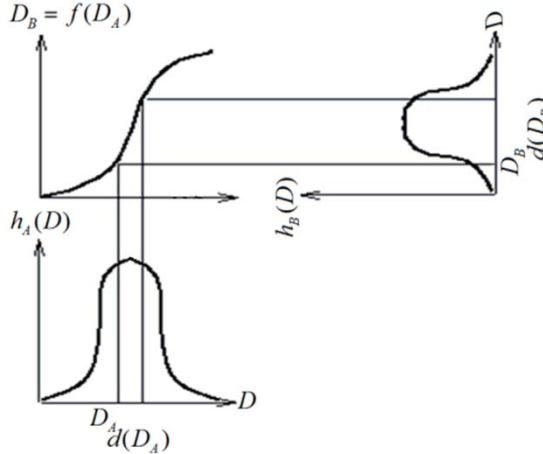


Fig. 2.10. The sample transformation function

In Fig. 2.10 upper left corner represents desirable unknown function for intensity transformation. Further we will show, that values of this function are proportional to the intensity distribution function values of the investigative image A see (2.16).

The intensity adjustment procedure can mainly be described in this way. Assume that the distribution of intensity values of the subtracted image A and the transformation function $f(D_A)$ are continuous in the interval $[0,1]$ (Gonzalez and Woods 1992). Moreover, assume that the transfer function is single-valued $D_A = f^{-1}(D_B)$ and also, monotonically increasing (see Fig. 2.10). Then the real intensity levels, in the shown interval, will be recalculated using the function f to the desired intensity levels in a desired interval.

Densities of all the initial image histogram intensities in the interval $[D_A, D_A + d(D_A)]$ will be recalculated in the desired interval $[D_B, D_B + d(D_B)]$. The surface areas $h_A(D_A)dD_A$ and $h_B(D_B)dD_B$ will be equal (Fisher *et al.* 2007). Hence, if the histogram h is a continuous probability function p that depicts the distribution of intensities, then one can write:

$$p_B(D_B) = \frac{p_A(D_A)}{d(D_A)}. \quad (2.12)$$

All the output probability densities should be an equal fraction of the maximum number of intensity levels in the input image, hence:

$$p_B(D_B) = \frac{1}{D_M}. \quad (2.13)$$

where $D_M = \max(D_B) = 255$ while $\min(D_B) = 0$. Thus, we arrive at:

$$d(D_A) = \frac{df(D_A)}{dD_A} = D_M F_A(D_A). \quad (2.14)$$

Further, by substituting D_A with u and by rearranging (2.14) to:

$$df(u) = D_M p_A(u) du. \quad (2.15)$$

we integrate both sides of the formula:

$$f(D_A) = D_M \int_0^{D_A} p_A(u) du = D_M F_A(D_A). \quad (2.16)$$

Here $F_A(D_A)$ is the histogram of point intensities obtained from the initial image (probability distribution). Hence, such a point intensity recalculation flattens the histogram and spreads the intensities over the desired intensity interval. In a discrete computational form it can be written as follows:

$$f(D_A) = \max(0, \text{round} \left[D_M \frac{n_k}{NM} \right]), \quad (2.17)$$

whereas N is the height of the image in pixels, M is the width of the image in pixels and n_k is the sum of pixels which intensity level is k or lower. The result of intensity adjustment is shown in Fig. 2.11.

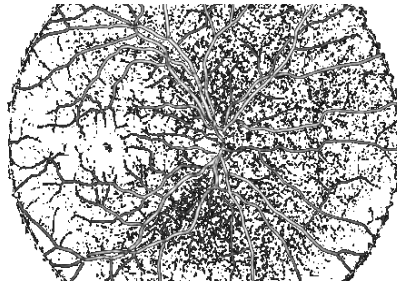


Fig. 2.11. Subtracted image after the intensity adjustment

The Gamma correction factor was set to 1. It means that the transformation function $f(D_A)$ is nearly linear.

2.3.3. Otsu Threshold

By introducing mathematical morphological operations with a view to remove the vasculature, the areas of the outlier points can be seen. The outliers are points which do not belong to the tree of the vasculature. Also, it should be

stated that the intensity levels of the outlier points is considerably lower than that belonging to the tree of the vasculature. This implies that the outlier points have to be removed somehow. It means that the intensity image has to be converted to a binary one, where the foreground is assumed to be the tree of the vasculature and set to white, and the background with all the outliers has to be set to black. Thus, for an automated threshold level calculation, we use Otsu's method based on the weighted histogram calculation (Otsu 1979). Otsu's method maximizes the between-class variance $\sigma_B^2(\tau_1)$ given by:

$$\sigma_B^2(\tau_1) = \omega(\tau_1)(1 - \omega(\tau_1))(\mu_1(\tau_1) - \mu_2(\tau_1))^2, \quad (2.18)$$

where $\omega(\tau_1) = \sum_{i=0}^{\tau_1} \frac{n_i}{N}$, $\mu_1(\tau_1) = \sum_{i=0}^{\tau_1} i \frac{n_i}{N}$, $\mu_2(\tau_1) = \sum_{i=\tau_1}^{L-1} i \frac{n_i}{N}$.

The optimal threshold τ_1 is found by Otsu's method through a sequential search for the maximum of $\max_{0 \leq \tau_1 < L} \sigma_B^2(\tau_1)$ of τ_1 , where n_i represents the number of pixels at the intensity i , L is the number of intensities, and N is the total number of pixels in the image (Tian *et al.* 2003).

Fig. 2.12 represents the tree of vasculature (coloured part) of the retinal image.

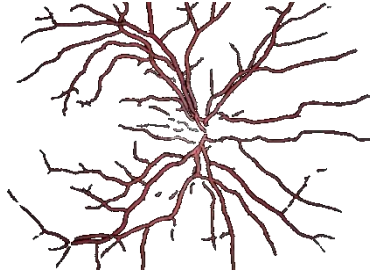


Fig. 2.12. Tree of the vasculature after the threshold application

In this sub-section the opposite task to the blood vessel elimination from eye fundus images was investigated. The proposed method for the blood vessel tree extraction rely on the resulting image after elimination algorithm. Next, the subtraction of pixel intensities is applied over vessel-free and the initial eye fundus images. The resulting image contains the structure of the vasculature and the noise generated by elimination algorithm. The noise was removed by thresholding the equalized image. For the threshold level calculation the Otsu algorithm was introduced and allowed us to automate the task of blood vessel extraction from eye fundus images.

2.4. Conclusions for the Second Section

The tasks of automated blood vessel elimination and extraction were considered in this section. The investigation of the automated optic nerve disc localization and parameterization problem has highlighted that it is only possible in vivid (qualitative, explicit anatomical structure) images. Thus, employment of the segmentation methods does not fit in this context, since they work on a gradient image and lock onto homogeneous regions enclosed by strong gradient information. The task of the robust automated blood vessel elimination from eye fundus images was solved by introducing mathematical morphological closing operation to a separate colour channels with 7 pixel radius disc-shaped structuring element. Further, the recombination of processed channels into a colour representation showed that the tree of the blood vessels was efficiently eliminated from eye fundus image while keeping the actual edges of the optic nerve disc.

The opposite task for the automated extraction of the blood vessel tree was investigated in this section also. Analysis of the literature has disclosed that vasculature extraction methods from retinal images can be classified into one of the groups: kernel, classifier, and tracing based. However, these groups of algorithms cannot be automated in most cases and require either a priori knowledge of the structures of vasculature, either some human interaction. Moreover, they use the line-shaped structuring elements that cannot process every image pixel of blood vessel. We have showed that the combination of the elimination algorithm, histogram equalization and non-static image thresholding methods, robust extraction of the vasculature from the eye fundus images becomes possible in an automated way with a disc-shaped structuring element.

Investigation of Optic Nerve Disc in Eye Fundus Images

Automated localization and parameterization of the optic nerve disc is particularly important in making a diagnosis of glaucoma, because the main symptoms in these cases are relations between the optic nerve disc and the excavation parameters. In this section we will describe the algorithm for the automated optic nerve disc localization and parameterization by an ellipse in colour eye fundus images. It is assumed that for the optic nerve disc localization and parameterization task, the blood vessel tree is eliminated from eye fundus image according to algorithm provided in Section 2.2.

3.1. Survey of Methods for Optic Nerve Disc Localization in Eye Fundus Images

The optic nerve disc is the main structure for localizing other eye fundus structures as well as a very important structure for diagnosing some eye and neurological diseases. As mentioned before, the optic nerve disc appears in the normal eye fundus image as a yellowish disc with whitish central cupping (excavation) through which the central retinal artery and vein pass

(Jegelevicius *et al.* 2008). Changes of the optic nerve disc can be associated with numerous vision threatening diseases such as glaucoma, optic neuropathy, swelling of the optic nerve disc, uveal melanoma or related to some systemic disease (Jegelevicius *et al.* 2002; Zupan *et al.* 1997).

This section focuses on automated optic nerve disc (OND) localization and approximation by an ellipse in retinal images with the aim to produce the parametric form of it. The intensity of the optic nerve disc is much higher than the surrounding retinal background. Thus the position of OND can roughly be estimated by finding the region or point with the maximum variance (Sinthanayothin *et al.* 1999). However, such a straightforward method often fails due to non-uniform illumination or photographic noise seen in the retinal images.

Moreover, this problem is extremely difficult since, in general, the OND in the eye fundus image does not have a homogenous structure. This is due to a vascular tree within the optic nerve disc, and we have to deal with a colour images. Thus, the algorithm that removes the vasculature but keeps the actual edges of the optic nerve disc in eye fundus image provided in Section 2.2 was applied.

The first problem of automated OND localization is to identify its position in retinal images. In the literature, there are many algorithms for OND localization. Basically these methods deal with image segmentation, dynamic contours and geometric models.

In (Sinthanayothin *et al.* 1999; Boyd 1996), the vessel detection and convergence analysis are based on the region of nearly vertical vessels emanating in the area of OND. This algorithm led the authors to achieve an accuracy of 80 %. A separate case of convergence analysis is introduced in (Hoover and Goldbourn 2003). Here every vessel forms a separate line and the voting for the constructed lines is performed. Since this is an extension of methods (Boyd 1996; Chaudhuri *et al.* 1989), this provides the accuracy of 89 %. In the paper (Tobin *et al.* 2006) is described an accurate vasculature segmentation method and achieve the localization accuracy up to 87 %. Also segmentation method is presented in paper (Grau *et al.* 2006). In this paper authors discusses anisotropic Markov random field models for gathering prior knowledge of the geometry of the optic nerve disc structure. A different approach was used in (Goldbaum *et al.* 1996), where the main idea is segmentation accomplished by using matched spatial filters of bright and dark blobs. However, quantitative results for nerve localization were not provided. In (Pinz *et al.* 1998) the localization of optical nerve disc is accomplished by segmenting a retinal image into vessels, fovea, and nerve. The lack of this method is that the authors have a priori knowledge where OND is in the retinal image, and the data set used was very small. The accuracy of this method is

91 %. Segmentation and the vessel tracking methods are also presented in (Tolias and Panas 1998). Nerve localization is based on the brightest region search in a restricted third of the image. The testing data set consisted only of three fundus images, so the results are very questionable. The use of active dynamic contours, described in (Morris and Donnison 1999), is introduced, too. The main idea is that edge gradients and terminations in the image are converted into energies. This covers the actual OND by a curve. This approach is explored in article (Xu *et al.* 2007). In this article authors present modified active contour algorithm by introducing knowledge-based clustering and smoothing update techniques. This allow authors to achieve better success rate (94 %) compared to standard gradient vector flow snake model 12 %. Geometric models, presented in (Foracchia *et al.* 2004), probe the fundus image in a spatial or frequency domain with a predefined model for optic nerve disc localization. Another approach is presented in (Lowell *et al.* 2004). Here authors deals with blurred images from diabetic screening programme. Article incorporates specialized template matching filters and active segmentation methods for OND localization and leads to accuracy of edge excellent-fair performance (evaluated by ophthalmologist) of 83 %. Almost all of these methods rely on the quality of vasculature segmentation.

The automated optic nerve disc approximation by a parametric curve such as an ellipse is a second goal of this section. Of course, 3D model parameters of optic disc could be much more informative, but this is not possible to explore, since this problem is related to the equipment involved with 3D photography.

The analysis of the literature showed that the OND parameterization is insufficiently explored. The research is mostly concentrated on exudates, drusen detection and parameterization, but not the optic nerve disc itself.

Further, we will describe an algorithm for OND localization in retinal images and parameterization by an ellipse.

Use of new information technologies provides a possibility of collecting a large amount of fundus images into databases. It allows us to use automated processing and classification of images for clinical decisions.

The automated localization and parameterization of the optic nerve disc is particularly important in making a diagnosis of glaucoma, because the main symptoms in these cases are links between the optic nerve and cupping parameters and differences in the symmetry between eyes. Besides, tracking of the disease progress is almost impossible without a quantitative change in patient's fundus images with the lapse of time. Thus, the parameterization of the optic nerve disc is crucial.

3.2. Localization of the Optic Nerve Disc

In order to localize OND, first of all we have to pre-process an image. The first step of image pre-processing is accomplished by scaling down the retinal image to the size of 768 times 512 pixels. Scaling is performed in order to decrease the computation time. Basically the circular Hough transform is the most time consuming procedure, since for every pixel in a spatial domain it calculates circle of radius r in a Hough space. In the case of the initial image, it has to be done 6291456 times. In the case of a scaled down image it has to be done 16 times less. This leads to a substantial acceleration of approximation by the ellipse, which is very important at this stage. Besides, the size of the optic nerve disc is much larger than the details lost in the scaling operation. Also, as shown in the results section, quantitative parameters have a minor difference between that, achieved from a non-scaled image, and those achieved from the scaled down fundus image.

In further investigation, in order not to lose the optic nerve disc details, we will use the closed colour retinal image converted to gray-scale (see Section 2.2.3), since the OND edge describes all the three colour bands. This approach suffers from unwanted details seen in the $\{R\}$ and $\{B\}$ bands, which do not belong to the optic nerve disc. Thus, as a reference the closed $\{G\}$ band fundus image for the same patient's eye is also used which is least polluted with additional details.

After the pre-processing step has been completed, we have to localize the OND centre. The difficulty is that we even do not know a priori where the optic nerve disc lies in the retinal image. Thus, localization is performed in two steps, by applying the Canny edge detector and Hough transform to the edge-detected image.

3.2.1. Edge Detection

Canny has defined three criteria to derive the equation of an optimal filter for step edge detection: good detection, good localization, and clear response, i. e., only one response to the edge (Canny 1986). We have used a scheme of the Canny edge detector algorithm as follows.

The first step was to filter out any noise in the original image before trying to detect and locate any edges. Consider a two-dimensional Gaussian function:

$$G_{\sigma}(x, y) = \frac{1}{\sqrt{2\pi\sigma^2}} e^{\left(-\frac{x^2+y^2}{2\sigma^2}\right)}, \quad (3.1)$$

where $x = 1, \dots, N$, $y = 1, \dots, M$ and M, N are the dimensions of the discrete approximation matrix.

The main advantage of the Gaussian function is that we can easily approximate by a discrete convolution kernel. The discrete approximation can be calculated using:

$$h(x, y) = \frac{e^{-\left(\frac{x^2+y^2}{2\sigma^2}\right)}}{\sum_x \sum_y h_g}. \quad (3.2)$$

In our case, the standard deviation for noise suppression used $\sigma = 2$. This parameter was set experimentally.

Once a suitable mask has been calculated, the Gaussian smoothing is performed using the standard convolution methods.

3.2.2. Edge Gradient Detection

After smoothing the image and eliminating the noise, the next step is to find the edge strength by taking the gradient of the image.

Thus, for each pixel value at (x, y) in the smoothed retinal image I , was calculated:

$$\nabla I(x, y) = \left(I_x(x, y), I_y(x, y) \right)', \quad (3.3)$$

where $I_x(x, y)$ and $I_y(x, y)$ are image gradients along the x and y axis at a coordinate (x, y) , respectively. This task is resolved to calculation of edge strength and direction. Calculation of edge strength is performed by:

$$E_s(x, y) = \sqrt{I_x^2(x, y) + I_y^2(x, y)}. \quad (3.4)$$

Once the gradient has been found, the calculation of its direction comes to be possible:

$$E_o(x, y) = \tan^{-1} \left(\frac{I_x(x, y)}{I_y(x, y)} \right). \quad (3.5)$$

Further non-maximum suppression has to be applied. There are only four directions when describing the surrounding pixel degrees: 0° , 45° , 90° , and 135° . Thus, each pixel has to be grouped in one of these directions to which it is closest. Next we check whether each non-zero pixel at coordinate (x, y) in the image is greater than its two neighbours perpendicular to the gradient direction $E_o(x, y)$. If so, keep the pixel at (x, y) , or else set it to 0.

And the final phase of the Canny edge detector is to apply the hysteresis threshold. Before the hysteresis threshold can be applied the threshold levels have to be known. The problem is that the eye fundus images even of the same patient differs. Thus, the application of the static threshold level fails and false

detection of the optic nerve disc edges emerges. The dynamic threshold level calculation was introduced to Canny edge detector scheme and the calculation of the parameters is provided in section below.

3.2.3. Image Binarization

By thresholding the previous result at two different levels τ_1 and τ_2 , we obtain two binary images T_1 and T_2 . The difficulty is that we can not apply the static threshold level τ_1 since there are no retinal images with identical properties. For automated threshold level calculation we use Otsu's method (see Section 2.3.3).

We assume that to calculate the threshold level τ_1 , the black background around the retina is omitted. Also, after image pre-processing, a supplementary noise is observed. This leads to the appearance of unwanted details since, in origin, Otsu's method was designed for weak gradient change detection. After the threshold the edge detected images contain too many edge details. Thus, after a careful computation, the original parameter τ_1 is scaled to 25 % and the parameter τ_2 is calculated as follows: $\tau_2 = 0.1\tau_1$.

3.2.4. Hysteresis Threshold

After the parameters τ_1 and τ_2 have been calculated, we threshold the image at these two levels. For all unvisited pixels at coordinate (x, y) in the image T_2 we trace each segment in to its end and set them as contour points. At the segment end in the image T_2 we seek its neighbours in the image T_2 (since this image has much more details). If there are neighbouring pixels in the image T_2 , we denote them as contour points, too.

As described in the recombination of the results (see Section 2.2.4), to detect edges, we use intensity images from the closed band $\{G\}$, and the closed colour retinal image converted to gray-scale. This is necessary because there are cases where band $\{G\}$ does not provide any information about OND, and the bands $\{B\}$, $\{R\}$ are very noisy. In addition, using the closed gray-scale image with all bands, we retain all the nested information about OND.

The results of the edge detection scheme described are shown in Fig. 3.1 and Fig. 3.2. Here, in the right-side figures, the boundaries of OND are displayed 5 times magnified.

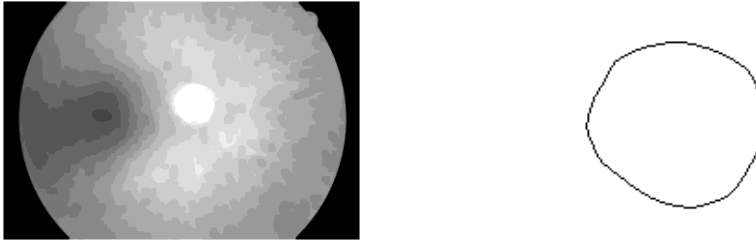


Fig. 3.1. The closed $\{G\}$ channel and edge detected images



Fig. 3.2. The closed intensity and edge detected images

The result of the Canny edge detection algorithm is an image with object boundaries identified. Suggested dynamic threshold level calculation allow us efficiently employ the properties of the Canny algorithm in automated edge extraction. However, the edges that describe the optic nerve disc may occur at every position in the image. Moreover, the boundary image contain not only the OND edges but also a supplementary edges described by excavation, fovea etc. Thus the next step is to apply the Hough transformation with the aim to identify the true position of optic nerve disc in eye fundus image.

3.2.5. Hough Transform

After the edge detection has been completed, we apply the Hough transform (Hough and Paul 1962) to the optic nerve disc localization. This is necessary because the optic disc structure in retinal images is nearly circular. We describe here the main idea. The general Hough transform can be found in (Ballard 1981).

The circular Hough transform is the method for transforming the image domain into the Hough domain. Each picture element in the image domain is transformed into a circle in the Hough domain.

Thus, in the case of a circle, this model has three parameters: two parameters indicate the centre of the circle and one parameter the radius. In this scheme the parameter space is congruent with the image space, that is, each

point in the image maps to a point in the same position in the parameter space (Ashbrook and Thacker 1998). To detect a circle of radius r , the circles of this radius are plotted in the Hough parameter space centred on every edge pixel found in the image. Thus, an array of peaks is formed for each edge-detected fundus image. A peak emerges when the circles in the Hough space intersect one another. Such peaks in the Hough parameter space indicate the possible centres of r radius circles.

The problem is that we do not know both: where the OND lies in the retinal image and how large it is. We iterate the circular Hough transform each time with the different circle radius r and select the highest peak value in the peak array formed (Fig. 3.3).

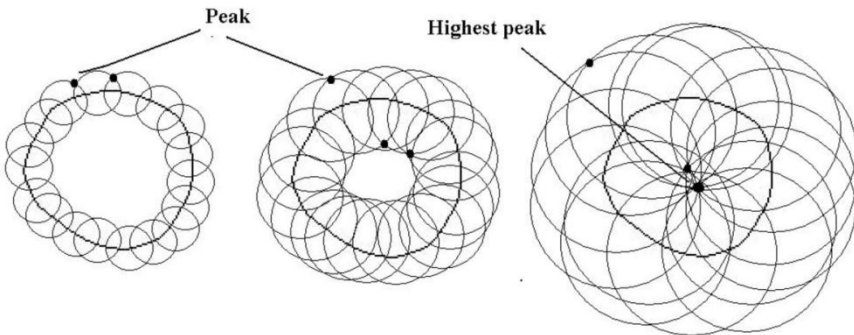


Fig. 3.3. The scheme of Hough transformation

Fig. 3.4 shows the optic nerve disc boundary after Canny edge detection and the resulting iterative Hough transform circle (dashed line).



Fig. 3.4. The result of iterative Hough transformation

After the parameters for the circle that match the true optic nerve disc boundary have been calculated, we assume that we have approximately found the OND in eye fundus image. Then the selection of the optic nerve disc boundary coordinates and the approximation of the elliptical cone is possible to accomplish.

3.3. Optic Nerve Disc Approximation by the Ellipse

After we have approximately calculated a radius of the circle and its centre coordinates, the next step is to choose the points describing the OND boundary. This is done by varying the circle radius on polar coordinates. The OND boundary can lie (as seen in Fig. 3.4) either within the circle found or outside it. In this case, we state that the binary image point (x, y) is selected as a boundary of the optic disc by iteration:

phi=0; dphi=0;

*Do While phi < 2 * pi*

Increase phi by dphi

*radius = r*0.9*

*Do While (radius < r * 1.1)*

*x = Hough centre x + (radius * Cos(phi))*

*y = Hough centre y + (radius * Sin(phi))*

If point(x,y)=TRUE Then

Add point(x,y) to boundary point accumulator

End If

Increase radius

Loop radius

Increase dphi

Loop phi

Here: *phi* is a direction; *dphi* is a direction angle step; *radius* is the current radius, *r* is the radius obtained by the iterative Hough transform.

In other words, we iterate the angle and the radius in polar coordinates, found by the iterative Hough transform, and check whether the image point (x, y) is set to 1. If so, we add it to the boundary point accumulator, or else move further to check another point (x, y) .

Here the radius *r* is restricted to the interval $[0.9r, 1.1r]$, whereas there are many cases where, after detecting the edge inside the area of OND, we see the edges of excavation. As usual, these edges (we assume them to be noise) are located near the OND boundary and can be defined as false ones. Also, the optic nerve disc boundary is not always round or ellipse-shaped after edge detection. Consequently, several fragments of boundary arcs can form a disc-shaped structure and other fragments, starting from the true OND boundary, can stretch along the retina as a line (Fig. 3.5). These lines are no more than noise left from vessel tree removal.



Fig. 3.5. OND boundaries with noise after edge detection

After the optic nerve disc boundary coordinates have been accumulated from binary images (as described before, from the closed intensity and the closed $\{G\}$ channel image), we apply the least squares ellipse fitting algorithm that calculates the ellipse parameters depending on the data set collected.

3.3.1. Least Squares Method

Since our objective is to parameterize the optic disc by an ellipse, we further introduce the least squares algorithm for fitting the ellipse. A full description of the algorithm can be found in (Fitzgibbon *et al.* 1999). Since this algorithm solves the best fit problem to the data set, it also controls the rotation of a cone and guarantee that the calculated parameters of an elliptic cone fit best to the given data set.

In general, the cone can be expressed as:

$$F(E_{param}, X) = E_{param} X = ax^2 + bxy + cy^2 + dx + ex + f = 0. \quad (3.6)$$

Where $E_{param} = [a, b, c, d, e, f]$ are the parameters of a cone and $X = [x^2, xy, y^2, x, y, 1]$ is a set of pixel coordinates from the boundary accumulator array. $F(X_i)$ is the so-called algebraic distance from the i -th point (x, y) to the cone $F(E_{param}, X) = 0$. So the fitting of the general cone can be approached by minimizing the sum of squared algebraic distances:

$$\theta_X(E_{param}) = \sum_{i=1}^N F(X_i)^2. \quad (3.7)$$

(Bookstein 1979) has shown that problem (3.7) can be solved as a problem of eigen-values:

$$D^T D E_{param} = \lambda C E_{param}. \quad (3.8)$$

Here D is the design matrix and $D = [x_1, x_2, \dots, x_n]^T$, C is the constraint matrix.

The appropriate constraint on the ellipse is well known, namely, that the discriminant $b^2 - 4ac$ has to be negative. However, this constrained problem is difficult to solve in general, since the Kuhn-Tucker (Rao 1984) conditions do not

guarantee the solution. Data scaling is performed by applying $E_{param}^T C E_{param} = 1$ quadratic constraint C of the form:

$$E_{param}^T \begin{bmatrix} 0 & 0 & 2 & 0 & 0 & 0 \\ 0 & -1 & 0 & 0 & 0 & 0 \\ 2 & 0 & 0 & 0 & 0 & 0 \\ 0 & 0 & 0 & 0 & 0 & 0 \\ 0 & 0 & 0 & 0 & 0 & 0 \\ 0 & 0 & 0 & 0 & 0 & 0 \end{bmatrix} E_{param} = 1, \quad (3.9)$$

which compels the constraint to become $4ac - b^2 = 1$. Thus, this reduces the ellipse fitting algorithm to minimizing:

$$E = \|D E_{param}\|^2, \quad (3.10)$$

with respect to the constraint $E_{param}^T C E_{param} = 1$.

Therefore, by differentiating the equation and assuming that λ is a Lagrange multiplier, we arrive at the system of equations:

$$S E_{param} = \lambda C E_{param}, \quad (3.11)$$

$$E_{param}^T C E_{param} = 1, \quad (3.12)$$

where S is the scatter matrix and $S = D^T D$.

The problem described is easily solved by eigen-vectors of (3.11). If (λ_i, u_i) solves (3.11), then it also does solve $(\lambda_i, c u_i)$ for any c , and from (3.12) we can find c_i that satisfies $c_i^2 u_i^T C u_i = 1$ by using:

$$c \sqrt{\frac{1}{u_i^T C u_i}} = \sqrt{\frac{1}{u_i^T S u_i}}. \quad (3.13)$$

Finally, by applying $\hat{E}_{param}_i = c_i u_i$, we solve (3.13).

Thus, by the (Fitzgibbon *et al.* 1999) scheme, the best parameters of the ellipse correspond to an eigen-vector identified by a minimal positive eigen-value.

3.4. Evaluation of Localization and Approximation Results

The testing set consisted of 54 retinal images. Within the scope of our investigation, only the retinal images of glaucomatous and healthy eyes were taken.

The results were evaluated by two criteria: optic nerve disc position in retinal image identification and approximation by ellipse accuracy. In the first case, in the OND localization there was only one false result which leads the proposed algorithm to the accuracy of 98.14 %. In the second case, in the optic nerve disc approximation by ellipse correctness measurements we excluded the case where the OND localization failed. Next, a comparative parameter space was constructed. In this step, the ophthalmologists from the BRKU set the points describing the optic nerve disc boundary by hand in the provided retinal images. These fundus images were not scaled down. Further, the least squares method described above was incorporated to produce the parametric form of each optic disc from all the 54 retinal images. Since the reference points were set by ophthalmologists, the defined elliptic parameters formed a reference parameter space for the proposed automated algorithm testing. As described in the least squares section, the rotation of ellipse is totally controlled by the algorithm. Besides, the reference points and that gathered by an automated algorithm were provided to the same least squares algorithm to get a parametric cone representation.

The comparative parameter space was formed of major and minor axes as well as horizontal and vertical diameters of the ellipse. The vertical and horizontal diameters of a cone were used here to indirectly show and evaluate the rotation of the ellipse. For the approximated examples shown in Fig. 3.6, Fig. 3.7 and Fig. 3.8 both data sets (ellipse parameters from the reference points and ellipse parameters from the proposed algorithm) is provided in Table 3.1.

Table 3.1. Some values from two data sets compared

Ellipse parameters from reference points				Ellipse parameters from proposed algorithm				Avg. error rate %
OND major axis	OND minor axis	OND horizontal diameter	OND vertical diameter	OND major axis	OND minor axis	OND horizontal diameter	OND vertical diameter	
2.54	2.44	2.44	2.54	2.56	2.46	2.54	2.49	1.89
2.18	2.09	2.09	2.18	2.17	2.08	2.14	2.08	1.96
2.27	2.15	2.19	2.22	2.28	2.16	2.19	2.19	0.52
2.28	2.16	2.18	2.25	2.22	2.11	2.11	2.21	2.44
2.22	2.06	2.08	2.20	2.29	2.07	2.23	2.12	3.54
2.43	2.29	2.31	2.41	2.45	2.43	2.42	2.42	3.02
2.59	2.56	2.53	2.51	2.49	2.42	2.47	2.40	4.02
2.30	1.97	1.98	2.19	2.34	1.95	2.19	1.98	5.80
2.45	2.43	2.42	2.42	2.50	2.29	2.21	2.21	6.19
2.41	2.02	2.04	2.39	2.40	2.21	2.40	2.21	8.64
2.22	2.15	2.20	2.18	1.70	1.57	1.57	1.73	24.8
2.25	2.14	2.21	2.18	1.51	1.35	1.50	1.34	35.2

We assume that the excellent approximation is when the average of parameters from two sets differ less than 3 %, a good approximation is when the average of parameters are between 3 % and 6 %, and a poor approximation is when the average of parameters is more than 6 %.

The overall average error rate achieved for the major axis of the ellipse was 4.97 %, for the minor axis – 6.06 %, for the horizontal diameter – 9.26 % and for the vertical diameter of the ellipse – 7.37 %.

Such a high error rate of the horizontal and vertical diameters of the ellipse is self-explanatory. Since the OND in retinal images has nearly a circular shape (the average difference in the provided data-set of minor and major axes is 0.2mm), thereof the ellipse rotation angle with respect to the positive Cartesian of the axis x is very neat. In other words, OND has more degrees of freedom to be rotated to vouch for the best fit problem.

As can be seen from Table 3.1, the last two lines the average error between parameters is more than 20 %. In all such cases in eye fundus images the optic nerve disc has a very weak edge gradient and can hardly be seen even by eye, as shown in Fig. 3.8, the last two images. Consequently, the made up OND boundary data set collected is very small. This is because we restrict the radius r when selecting boundary points in the section of optic nerve disc approximation by the ellipse and that leads to the fact that the least squares method fails to produce the right parametric form of the ellipse.

Some examples of the algorithm work are provided in Fig. 3.6, Fig. 3.7 and Fig. 3.8.

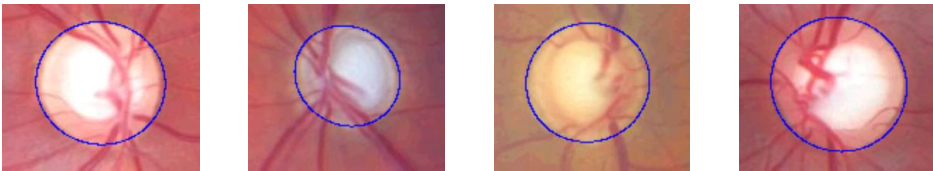


Fig. 3.6. Excellent approximation by the ellipse

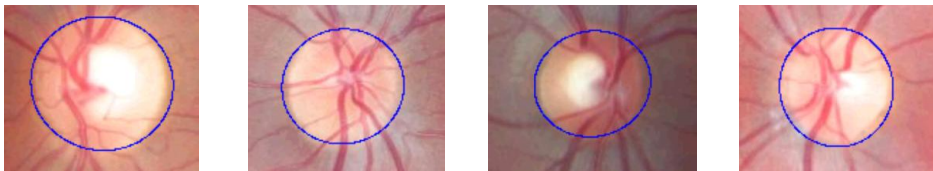


Fig. 3.7. Good approximation by the ellipse

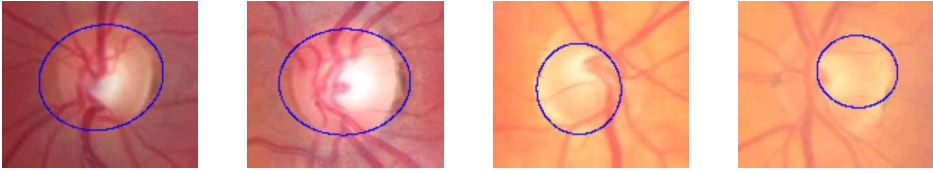


Fig. 3.8. Poor approximation by the ellipse

3.5. Conclusions for the Third Section

In this section, the problem of optic nerve disc localization and approximation by the elliptical cone is presented. The Canny edge detection algorithm was used to determine a boundary of the optic nerve disc. The introduction of non-static threshold level computation by Otsu's method extended this algorithm. The extension let automatically select levels for the hysteresis threshold depending on the intensity distribution of each eye fundus image. To localize the optic nerve disc, the iterative circular Hough transform was used that led the algorithm accuracy of the localization up to 98.14 % from 54 eye fundus images.

Finally, the least squares method was applied to calculate the ellipse parameters on the set of OND boundary points. The resulting ellipse parameters were compared and showed that the elliptic parameters, obtained by the proposed algorithm, on the average did not differ from those obtained by the reference points more than 9.26 %. The reference points have been taken from a non-scaled down image, which shows that the loss of information is minor in this context of problem.

4

Positioning of Overlapping Eye Fundus Images

In order to assess the diagnosis it is important to identify not only the structures seen in eye fundus image but also the tendency of structures change. The tendency may be evaluated from either from a parametric estimates of a structures or from the visual investigation of the eye fundus images. In order to facilitate visual identification of anatomical structures change emerges the necessity of the eye fundus image registration.

4.1. Survey of Methods for Eye Fundus Registration

In this section, we present an algorithm for automated retinal image registration (Treigys *et al.* 2008a). Image registration is the process of transforming the different sets of data into one coordinate system. In this particular situation, the registration should be performed so that the visible structures in two images overlapped each other in the resulting image (Fig. 4.1, right-hand side). The resulting image is described by a registration quality parameter. Besides, this section shows that, in order to solve the eye fundus registration problem, a linear transformation is sufficient.



Fig. 4.1. Base retinal image (*left-hand side*), committed for registration retinal image (*centre*), superimposed retinal images (*right-hand side*)

The eye fundus images were scaled to 768 times 512 of pixels. This leads to a substantial acceleration of vessel structure extraction. Further, the colour eye fundus image was converted to monochrome luminance as described in Section 2.3.1 and finally, the scheme for vasculature extraction, presented in Section 2.3, was applied.

For the registration problem the blood vessel tree of the eye fundus may be used. The main difficulty is to extract the vascular tree in a reliable way. The authors of the paper (Zana and Klein 1999) present an algorithm for temporal and multimodal registration of retinal images, based on the bifurcation point correspondences in a vascular tree. Further, an angle-based invariant probability is computed for every point match. Finally, the Bayesian Hough transform is used to sort the transformations with their respective likelihoods. Another approach was presented in the paper (Choe and Choen 2005). The authors propose a Y-feature extraction method, based on the local classification of image gradient information. An appropriate cost function is proposed for fitting the model, using a gradient-based approach. In the paper (Can *et al.* 2002; Stewart *et al.* 2003) authors use a model-based approach. The parameters of this model are estimated by matching vascular landmarks extracted by an algorithm that recursively traces the blood vessel structure. In another approach the iterative closest point algorithm is used. Another model-based approach is presented in (Tsai *et al.* 2003). The authors improved the approach by specifying a branching area and calculates the centre position of Y-feature. The centre position is estimated from the closest point of the three linearly approximated traces. Nevertheless, the algorithm proposed produces multiple Y-features in one branch. But the problem is that the majority of algorithms have been applied to the registration of fluorescent eye fundus images obtained after a fluorescent dye injection (Basevičius 2005), based on tracing or they are iterative and use local features of the eye fundus vasculature.

To avoid a false indication of Y-features, we propose to use the whole tree of the vasculature. Next, we have to get rid of supplementary information on the vasculature, i. e., the colour or width of blood vessels. Thus, the point of interest

is the topology of the blood vessel tree and that application of medial axis transformation.

4.2. Medial Axis Transformation

Let us assume that the above presented scheme is applied to two images: the base one and the investigative one. The next step is to extract the topology of vasculature from both images: from the base image and the image to be registered. For this end we have used the medial axis transform (skeletonization) (Mukherjee *et al.* 2002). Basically, the skeletonization operation is calculated by shifting the origin of the structuring element (Fig. 4.2) to each possible pixel position in the image. Then, at each position it is compared with the underlying image pixels. If the foreground and background pixels in the structuring element match exactly the foreground and background pixels in the image, then the image pixel situated under the origin of the structuring element is set to the background, otherwise, it is left unchanged. Here we denote that a foreground pixel is assumed to be 1 and a background pixel is 0. An empty cell means that a particular pixel is of no interest, and it is not taken into account for evaluation.

0	0	0
	1	
1	1	1

	0	0
1	1	0
	1	

Fig. 4.2. Structuring elements used for skeletonization

In Fig. 4.2, images are first skeletonised by the left-hand structuring element, and afterwards by the right-hand one. Then the above presented process is performed with the remaining six 90° rotations of those two elements during the same iteration. The iteration process is stopped when there are no changes in the image for the last two iterations, i. e., the resulting image contains only the topology of the blood vessels.

4.3. Transformation to the Frequency Domain

In order to register two vasculature trees achieved by medial axis transformation we have to incorporate some cross-correlation method. It is well known that for big images the convolution methods designed for cross-correlation runs very slowly. This problem can be solved by introducing a discrete Fourier transform (DFT) (Karmen and Heck 2002). Usually DFT is defined for the discrete

function $f(x, y)$ that is non-zero over the finite region $0 \leq x \leq M - 1$ and $0 \leq y \leq N - 1$. In our case, this function represents a retinal image in the spatial domain. Then, the two-dimensional discrete Fourier transformation of the matrix M by N can be calculated as follows:

$$F(p, q) = \sum_{x=0}^{M-1} \sum_{y=0}^{N-1} f(x, y) e^{-i\left(\frac{2\pi}{M}\right)px} e^{-i\left(\frac{2\pi}{N}\right)qy}, \quad (4.1)$$

where $p = 0, \dots, M - 1$ and $q = 0, \dots, N - 1$. The inverse DFT can be achieved by applying:

$$F_I(x, y) = \frac{1}{MN} \sum_{p=0}^{M-1} \sum_{q=0}^{N-1} F(p, q) e^{i\left(\frac{2\pi}{M}\right)px} e^{i\left(\frac{2\pi}{N}\right)qy}. \quad (4.2)$$

Here $x = 0, \dots, M - 1$ and $y = 0, \dots, N - 1$.

The Fourier transform produces a complex number valued output image. This image can be displayed with two images, either with the real and imaginary part or with magnitude and phase.

In our investigation, we apply (4.1) to the base retinal image. The retinal image committed for the registration process is rotated by 180° , since the convolution operation itself reverses the provided pattern (Smith 1997). Then, the (4.1) is applied to the rotated pattern as well. This results in four arrays, the real and imaginary parts of the two images being convolved. Multiplying the real and imaginary parts of the base image by the real and imaginary parts of the image committed for registration generates a new frequency image with the real and imaginary parts. Taking an inverse DFT of the newly created frequency image, described by (4.2), completes the algorithm by producing the final convolved image. The value of each pixel in a convolved correlation image is a measure of how well the target image matches the searched image at a particular point. The new correlation image calculated is composed of noise plus a single high peak, indicating the best match of vasculature of the image to be registered in the base retinal image vasculature. Simply by locating the highest peak in this image, it would specify the detected coordinates of the best match.

The frequency transformation procedure described above is applied by taking the structure of vasculature of the image which has to be registered on itself. This is done because other coordinates are necessary that shows where the best match of image on itself is (Fig. 4.3).

In Fig. 4.3 on both sides a smaller peak corresponds to the two different images convolved together. The biggest peak corresponds to the image convolved by itself. Then, by introducing a simple linear transform to the retinal image, committed for registration, we shift pixels by the calculated distance along the x and y axes. The result of shift calculation is shown in Fig. 4.4.

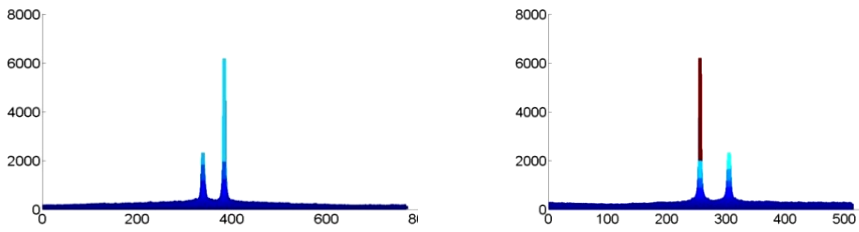


Fig. 4.3. Match point after cross-correlation in frequency domain

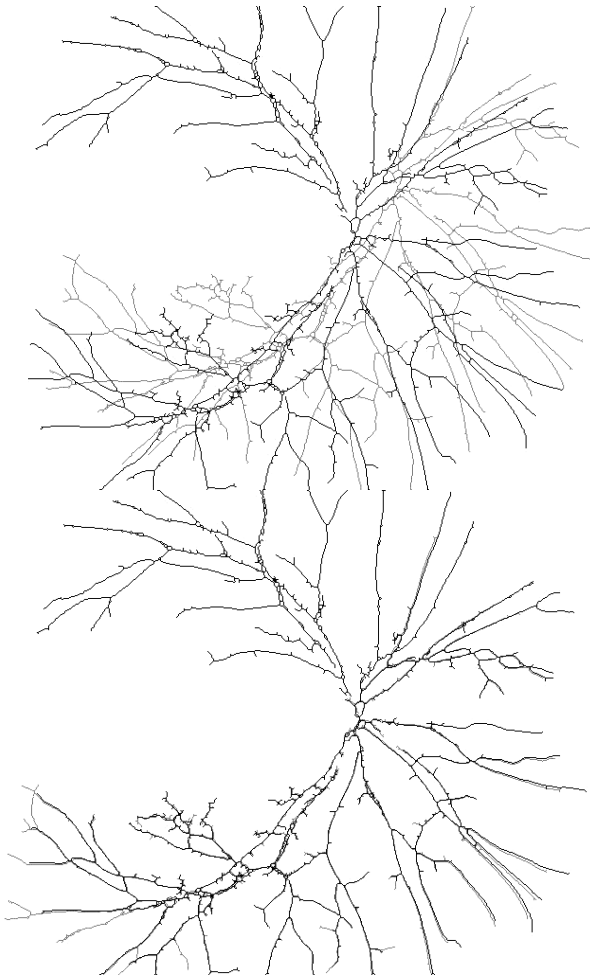


Fig. 4.4. Superimposed structures of the extracted vasculature

Fig. 4.4 shows two structures of vasculature extracted by the method proposed above. The stronger structure belongs to the base retinal image on which a retinal image intended for registration has to be put. The weaker structure of vasculature belongs to the retinal image intended for registration. The top image represent two superimposed topologies of the vasculature. The bottom image represent the registered topologies of the vasculature.

4.4. Evaluation of Positioning Results

The testing set consisted of 19 patients' eye fundus images of both, left and right eyes. A great number of each patient's eye fundus images were taken. Thus, in testing the algorithm, we have analysed 55 retinal images of the left eye and 56 retinal images of the right eye in all. It should be noted that registration of images is possible only if those images are of the same patient and of the same eye. This comes from the fact that the structure of eyes vasculature of each human is unique. In order to verify this fact and to obtain the factor of registration error, the registration algorithm described above was applied to the retinal images taken from different patients of the same eye (Fig. 4.5).

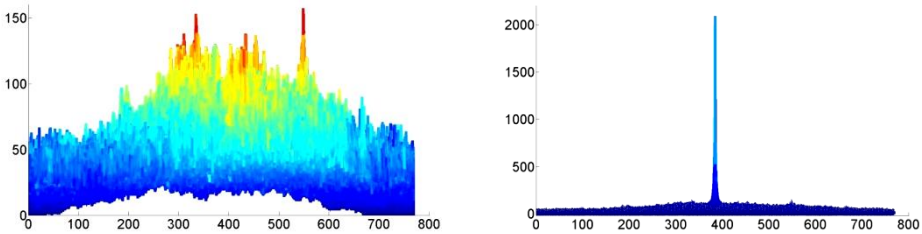


Fig. 4.5. The correlation between two different images (*left-hand side*), self-correlation of retinal images (*the right-hand side*)

Fig. 4.5 shows the magnitudes of convolved images along the x axis. In this particular case, where it is not the same person is taken for investigation, note, that magnitudes on the left image are dramatically lower than that in the image on the right.

Thus, to evaluate the quality of the registration, we computed the ratio of the peak-signal to noise (PSNR). 119 possible pairs of eye fundus images have been investigated. The conditions for those images to be of the same person and also of the same eye have been satisfied. The results achieved are shown in Fig. 4.6.

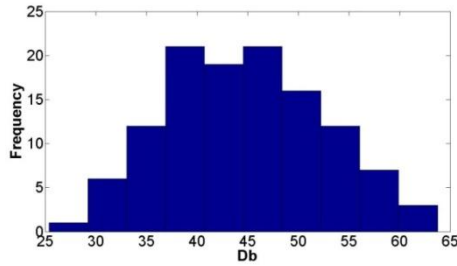


Fig. 4.6. Histogram of the peak signal to noise ratio

In Fig. 4.6, a histogram of the ratio peak-signal to noise is presented. According to (Netravali and Haskell 1995), acceptable PSNR values are between 20 and 40 decibels. The higher the value of decibels, the better registration is performed. Fig. 4.7 shows the registration result of the quality f 51 decibels.

Here we can draw the conclusion on automated human identification from retinal images. If the ratio peak-signal to noise dramatically lower than 25 decibels one can made the decision that it is not the same person. In case shown in Fig. 4.5 calculated PSNR value was 4.3 decibels. Beside, the comparative PSNR analysis can be made over the patients' database in order to automatically identify the person taking the physician consultation. This can be used for solving the problem of patient's data protection because physician will be working only with the data about the state of the patient without knowing who really the patient is.

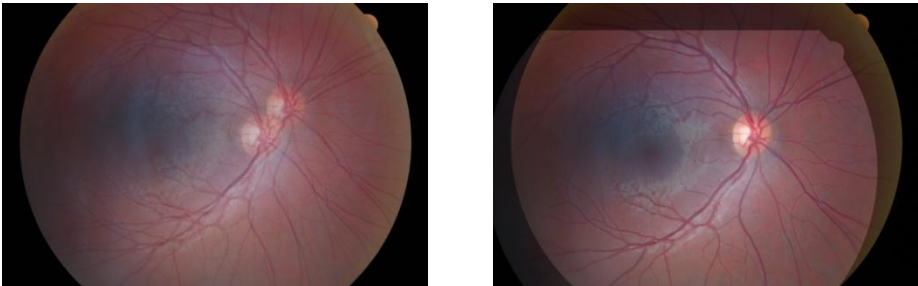


Fig. 4.7. Two superimposed (*left-hand side*), registered retinal images (*right-hand side*)

4.5. Conclusions for the Fourth Section

In this section an automated technique for retinal image registration is presented. The goal of the problem was to register two retinal images so that optic nerve

discs in the resulting image overlaps each other in the best way. The task was accomplished by introducing the intensity level mathematical morphology operations for vessel extraction. Then the intensity adjustment procedure was performed to enhance the resulting image after subtraction. This operation was followed by the image binarization, where the skeletonization operation was introduced. In the next step the spatial domain of the extracted vasculature structure was converted into the frequency domain, which resulted in a fast convolution of two images. This fact enables us to calculate the image shift along the Cartesian axes. The analysis of provided retinal images showed that the registration quality parameter basically occurs within the bounds of decibels accepted in literature. By introducing the global topology of the blood vessel tree, we have showed that for OND registration problem a linear transformation is enough to obtain satisfactory results.

Disclosed problem on human identification revealed that proposed algorithm is also suitable to solve the identification-related class problems. However, more careful analysis in order to evaluate the identification results should be made.

5

Data Analysis: Software Tools and Applications

In the first part of this section we will present the software for the automated optic nerve disc approximation by the ellipse. Next, a comparative analysis of the parameters gathered in an automated way and the parameters of the ellipse defined interactively by physicians will be discussed. In the third part of this section, the neural network will be explored as a disease classifier. In our investigation, the sets of parameters describing glaucomatous and healthy eyes are taken. These sets represent the structure of the optic nerve disc which resides in a patient's eye fundus image. As a separate case, the excavation can be seen in the image as well. These two sets describe the elliptical shape of both structures and comprise the initial data for the neural network. Finally, in the fourth part of the section thermovisual data will be investigated with a view to detect thermal anisotropy of the tissue.

5.1. Software Implementation

Despite the promising results provided in Section 3.4 which were achieved on the initial data set of 54 images, it is necessary to explore the collected OND

parameters in a manual and automated way. To this end, a software has been developed. This software was aimed to collect experts' experimental data and compare with automated algorithm described in Section 3. In this case, experts mark the points of the optic nerve disc boundary by hand. Later on, least squares elliptical fitting is performed at these points. Further, the analysis of these parameter sets can be accomplished. The basic functionality of the program is provided in the use case diagram (Fig. 5.1).

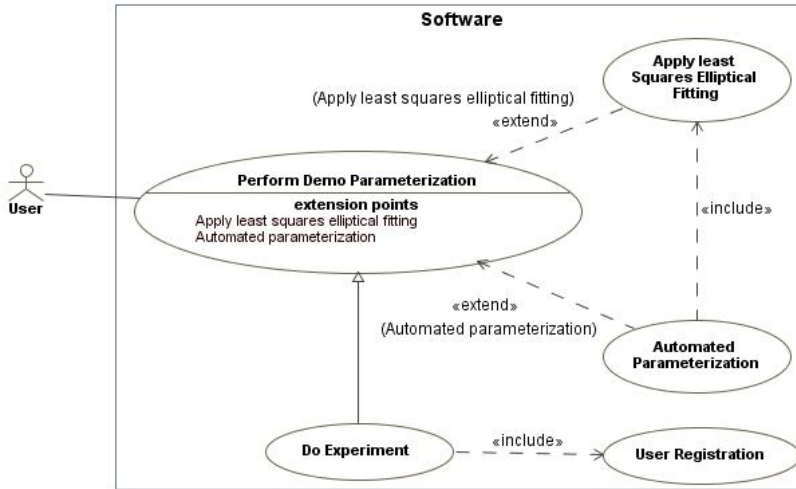


Fig. 5.1. High-level software use cases

The basic activity (see Fig. 5.2) of user interaction with the software can be described as follows:

When the user starts the software, the main window is shown. Then the user can decide either to practice with the software by the “Demo” mode, either to do an experiment by selecting “Do experiment”. In both cases, the basic scenario steps are the same except that, in the “Demo” mode, the user does not have to perform the registration procedure and the results of the manual or automated point selection are not saved in the database. On the shown eye fundus image, the user:

1. Points the centre of the optic nerve disc.
2. Invokes the “Draw axes” function by clicking the appropriate button. This results in drawing lines on the image that cross in the marked optic nerve disc centre and divide the OND region into twelve equal parts. These two steps were predefined by the problem domain users.

3. If the result satisfies the user's expectations, the user proceeds with the fourth scenario step, or else he can repeat the first two.
4. Selects twelve points along each axis that points to the boundary of the optic nerve disc. The user can move the selected point to precise location, if he wants.
5. Finally, the coordinates of points are committed to the database.
6. Further, depending on the user needs, OND boundary marking points can be automatically approximated by the ellipsis in the least squares sense.
7. Besides, automated localization of the ellipsis can be accomplished as well, on the active eye fundus image, or on an arbitrarily selected one.

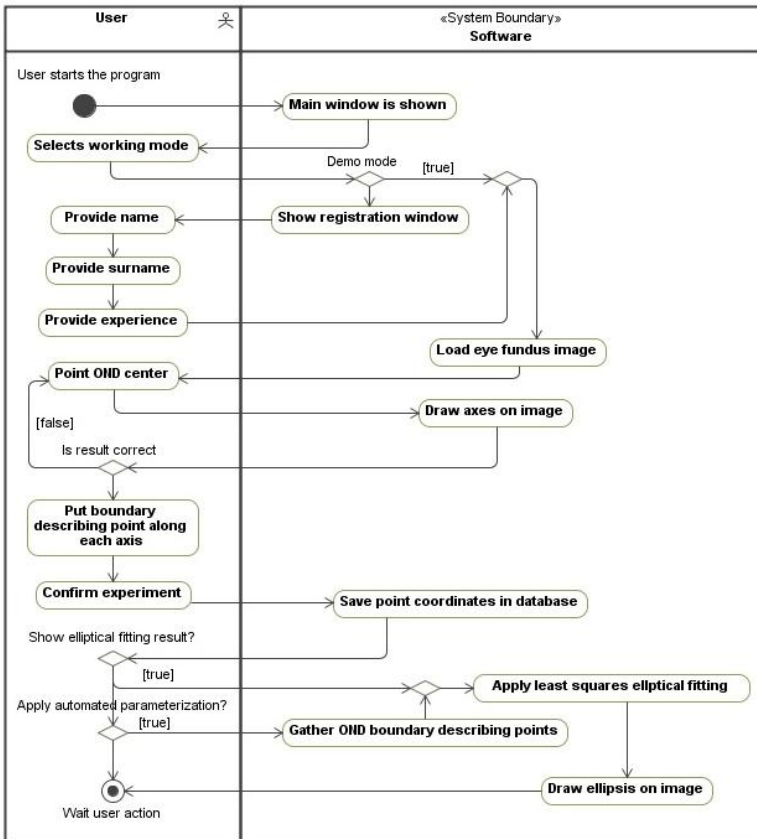


Fig. 5.2. Basic scheme of user's interaction with the software

An example of the approximation result is provided in Fig. 5.3. Further, in order to compare the results, the same ellipsis approximation algorithm will be applied to manually selected and automatically gathered (algorithm is provided in Section 3) sets of points that describe the OND boundary.

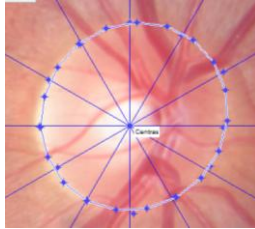


Fig. 5.3. Example of the elliptical approximation

In the case of experiment, this scheme has to be repeated on each image provided by the software except the registration procedure. When the user finishes the processing of the image, the next image is shown on the screen. Overall there are six images selected by ophthalmologists as the basic reference. The experiment for one user has to be carried out in a series. If the experiment falls into an exception, it has to be repeated from the very beginning. The software implements the algorithms described in Sections 2.2 and 3.

In addition, the client software for automated eye fundus images accumulation and processing was developed (Fig. 5.4). The software relied on the client-server technology. All the images as well as the image approximation data are saved on the server. At present the registered user has access to two groups of provided functionality, i. e., Patients and Administration.

- The user in the Patients group can:
 - Register a new patient.
 - Edit the registered patient.
 - Delete the data of the registered patient.
 - Upload eye fundus images for the patient.
 - Process uploaded eye fundus images.
 - Select the corresponding diagnosis on the uploaded eye fundus image.
- The user in the Administration group can:
 - Create, edit, delete, and manage user rights.

- Edit server connection data.
- Create, edit, and delete the diagnosis.

By selecting an investigative image from the list on the left and right-clicking on the shown eye fundus image, the user is able to process image for OND localization and parameterization. Finally, after processing by double-clicking on the resulting image, the image with the approximation result is shown (Fig. 5.5).

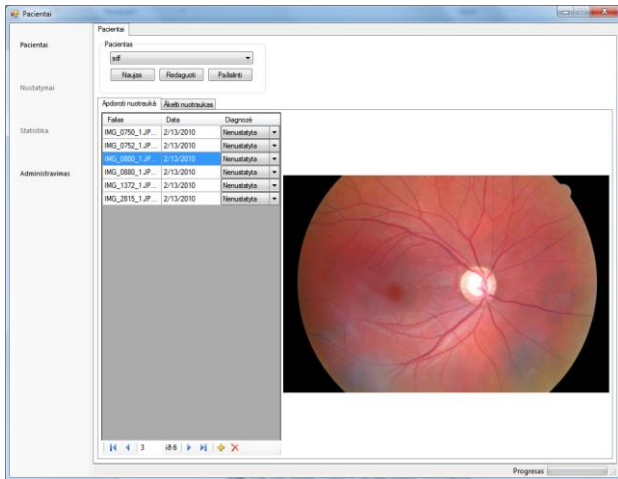


Fig. 5.4. The main window of the software

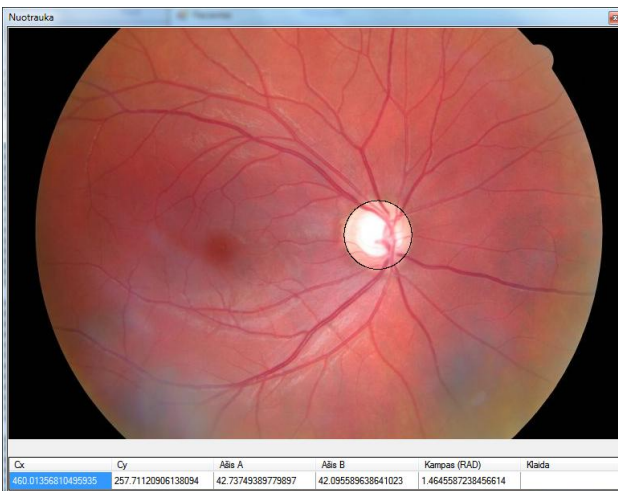


Fig. 5.5. Processed eye fundus image

The processed data are saved in the database and are related to the user and the patient, moreover, the software allows each user to see only his/her own data. This scheme allows us to accumulate the independent experimental results that further can be analysed.

5.2. Analysis of the Optic Nerve Disc Parameters

The results of this sub-section rely on the report of the investigation which was accomplished in (Paunksnis 2009). An algorithm which automatically detects the location and calculates the ellipsis parameters the optic nerve disc is described in Section 3, besides, its implementation is briefly described in the Section 5.1. Thus, naturally there arises a question, whether software implementation produces an elliptical cone which is similar to that defined by the ophthalmologist defined elliptical cone. In other words, if we have a set of eye fundus images and a set of different elliptical cones defined by ophthalmologists in each of the image, is it possible to distinguish an elliptical cone produced by the software from that defined by physicians.

All the optic nerve disc contours are parameterized according to the same methodology as it is done in diagnostic purposes. Each optic nerve disc is parameterized by the elliptical cone. The ellipsis parameters taken for the further investigation are:

- Horizontal coordinate of the ellipsis centre C_x .
- Vertical coordinate of the ellipsis centre C_y .
- Longer semi-axis of the ellipsis R_x .
- Shorter semi-axis of the ellipsis R_y .
- Ellipsis rotation E_{Angle} .
- Restricted area of the ellipsis E_{Area} .

6 eye fundus images were taken under investigation. The contours of the optic nerve disc estimated fifteen different physicians. The data related to each image are provided in Annex A from Table A1 to Table A6. In each table, the first column rows numbered from 1 to 15 represent physicians' data. However, in Table A6, provided in Annex A, the results of the fifth and the fifteenth physician have not been saved. The row with the parameter "Software" represents data gathered during the automated approximation of ellipsis. Besides, additional parameters are provided for each parameter such as average,

minimum, and maximum values as well as the results of investigation. Next, the successive parameters after the parameter “Software” meanings are:

- *Sigma from average value*; describes the difference (in squared deviation σ sense) from the automatically estimated value and a physician's average value of a particular parameter.
- *Overfits physician boundary*; value is set to one if the value estimated in an automated way is higher than the physician's value interval.
- *Overfits physician average*; if the value is 1 it means that the value estimated in an automated way is higher than the average of the physicians' values.
- *4th physician sigma from average*; value describes the difference of the fourth physician's value (in the squared deviation sense) from that of the parameter average evaluated by other physicians
- Successive data under the row called *Excluding 4th physician* represent analogous data meaning as above with excluded values of the fourth physician.

It should be remembered that in the case of normal distribution, the values drifted from the average by 1.96 sigma, statistically not belong to the distribution with 5 % importance interval. In practice, the difference of two sigma is applied to unknown distributions, when we have to identify outlier points.

Fig. 5.6 shows the evaluated area of OND according to each ophthalmologist. This figure represents the area of the same optic nerve disc while Fig. 5.7 visualizes the distribution of the ellipsis area in each image for each physician.

According to Fig. 5.6 and Fig. 5.7 different physicians provide different values. As an example for an important parameter Area (see Annex A Table A1 and Table A4) maximum values are 1.5 times higher than minimum values. Moreover, according to Table 5.1 and Fig. 5.7 the values estimated by the fourth physician are higher than the values estimated by the rest doctors. This physician tends describe OND larger than others. This fact can also be seen from the parameter line *4th physician sigma from average*. In three cases the values of R_x , R_y , and E_{Area} differ from the other physicians' parameter average more than by two sigma. Thus, the data from this ophthalmologist can be treated as a systemic error or outlier and can be excluded from further investigation. Despite this fact, Fig. 5.7 shows that the values provided by the rest physicians incidentally scattered. Thus, this results in a need of measurement unification or standardization.

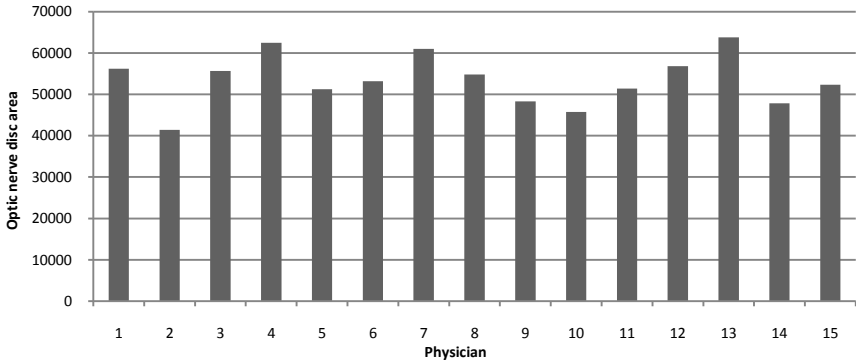


Fig. 5.6. Measurement area scattering

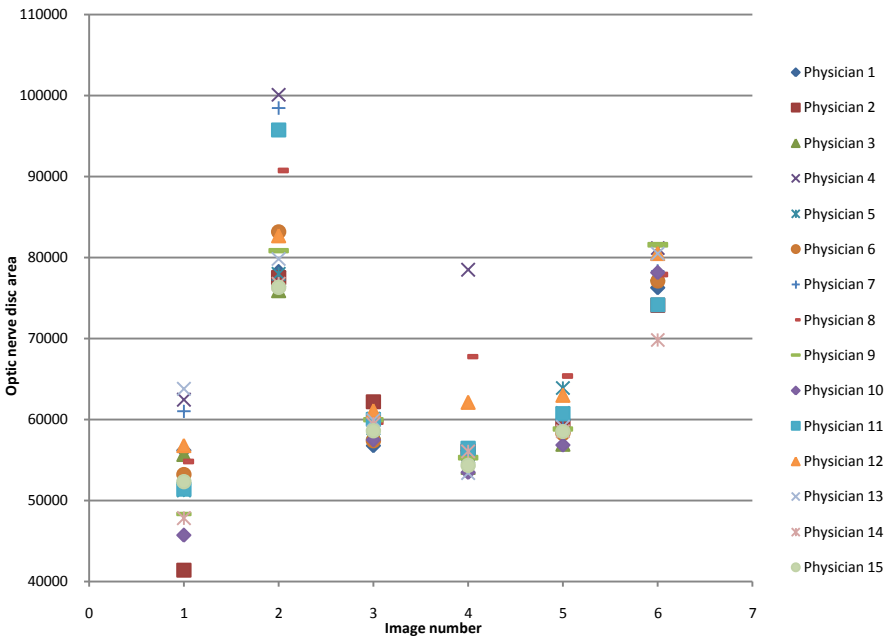


Fig. 5.7. OND area measurement according to ophthalmologists' settings

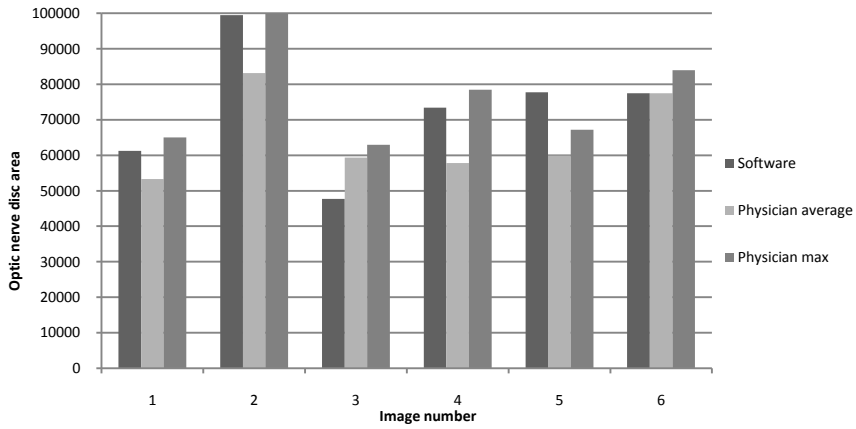


Fig. 5.8. Automatically obtained OND area values in comparison with the values of physicians

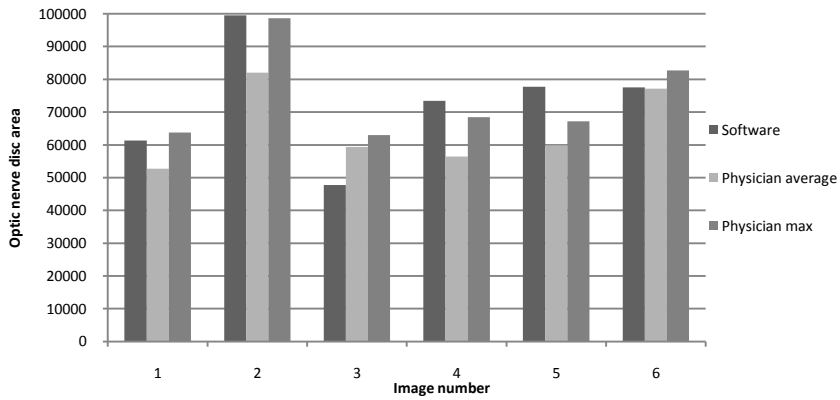


Fig. 5.9. Automatically obtained OND area values in comparison with the values of physicians, except for 4th doctor

Table 5.1. Count of the value maximum among measurements

Physician	1	2	3	4	5	6	7	8	9	10	11	12	13	14	15
Count of maxima		2	1	7	4		3	2	2	1		1	4	3	
Count of maxima between R_x and R_y		1		6	1			1	1				1	1	

As can be seen from Fig. 5.8 and data provided in tables from Table A1 to Table A6 in Annex A, the proposed algorithm tends to increase the OND. In five of the six cases, an automatically calculated OND area is larger than that measured by all physicians. In one case, the automatically selected OND area is larger than the maximum calculated by all doctors, other 4 cases are very close to the maximum. In three images from six, the automatically calculated OND area is statistically significantly different from all the doctors' data and machine results are quite similar to the OND boundary marked by the 4th physician.

Rejection of the 4th physician's data, yields a greater difference between the software results and that of physicians. As can be seen from Fig. 5.9, in four cases out of six the automatically obtained OND area is larger than the maximum area according to physicians' measurements. In five images, the automatically obtained OND size is significantly different from the 14 physician's data: in four cases it is significantly higher, in one case – significantly lower.

5.2.1. Artificial Neural Network as a Disease Classifier

The aim of the investigation of this sub-section is to check whether the artificial neural network can be used as a healthy-glaucoma disease classifier from the parameters of eye fundus image.

Assume that some set of parameters characterizes the optic nerve disc and excavation (Treigys and Šaltenis 2007). Hence, it becomes possible to construct an n -dimensional vector $Y = (y_1, y_2, \dots, y_n)$. Each n -dimensional vector corresponds to one fundus image and describes the disease.

The goal is to attribute the vector Y_i to one of the known classes, where $i = 1, \dots, m$ and m is the number of patients.

The set of 27 parameters of each eye fundus image has been measured. Generally, these parameters fall into four groups (Bernatavičienė *et al.* 2007):

- Parameters of optic nerve discs:
 - Length of major and minor axes of OND ellipse.
 - Length of semi-major and semi-minor axes of OND ellipse.
 - Horizontal and vertical diameter of OND ellipse.
 - Area, perimeter, and eccentricity of OND ellipse.
- Parameters of excavation (EKS):
 - Length of major and minor axes of EKS ellipse.
 - Length of semi-major and semi-minor axes of EKS ellipse.

- Horizontal and vertical diameter of EKS ellipse.
- Area, perimeter, and eccentricity of EKS ellipse.
- Ratios between various OND, EKS, neuroretinal rim (NR) parameters. Neuroretinal rim is a tissue between EKS and OND:
 - Ratios between EKS and OND horizontal and vertical diameters.
 - NR area.
 - Ratio between NR and OND areas.
 - Ratio of EKS and OND.
- Thickness of NR parts:
 - Inferior, superior, nasal, and temporal disc sectors.

Two groups of items are investigated: vectors, corresponding to the healthy eyes (24 items); vectors, corresponding to the eyes, damaged by glaucoma (24 items). Unknown EKS parameters were assumed to be zeros. This happens when the excavation is absent or not measured in the eye fundus image.

In mathematical terms, we can state that for the input vector Y (set of values representing the problem domain) and the weight vector W (set of weights describing how important each problem domain value is) the weighted sum of the neuron can be found by:

$$s = w_0 + \sum_{i=1}^n y_i w_i, \quad (5.1)$$

where n is the dimension of the input vector Y , w_0 is the bias and w_i is the i th weight. Further, the activation function $f(s)$ of the form:

$$f(s) = \frac{1}{1+e^{-s}}. \quad (5.2)$$

was used.

The main disadvantage of the single-layer artificial neural network is that it can easily operate and show itself fine until the classes described by the vectors Y are separable. But, as the dimensionality n of the vector Y increases, in most cases it forms not linearly separable regions. As stated before, with no hidden layer, the neuron can only perform linearly separable tasks. Let us consider the network shown in Fig. 5.10. Here x , y are values representing a point on the plane. The output can be calculated as follows:

$$\begin{cases} 1, & f(s) > 0.5, \\ 0, & f(s) \leq 0.5. \end{cases} \quad (5.3)$$

(5.3) describes two regions on the plane xy . Actually it exposes the region to which the given point corresponds.

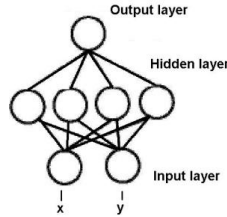


Fig. 5.10. Artificial neural network with one hidden layer

Let us assume that the same point (x, y) is introduced into the network (Fig. 5.10). Since there are four neurons in the hidden layer and they are independent of each other, the given point is classified into four pairs of linearly separable regions. Each region is described by a unique line produced by each neuron in the hidden layer. Finally, the output layer performs some logical operation on the outputs of the hidden layer, so that the network ascribes the input point either to one region or another that might not be linearly separable (Fig. 5.11).

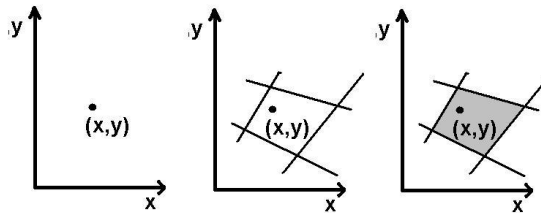


Fig. 5.11. Initial point (*left-hand side*); region formed by hidden layer (*centre image*); output layer response (*right-hand side*)

Thus, by varying the number of neurons in the hidden layer, the number of hidden layers, and output nodes, we can attribute the number of points of arbitrary dimensions into the required number of groups.

The artificial neural network with one hidden layer with the log-sigmoid activation function and second order Levenberg-Marquardt (Marquardt 1963) learning algorithm was used. This learning algorithm is more robust and in many cases finds a solution even if it starts very far off the minimum (Abraham and Nath 2001).

For the artificial neural network training, the set of 48 vectors was divided into two separable subsets of 24 vectors. One subset was used for the artificial

neural network training and the other – for the cross testing procedure. Cross testing is performed to prevent the artificial neural network from overtraining (Saarinen *et al.* 1993).

The class to which each vector belongs is known in advance. The proposed classifier has to be able to tell apart glaucomatous from healthy eyes by the given parameters, corresponding to one investigative eye fundus image. The artificial neural network with one hidden layer was used for investigation.

At first, the optimal number of hidden neurons in the hidden layer was not known. In this case, to find the optimal number of units, an iterative procedure was used. The parameter vector consisted of 27 measured features of the optic nerve disc structure. Thus, in the first iteration, only one hidden unit was used. In the second iteration, two hidden units were investigated, in the third iteration, three hidden units were used, etc, up to 27 hidden units. Each iteration was repeated 100 times because of initially selected random weights for artificial neural network units. During the evaluation of network error, all the 48 parameter vectors were provided for the network classification task. The network error was measured in the sense of the sum of squared errors (SSE). The diagram of the best SSE drawn for a particular number of units in a hidden layer is shown in Fig. 5.12.

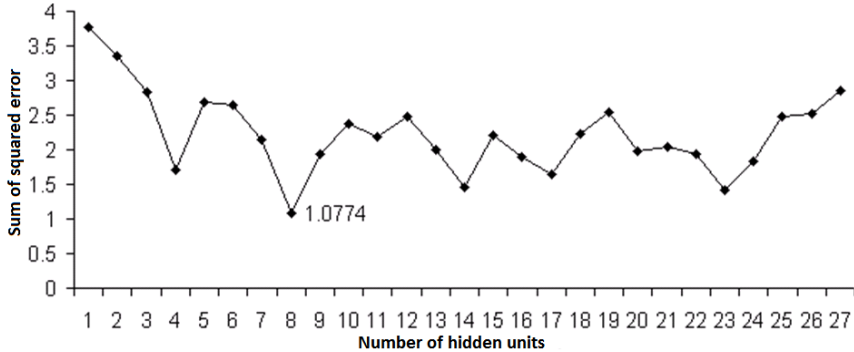


Fig. 5.12. Sum of squared error according to the number of hidden units

Fig. 5.12 shows that the optimal number of hidden units is 8 for this problem statement in the SSE sense.

Second, the network was tested as a disease classifier. The results achieved are provided in Table 5.2. We can see from the table that the minimum of SSE is when the number of hidden units is 8. All the healthy eyes were identified correctly and only one case of glaucomatous eyes was classified as healthy.

However, the result shown in Fig. 5.12 is questionable, since the curve has a lot of peaks. To explain such curvature, the standard deviation of network error

was explored. As stated earlier in this sub-section, the initial weights are selected randomly. Thus, it becomes possible to measure what influence those starting values have on the sum of squared error. In the case of 8 hidden units, where the SSE was minimal, the standard deviation was 3.25.

Table 5.2. Classification results with respect to number of hidden units on non-scaled data

Number of hidden units	True glaucoma	False glaucoma	False norm	True norm	SSE
1	20	4	1	23	3.775
2	21	3	3	12	3.362
3	22	2	4	20	2.823
4	21	3	1	23	1.706
5	22	2	2	22	2.698
6	22	2	2	22	2.642
7	23	1	0	24	2.141
8	23	1	0	24	1.077
9	22	2	0	24	1.935
10	22	2	2	22	2.371
11	22	2	1	23	2.194
12	20	4	0	24	2.488
13	22	2	0	24	2.005
14	23	1	1	23	1.464
15	23	1	3	21	2.209
16	22	2	0	24	1.890
17	22	2	0	24	1.637
18	20	4	1	23	2.230
19	21	3	1	23	2.536
20	23	1	1	23	1.971
21	22	2	0	24	2.048
22	22	2	1	23	1.933
23	22	2	0	24	1.426
24	22	2	2	22	1.829
25	21	3	4	20	2.481
26	23	1	4	20	2.528
27	22	2	3	21	2.862

In addition, the influence of derivative parameters was investigated. In this case, the principal component analysis (PCA) was made as the initial step for pre-processing data vectors, which retain only those components that contribute

more than 1 % to the variance in the given data set (Medvedev 2007). Such an analysis has showed that in the case of the given variance it is enough to take 10 parameters in each feature vector. Further, the artificial neural network was trained under the same conditions with the pre-processed data set. The graphical result of sum of squared errors is shown in Fig. 5.13.

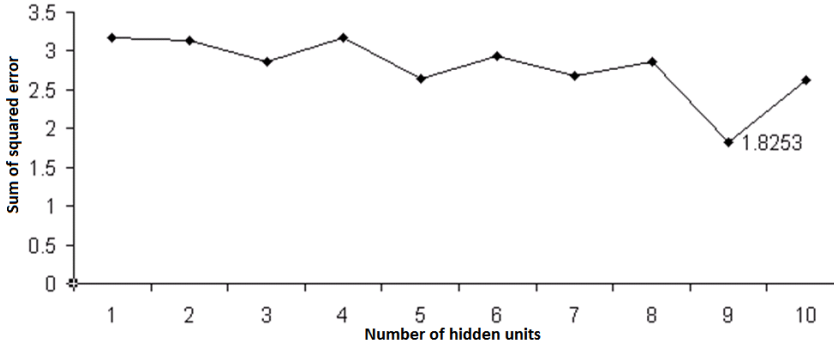


Fig. 5.13. Sum of squared error according to the number of hidden units with pre-processed data set

One can see that contrary to Fig. 5.12, the network SSE response variance is smoother. However, the overall error is greater than that with not pre-processed data. The classification results are presented in Table 5.3.

Table 5.3. Classification results with respect to number of hidden units on scaled data

Number of hidden units	True glaucoma	False glaucoma	False norm	True norm	SSE
1	22	0	5	19	3.175
2	22	2	3	21	3.129
3	22	2	3	21	2.867
4	17	7	1	23	3.170
5	21	3	2	22	2.642
6	24	0	3	21	2.936
7	22	2	1	23	2.856
8	22	2	1	23	2.856
9	24	0	1	23	1.825
10	22	2	1	23	2.621

In the case of data pre-processed by the PCA algorithm, the minimal sum of squared errors was obtained with nine hidden units. The best classification error achieved was 1.825 with the standard deviation of 2.13.

In both cases, no matter that the initial data were pre-processed or not, only one feature vector was erroneously classified. The classification accuracy of 97.91 % were achieved of the investigated artificial neural network. The previous results presented in (Paunksnis 2006) on the same data set were:

- Naïve Bayes – 83 %;
- Decision Trees – 83 %;
- k Nearest Neighbour – 83 %;
- Support Vector Machine – 77 %;

By setting the unknown excavation parameters to zeros, we could increase the accuracy of classification performance by 14.91 % compared to the results presented in the report (Paunksnis 2006). However, the deviation of the classification errors implies that the classification result is questionable in both cases.

5.3. Analysis of Thermovisual Data

Thermography is a contact-free method used in experiments and cardiovascular surgery to investigate the myocardium and coronary artery function. When performing a coronary bypass without artificial blood circulation, it is important to be aware of how a cut off in blood flow affects the myocardium and restoration of coronary blood flow after surgery. Diagnosis and treatment of the ischemic disease are the most important problems in cardiology. In many cases a sudden death is caused by myocardial ischemia and is accompanied by ventricular arrhythmias. It has been proved that ischemic slowdown of excitation spread provokes the formation of recurrence of arrhythmia, ventricular tachycardia and ventricular fibrillation (Lekas *et al.* 2009). During coronary artery bypass grafting operations a surgeon requires information regarding coronary flow, coronary anatomy and myocardial perfusion. Additional quantitative flow estimation is desirable to detect graft failures as early as possible. Thermography imaging, such as advanced, uncooled microbolometer detector technology, delivers high-resolution long-wave infrared images that allow to determine thermal variances. Real-time scanning at standard video rates enables us to see rapid, thermally transient events, which gives an opportunity to visualize temperature dynamics of the beating heart. Camera specification is

provided in Annex B Table B7. Circulation disorders in the tissue should be associated with local temperature changes. Some pictures taken from the thermovisual video stream are presented in Fig. 5.14.

At present, corrections of many cardiac disorders are treated by applying some destructive energy sources. One of the most common sources and the related methodology is to use radiofrequency ablations.

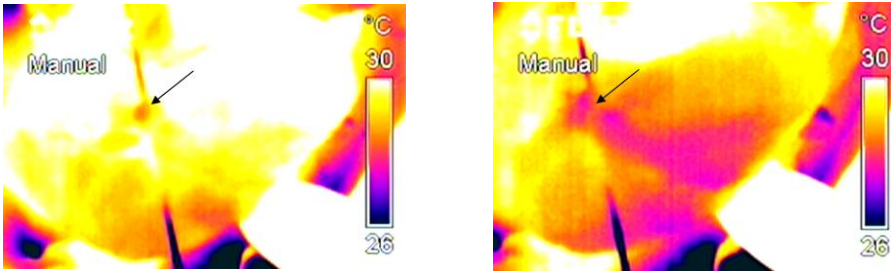


Fig. 5.14. Artery dressing location (*left-hand side*), spreading of cold across the left ventricular wall (*right-hand side*)

In medical practice treatment capabilities have expanded almost to the whole area of the cardiac texture zones. However, despite the latest technical, navigational methods for localizing the affected zone, the rate of the risk of complications, including a disease recurrence, remains very high and in some case may reach 70 % (Tan *et al.* 2008). Thus, in order to understand the nature of possible complications, the technique of thermovisual monitoring can be introduced. This technique is a non-invasive method and enables us to track the temperature changes over time. Thermovisual data offer a possibility to use a wide range of analysis methods in terms of video or image processing. The object of the research proposed is to explore the impact of temperature on the heart texture anisotropy based on the thermovisual data in order to analyse the possibilities to reduce a risk of complications.

The pilot research has proved that the thermovisual data are rather promising for estimating the heart state (Lekas *et al.* 2009). Also, these results have shown the necessity to extend the research. The aim of this sub-section is to investigate the dependency parameters of the radiofrequency ablation (RFA) procedure by registering the dynamics of absorption and spread of heat on various cardiac structures over a certain time in a video stream (Dzemyda *et al.* 2008). Thus, by incorporating the methods of mathematical morphology and transformations, we can approximate the thermal anisotropy zone. Moreover, that enables us to automatically identify, register, and track the changes in the structure as well as to evaluate the dynamics in time of the affected zone (Fig. 5.14). In this section, we will disclose the dependency of the

area of the affected zone on the energy and time of radiofrequency ablation procedure.

Thus, in order to disclose the affected zone, the overview of the colour models will be accomplished. In general, colour which a human understands is the brain reaction to a visual stimulus. The precise colour description can be achieved by measuring the spectral power distribution of electromagnetic waves. However, in the case of human vision, it falls into redundancy. This is related to a human perception of the colour. The human eye roughly has three types of cones which can perceive red, green, and blue light (Shanker 2001). Moreover, by transmitting a signal to the brain together with the signals received by rods that measures the intensity, we are able to perceive colour. Later, a colour space can be defined. A colour space or model is nothing more than a method for creation, specification and visualization of a colour (Hunt and Horwood 1998). Hence, there is a lot of colour systems which are different and can be efficiently used in different applications. The CIE has defined (Rencz 1999) a system that classifies colours according to the human visual system (HVS). Using this system, we can specify any colour in terms of its CIE coordinates and hence be confident that a CIE defined colour will match another with the same CIE definition. In a sequel, a short description of the most popular colour systems will be provided.

The RGB (Red, Green, Blue) is an additive colour system, based on the tri-chromatic theory (Rencz 1999). Despite the fact that the RGB colour system is easy to implement, however it is nonlinear with a visual perception. This colour system is device-dependent and the specification of the colour is semi-intuitive (Ford and Roberts 1998).

The CMYK (Cyan, Magenta, Yellow, Black) colour system is also device dependent, but it is a subtractive colour system. This system is also nonlinear with a visual perception, Component $\{K\}$ (Black) is introduced to improve the density and the available colour gamut (Williams 2008). This colour system is mostly used in printing or in hard copy output related tasks.

The *Lab* (CIE*Lab*) is a spherical colour system and is considered to be perceptually uniform (Russ 2006) and nearly uniform with visual perception. This is related to the fact that this colour system is based on the CIE system of colour measurement which is based on the human vision, where $\{L\}$ is a gray-scale axis or luminance, while $\{a\}$ and $\{b\}$ are two orthogonal axes that define the colour and saturation. $\{a\}$ axis runs from red to green and $\{b\}$ axis runs from yellow to blue.

One of the most difficult tasks of image analysis and processing is to segregate objects in image. In order to better identify the problem domain area the characteristic, such as image intensity histogram distribution has been visualized for different colour systems (Fig. 5.15). The first row shows the $\{R\}$,

$\{G\}$, and $\{B\}$ channel histogram intensities, the middle line $\{L\}$, $\{a\}$, and $\{b\}$ intensities histogram, the lowest one represents $\{C\}$, $\{M\}$, $\{Y\}$, and $\{K\}$ channel intensity histograms. The intensity of the charts (middle line $\{a\}$ and lower line $\{M\}$) forms two classes of peaks, with different intensity densities. One the equivalence classes is the heated area, and the other represents the background. Further, by applying the histogram equalization procedure described in Section 2.3.2, the achieved results can be visualized in the spatial domain (Fig. 5.16).

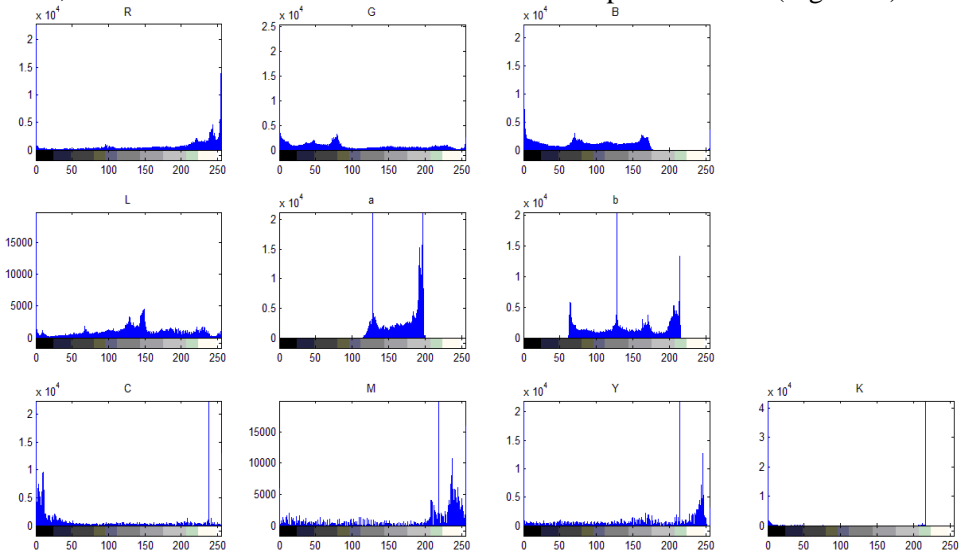


Fig. 5.15. The intensity distribution histograms of the colour systems channels

Fig. 5.15 shows the histograms of different colour system channels. On the x axis, the intensity levels are shown.



Fig. 5.16. Result in the $\{a\}$ colour channel (left-hand side), result in the $\{M\}$ colour channel (right-hand side)

5.3.1. Analysis of the Anisotropy Zone

As already mentioned in Section 5.3, one of the most difficult tasks for image analysis is to distinguish objects in contact. In order to identify the objects they must be segregated. Segregation is commonly accomplished by converting the intensity image into a black and white one. However, this task is not easy to implement. Basically, a problem arises in the context of different circumstances depending on which video was made. First of all, video stream was cut into frames and each frame was processed separately. The composition of steps required (Treigys *et al.* 2009) for each frame processing was the calculation of threshold level (see Section 2.3.3). Afterwards mathematical morphology processing was introduced in order to clear the objects in contact with the perimeter of the frame. This happens when the physician's hand acts closer to a microbolometer than the tissue being filmed. This results in greater emission of the heat registered by the thermal camera as well as in an anisotropy zone localization error. Moreover, the closing operation of mathematical morphology (see Section 2.2.1) was used to fill the dark holes of the heated zone resulting after the threshold operation. Finally, the zone perimeter marker was put around the segmented anisotropy zone (Fig. 5.17).



Fig. 5.17. Segmented heated zone

Fig. 5.17 represents the heated zone that was segmented automatically. A double line around the heated area is due to the fact that the segmentation was performed using two colour systems. In order to evaluate the dynamics of the heated area, the temperature range was fixed on the thermal camera. If the temperature range was not fixed, we only could evaluate the temperature dynamics with respect to the fixed anisotropy zone, but not the area dynamics with respect to the changing temperature.

5.3.2. Analysis of Heart Tissue Damage Dynamics

The lesions were experimentally assessed on the pulmonary vein and atrium with different features of the experimental conditions. Both the pulmonary vein and atrium were exposed by epicardial electrodes, of different impulse current power and different lesion time. The parameters that describe the experiment on pulmonary veins are presented in Table 5.4 and that on atrium in Table 5.5. All the experiments were carried out while the range of temperature recorded by the thermovisor was fixed, namely, the range of 29–41 °C. Further, the recorded footage was analysed. The analysis covered the tissue reaction to lesion. Some individual frames from the video footage with the approximated lesion are provided in Fig. 5.18.

Table 5.4. Experiment parameters of the pulmonary vein lesions

Experiment No.:	Power of electrode	Lesion time
1	20 Watts	10 Seconds
2	20 Watts	20 Seconds
3	30 Watts	10 Seconds
4	30 Watts	20 Seconds
5	50 Watts	10 Seconds
6	50 Watts	20 Seconds

Table 5.5. Experiment parameters of the atrium lesions

Experiment No.:	Power of electrode	Lesion time
1	20 Watts	20 Seconds
2	30 Watts	20 Seconds
3	50 Watts	20 Seconds

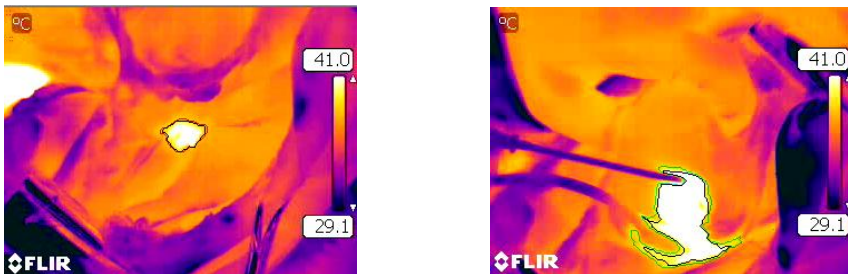


Fig. 5.18. The lesion of the pulmonary vein (*left-hand side*), the lesion of atrium (*right-hand side*)

As is shown in the Fig. 5.18, lesions in the different tissue sites are different. Moreover, since all the experiments were filmed by thermal camera it is possible to analyse the dynamics of the anisotropy zone referring to the electrode impulse current power and lesion duration. Results are presented in Annex C in Fig. C1 and C2. In both figures, lesion area in pixels is presented on the *y* axis, and footage frames are presented on the *x* axis.

Next, the cone fitting to the data points that represent the lesion area was accomplished. The analysis of the data has showed that it suffices the 5th order polynomial to maintain $R^2 > 0.9$ criteria in most cases (see Annex C from Fig. C3 to Fig. C9). R^2 is a fraction of the variance in the data that is explained by regression. The data for the fitting process were normalized by the mean and standard deviation. If the parametric cone is represented as $y = ax^5 + bx^4 + cx^3 + dx^2 + ex + f$, then the values for each experiment of the parameters are provided in Table 5.6 and Table 5.7.

Table 5.6. Parameters of the cone for a separate experiment on the pulmonary vein

Parameters/Experiment	<i>a</i>	<i>b</i>	<i>c</i>	<i>d</i>	<i>e</i>	<i>f</i>	R^2
20 Watts 10 seconds	3.23	3.85	-5.56	-114.8	-2.04	288.2	0.96
20 Watts 20 seconds	63.37	25.11	-201	-254.3	95.05	615	0.95
30 Watts 10 seconds	-26.4	-12.35	219.3	-96.27	-437	425.6	0.98
30 Watts 20 seconds	50.65	50.61	-93.08	-344.4	-99.3	661.3	0.95
50 Watts 10 seconds	-31.1	8.87	231.9	-147	-432	398.5	0.94
50 Watts 20 seconds	88.84	102.2	-243.6	-481.5	11.6	734.6	0.96

Table 5.7. Parameters of the cone for separate experiment on atria

Parameters/Experiment	<i>a</i>	<i>b</i>	<i>c</i>	<i>d</i>	<i>e</i>	<i>f</i>	R^2
20 Watts 20 seconds	-15.02	3.83	60.63	-234.3	-62.4	630.3	0.69
30 Watts 20 seconds	269.5	-423.8	-577.9	1149	-846	756.4	0.98
50 Watts 20 seconds	253.7	-294.9	-567.7	830	-901	1084	0.96

As it can be seen in Fig. C1 in Annex C, dynamics of the anisotropy zone is essentially different from the rest when the zone is operated at an electrode impulse current power of 20 Watts and the operation time is set to 10 seconds. In the case of pulmonary veins anisotropy, where the applied impulse current power outputs of the electrode are 20 and 30 Watts, respectively, after 20 seconds of operation dynamics of the lesion affected area remains almost identical. However, when the electrode impulse current output power is set to 50 Watts, at the beginning the region of lesion spreads dynamically, but the cooling period is much faster than in the case of application of 20 or 30 Watts output

power, respectively. Furthermore, according to the data provided in Fig. C2 in Annex C, atrium tissue dynamics of the damage area is almost identical when the electrode impulse current output power of 30 and 50 Watts was applied, during heating and cooling periods (Fig. 5.19 and Fig. 5.20).

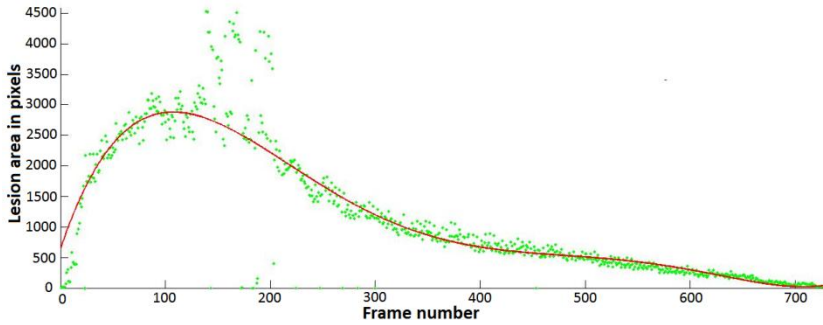


Fig. 5.19. Approximated data points by a polynomial.
Case: atria; parameters: 30 Watts 20 seconds

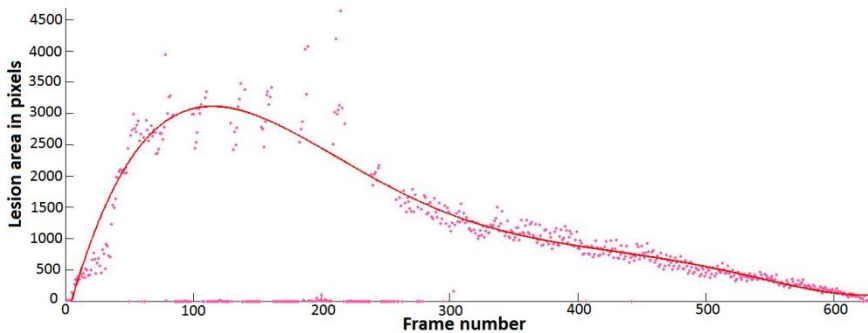


Fig. 5.20. Approximated data points by a polynomial.
Case: atria; parameters: 50 Watts 20 seconds

By investigating this topic in a broader context, it is not necessary to limit ourselves to the available colour system channels. It is possible to construct a nonlinear ways for video signal to be represented as pixel intensities in a spatial domain. A possible nonlinear approach is obtained by using the *Lab* colour system properties. Using this colour system, all pixels can be compared together by Euclidean distances. In this case, the distance can be thought as some similarity measure. Suppose that we want to compare the values of all points, defined in *Lab* colour system, with the black point value. To this end we construct a N by M matrix, where N is the image width and M is the image height. Each element in the matrix corresponds to the distance between the

current point and the black point value. After rearranging the matrix distance values in the interval $[0 \dots 255]$, it comes possible to visualize the image in a spatial domain as the intensity image. Finally, after applying the histogram adjustment and automated threshold calculation, the resulting image with separated classes is shown in Fig. 5.21.

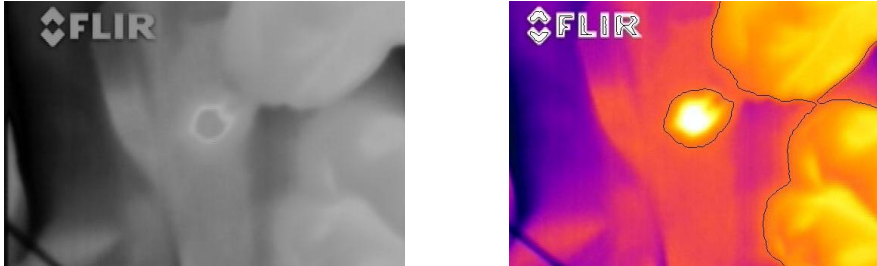


Fig. 5.21. Euclidian distance matrix as the intensity image (*left-hand side*), two class separation result in Euclidean distance matrix (*right-hand side*)

Another experiment was carried out using the method of principal component analysis. This method was used to find out the correspondence of pixel points with $\{R\}$, $\{G\}$, and $\{B\}$ components correspondence to gray intensity. To achieve this goal, the video stream from the thermovisor was split into frames, then, for each frame, the principal directions of components of all pixels $\{R\}$, $\{G\}$, and $\{B\}$ were calculated. Next, by selecting the direction with the largest dispersion, we calculate the projection of colour components for each frame pixel in the selected direction. Finally, the calculated projection is rearranged in the interval $[0 \dots 255]$. After the principal component analysis the resulting images as well as the classified image are shown in Fig. 5.22.

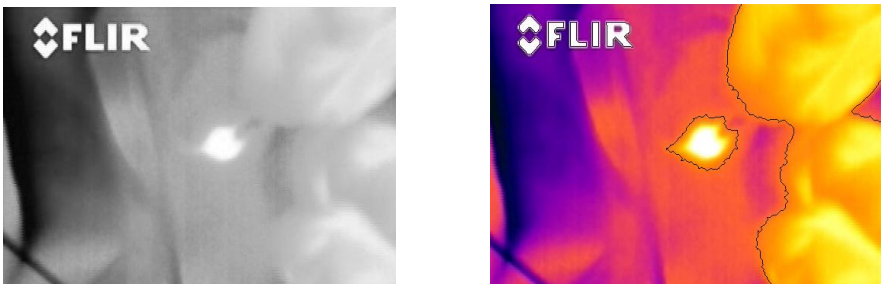


Fig. 5.22. Image after principal component analysis (*left-hand side*), classification result (*right-hand side*)

It should be noted that, in this experiment, we did not have a possibility to choose real temperatures from the thermal camera, only video footage was taken into consideration. However, the analysis of data in a wider context has revealed that, if we were aware how the thermal camera converts the temperature to colour representation, then the temperature could be visualized as an image, thus the problem would remain the same, i. e., to distinguish two classes in the provided image.

In this sub-section the investigation of the thermovisual data was carried out with a view to identify the thermal anisotropy dynamics in different heart tissues that are under the sway of radio frequency ablation procedure. Proposed method let us measure and record the tissue temperature changes. This, in turn, enables to decrease the rate of the risk of complications. The method proposed rely on the analysis of the colour spaces, mathematical morphological processing and the result clusterization by the Otsu method.

5.4. Conclusions for the Fifth Section

Evaluation of the developed software of the OND parameterization showed that it produces parameters of the optic nerve disc which are similar to that of one of fifteen physicians' measurements. The OND size, calculated by the software, is usually obtained slightly larger than that obtained by the majority of physicians.

Besides, the artificial neural network was investigated as a healthy-glaucoma disease classifier. In both cases, whether the pre-processed data whether not were used, the classification accuracy of 97.91 % was achieved. However, variation of SSE response and large dispersion values implies that the results may be questionable.

Further, proposed method for thermovisual data processing let us measure and record the tissue temperature changes. This, in turn, allows the real time control of destruction boundaries of the tissue in order to avoid adverse effects and preserve the structures in which the damage would have injurious consequences.

The principal component analysis, as well as the analysis of vector lengths have exposed that the task comes to a two-class separation problem, regardless of the manner in which the initial colour system pixel intensities are mapped on the gray level intensity interval. For example, he analysis made on the spread of the risk area using the electrode ablation impulse current power of 30 or 50 Watts and the operation time of 20 seconds, has shown that the tissue thermal anisotropy dynamics, is almost the same in heating and cooling stages.

Conclusions

A large amount of data is produced by technological means in everyday practice. The collected data cannot be examined in detail by a human since the amount is too large, however, this provides the crucial information on the state of the patient. Thus, the techniques of data mining, pattern recognition, and knowledge discovery are very efficient and can be used for decision support. The topics investigated in the thesis allow us to conclude that:

1. A disc-shaped structuring element can be used for the blood vessel tree extraction and removal tasks from colour eye fundus images. In the case of vasculature extraction the computation time is saved and every image pixel that represent a vessel is processed.
2. The recombination of processed channels of the retinal image by the mathematical morphological closing operation does not cause a colour distortion. It results in the 98 % optic nerve disc localization accuracy. The elliptic parameters, obtained by the proposed algorithm, on the average did not differ from those obtained by the reference points more than 10 %.
3. The blood vessel tree is unique and can be used for eye fundus registration. The algorithm, proposed, for blood vessel extraction that uses disc-shaped structuring element, enables us to position eye fundus images according to the features of global topology. Thus, a linear transformation is sufficient to

solve the eye fundus image registration problem. The analysis of a set of retinal images has showed that the registration quality parameter is sufficient and occurs within the framework of 20–40 decibels, which indicates the qualitative result of registration.

4. The analysis of the peak-signal-to-noise parameter has revealed that the algorithm proposed for image registration is also suitable to solve the identification-related class problems. However, a more thorough analysis should be made in order to evaluate the identification results.
5. The analysis of the principal components as well as of vector lengths has proved that the problem of unknown temperatures can be reduced to that of separating two classes, no matter how the initial colour system pixel intensities are mapped into the gray level intensity interval.
6. The analysis of spread of the risk area, made according to the electrode ablation impulse current power and time, has showed that the tissue thermal anisotropy dynamics, regarding 30 and 50 Watt power and 20 seconds lesion time settings on the atria tissue, remains almost the same during heating and cooling stages.
7. The artificial neural network with one hidden layer was tested as a healthy-glaucoma disease classifier. The classification accuracy of 97 % was achieved on the initial as well as pre-processed data. However, in both cases the variation of sum of squared error response may mean that either the given parameters do not reflect the real incidence of classes, or this parameter system is improper for the classification task.

References

Abraham, A.; Nath, B. 2001. ALEC: An Adaptive Learning Framework for Optimizing Artificial Neural Networks, in *Proceedings of the International Conference on Computational Science*, 2, 171–180.

Analytical Imaging Facility. 2005. *Examples of Scanning Electron Microscopy*. Retrieved 01 14, 2010, from Analytical Imaging Facility: <http://www.aecom.yu.edu/aif/gallery/sem/sem.htm>

Apte, C.; Weiss, S. 1997. Data Mining with Decision Trees and Decision Rules, *Future Generation Computer Systems* 13: 197–210. ISSN 0167-739X

Ashbrook, A.; Thacker, A. N. 1998. *Tutorial: Algorithms For 2-Dimensional Object Recognition*. Retrieved 01 14, 2010, from TINA: Open Source Image Analysis Environment: <http://www.tina-vision.net/docs/memos/1996-003.pdf>

Avdelidis, N. P.; Moropoulou, A. 2003. Emissivity Considerations in Building Thermography, *Energy and Buildings* 35(7): 663–667. ISSN 0378-7788

Ballard, H. D. 1981. Generalizing the Hough Transform to Detect Arbitrary Shapes, *Pattern Recognition* 13(2): 111–121. ISSN 0031-3203

Bernatavičienė, J. 2008. *Vizualios žinių gavybos metodologija ir tyrimas*. Vilnius: Technika.

Bernatavičienė, J.; Dzemyda, G.; Kurasova, O.; Marcinkevičius, V. 2006. Decision Support for Preliminary Medical Diagnosis Integrating the Data Mining Methods,

- in *Simulation and Optimisation in Business and Industry: 5th International Conference on Operational Research*, 155–160.
- Bernatavičienė, J.; Dzemyda, G.; Kurasova, O.; Marcinkevičius, V. 2005. Optimal Decisions in Combining the SOM with Nonlinear Projection Methods, *European Journal of Operational Research* 173(3): 729–745. ISSN 0377-2217
- Bernatavičienė, J.; Dzemyda, G.; Kurasova, O.; Marcinkevičius, V.; Medvedev, V. 2007. The Problem of Visual Analysis of Multidimensional Medical Data, A. Torn; J. Žilinskas (eds.), *Models and Algorithms for Global Optimization*, 4: 277–298. New York: Springer.
- Basevičius, A. 2005. *Radiologijos pagrindai*. Kaunas: KMU spaudos ir leidybos centras.
- Berry, M. W.; Browne, M. 2006. *Lecture Notes in Data Mining*. Singapore: World Scientific.
- Bookstein, F. 1979. Fitting Conic Sections to Scattered Data, *Computer Vision and Image Processing* 9: 56–71. ISSN 0734-189X
- Boyd, J. 1996. STARE Software Documentation: disk - Optic Disk Locator. San Diego: University of California.
- Bozzola, J. J.; Lonnie, R. D. 1998. *Electron Microscopy* (2nd Edition). Sudbury: Jones & Bartlett Publishers.
- Brown, M. A.; Semelka, R. C. 2003. *MRI: Basic Principles and Application* (3rd Edition). Wilmington: Wiley-Liss.
- Can, A.; Stewart, C.; Roysam, B.; Tanenbaum, H. 2002. A Feature-based, Robust, Hierarchical Algorithm for Registering Pairs of Images of the Curved Human Retina, *IEEE Transactions on Pattern Analysis and Machine Intelligence* 24(3): 347–364. ISSN 0162-8828
- Canny, J. 1986. A Computational Approach to Edge Detection, *IEEE Transactions on Pattern Analysis and Machine Intelligence* 8(6): 679–698. ISSN 0162-8828
- Carlton, R. R.; Adler, A. M.; Frank, E. D. 2005. *Principles of Radiographic Imaging*. New York: Thomson Delmar Learning.
- Chanwimaluang, T.; Guoliang, F.; Fransen, S. 2006. Hybrid Retinal Image Registration, *IEEE Transactions on Technology in Biomedicine* 10(1): 129–142. ISSN 1089-7771
- Chaudhuri, S.; Chatterjee, S.; Katz, N.; Nelson, M.; Goldbaum, M. 1989. Automatic Detection of the Optic Nerve in Retinal Images, in *Proceedings of the IEEE International Conference on Image Processing*, 1–5.
- Choe, T.; Cohen, I. 2005. Registration of Multimodal Fluorescein Images Sequence of the Retina, in *Proceedings of IEEE International Conference on Computer Vision*, 1, 106–113.

- Cios, K. J.; Swiniarski, R. W.; Pedrycz, W.; Kurgan, L. A. 2007. *Data Mining A Knowledge Discovery Approach*. New York: Springer.
- Cios, K.; Pedrycz, W.; Swiniarski, R. 1998. *Data Mining Methods for Knowledge Discovery*. Dordrecht: Kluwer.
- Dongxiang, X.; Hwang, J.; Yuan, C. 2000. Atherosclerotic Blood Vessel Tracking and Lumen Segmentation Intopology Changes Situations of MR Image Sequences, in *Proceedings of International Conference on Image Processing*, 1, 637–640.
- Dunham, M. H. 2002. *Data Mining: Introductory and Advanced Topics*. New Jersey: Prentice Hall.
- Dykstra, M. J.; Reuss, L. E. 2003. *Biological Electron Microscopy - Theory, Techniques, and Troubleshooting*. Norwell: Kluwer Academic Publishers.
- Dzemyda, G.; Veikutis, V.; Jakuška, P.; Puodžiukynas, A.; Treigys, P.; Medvedev, V. 2008. *Specializuotų duomenų analizės metodų kūrimas širdies audinių temperatūrinei anizotropijai tirti*. Vinius: Matematikos ir Informatikos Institutas.
- Farr, R. F.; Allisy-Roberts, P. J. 1996. *Physics for Medical Imaging*. Berkshire: Bailliere Tindall.
- Fayyad, U. M.; Piatetsky-Shapiro, G.; Smyth, P. 1996. Knowledge Discovery and Data Mining: Towards a Unifying Framework, in *Proceedings of the 2nd International Conference on Knowledge Discovery and Data Mining*, 82–88.
- Fielding, A. H. 2006. *Cluster and Classification Techniques in the BioSciences*. Cambridge: Cambridge University Press.
- Fitzgibbon, W. A.; Pilu, M.; Fisher, B. R. 1999. Direct Least-squares Fitting of Ellipses, *Transactions on Pattern Analysis and Machine Intelligence* 21(5): 476–480. ISSN 0162-8828
- Foracchia, M.; Grisan, E.; Ruggeri, A. 2004. Detection of the Optic Disc in Retinal Images by Means of a Geometrical Model of Vessel Structure, *IEEE Transactions on Medical Imaging* 23(10): 1189-1195. ISSN 0278-0062
- Ford, A.; Roberts, A. 1998. *Colour Space Conversions*. Retrieved 01 17, 2010, from Charles Poynton: <http://www.poynton.com/PDFs/coloureq.pdf>
- George, D. 2006. *Resident Physics Course*. Retrieved 01 14, 2010, from Medical College of Georgia: <http://www.radiology.mcg.edu/RadiologyPhysics/us/06USDoppler.ppt>
- Goldbaum, M.; Moezzi, S.; Taylor, A.; Chatterjee, S.; Boyd, J.; Hunter, E.; Jain, R. 1996. Automated Diagnosis and Image Understanding with Object Extraction, Object Classification, and Inferencing in Retinal Images, in *Proceedings of the IEEE International Conference on Image Processing*, 695–698.

- Gonzalez, R.; Woods, R. 1992. *Digital Image Processing* (3rd Edition). Reading: Addison-Wesley Publishing.
- Goutsias, J.; Heijmans, H.; Sivakumar, K. 1995. Morphological Operators for Image Sequences, *Computer Vision and Image Understanding* 62(3): 326–346. ISSN: 1077-3142
- Grau, V.; Downs, C. J.; Burgoyne, F. C. 2006. Segmentation of Trabeculated Structures Using an Anisotropic Markov Random Field: Application to the Study of the Optic Nerve Head in Glaucoma, *Transactions on Medical Imaging* 25(3): 245–255. ISSN 0278-0062
- Gruppen, C.; Cowan, G.; Eidelman, S. D.; Stroh, T. 2005. *Astroparticle Physics*. New York: Springer.
- Han, J.; Kamber, M. 2005. *Data Mining: Concepts and Techniques* (2nd Edition). San Fransisco: Morgan Kaufmann.
- Hand, D.; Mannila, H.; Smyth, P. 2001. *Principles of Data Mining*. Cambridge: MIT Press.
- Handbury, A.; Serra, J. 2001. Mathematical Morphology in the HLS Colour Space, in *Proceedings of the 12th British Machine Vision Conference*, 451–460.
- Handbury, A.; Serra, J. 2002. Mathematical Morphology in the Lab Colour Space, *Image Analysis and Stereology* 21(3): 201–206. ISSN 1580-3139
- Handbury, A.; Serra, J. 2001. Morphological Operators on the Unit Circle, *IEEE Transactions on Image Processing* 12(10): 1842–1850. ISSN 1057-7149
- Hastie, T.; Tibshirani, R.; Friedman, J. 2009. *The Elements of Statistical Learning* (2nd Edition). New York: Springer-Verlag.
- Hendee, R. W.; Ritenour, R. E. 2003. *Medical Imaging Physics* (4th Edition). Hoboken: John Willey and Sons.
- Hoover, A.; Goldbourn, M. 2003. Locating the Optic Nerve in a Retinal Image Using the Fuzzy Convergence of the Blood Vessels, *Transactions on Medical Imaging* 22(8): 951–958. ISSN 0278-0062
- Hough, V.; Paul, C. 1962. *Patent No. 3069654*. US.
- Hunt, R. W.; Horwood, E. 1998. *Measuring Colour* (3rd Edition). New York: Fountain Press.
- Hurley, A. P. 2005. *A Concise Introduction to Logic* (9th Edition). Florence: Wadsworth Publishing .
- Izmailov, V.; Novoselova, M.; Naumov, A. 2009. Forecasting of Electric Contact Residual Lifetime Based on Statistical Analysis of Thermovision Monitoring, *Russian Electrical Engineering* 80(5): 289–292. ISSN 1068-3712

- Janulevičienė, I.; Barzdziukas, V.; Jankauskienė, J.; Žemaitienė, R.; Žaliūnienė, D.; Milašienė, J.; Jašinskas, V.; Špečkauskas, M. 2008. *Lazerinių technologijų panaudojimas akių ligų diagnostikai*. Kaunas: VitaeLitera.
- Jegelevičius, D.; Buteikiene, D.; Barzdziukas, V.; Paunksnis, A. 2008. Parameterization of the Optic Nerve Disc in Eye Fundus Images, in *Proceedings of 14th Nordic-Baltic Conference on Biomedical Engineering and Medical Physics*, 20(8), 528–531.
- Jegelevičius, D.; Lukosevicius, A.; Paunksnis, A.; Barzdziukas, V. 2002. Application of Data Mining Technique for Diagnosis of Posterior Uveal Melanoma, *Informatica* 13(4): 455–464. ISSN 0868-4952
- Johnson, K. A.; Becker, A. 1999. *Hypertensive Encephalopathy*. Retrieved 01 14, 2010, from Harvard Medical School: <http://www.med.harvard.edu/AANLIB/cases/case21/mr3/013.html>
- Johnson, S. 2006. *Stephen Johnson on Digital Photography*. Sebastopol: O'Reilly Media.
- Karmen, E.; Heck, B. 2002. *Fundamentals of Signals and Systems Using the Web and Matlab* (2nd Edition). New Jersey: Prentice Hall.
- Kecman, V. 2001. *Learning and Soft Computing*. Cambridge: The MIT Press.
- Khan, M. R.; Abraham, A. 2003. Short Term Load Forecasting Models in Czech Republic Using Soft Computing Paradigms, *International Journal of Knowledge-Based and Intelligent Engineering System* 7(4): 172–179. ISSN 1327-2314
- Komorowski, J.; Pawlak, Z.; Polkowski, L.; Skowron, A. 1999. *Rough Sets: A Tutorial, Rough Fuzzy Hybridization. A New Trend in Decision-Making*. New York: Springer-Verlag.
- Kuisienė, N.; Raugalas, J.; Čitavičius, D. 2008. Comparative Sequence Analysis of 16S-23S rRNA Internal Transcribed Spacers of the Genus *Geobacillus*, *Biologija* 54(1): 1–6. ISSN 1392-0146
- Lamb, W. E.; Retherford, R. C. 1947. Fine Structure of the Hydrogen Atom by a Microwave Method, *Physical Review* 72(3): 241–243. ISSN 1050-2947
- Louverdis, G.; Vardavoulia, M.; Andreatis, I.; Tsalides, P. 2002. A New Approach to Morphological Colour Image Processing, *Pattern Recognition* 35(8): 1733–1741. ISSN 0031-3203
- Lowell, J.; Hunter, A.; Steel, D.; Basu, A.; Ryder, R.; Kennedy, R. L. 2004. Measurement of Retinal Vessel Widths from Fundus Images Based on 2-D Modeling, *IEEE Transactions on Medical Imaging* 23(10): 1196–1204. ISSN 0278-0062
- Lowell, J.; Hunter, A.; Steel, D.; Basu, A.; Ryder, R.; Fletcher, E.; Kennedy, L. 2004. Optic Nerve Head Segmentation, *IEEE Transactions on Medical Imaging* 23(2): 256–264. ISSN 0278-0062

- Mačiulis, A.; Paunksnis, A.; Barzdžiukas, V.; Kriaučiūnienė, L.; Buteikienė, D.; Puzienė, V. 2009. Digital Model of Blood Circulation Analysis System, *Informatica* 20(4): 539–554. ISSN 0868-4952
- Marquardt, D. W. 1963. An Algorithm for Least-Squares Estimation of Nonlinear Parameters, *Journal on Applied Mathematics* 11(2): 431–441. ISSN 0272-4960
- Matsopoulos, G. K.; Asvestas, P. A.; Mouravliansky, N. A.; Delibasis, K. K. 2004. Multimodal Registration of Retinal Images Using Self Organizing Maps, *IEEE Transactions on Medical Imaging* 23(12): 1557–1563. ISSN 0278-0062
- Medical Physics and Bioengineering. 2010. *Photoacoustic Imaging Group*. Retrieved 01 13, 2010, from Medical Physics and Bioengineering: <http://www.medphys.ucl.ac.uk/research/mle/images.htm>
- Medvedev, V. 2007. Tiesioginio sklaidimo neuroninių tinklų taikymo daugiamatiams duomenims vizualizuoti tyrimas. Vilnius: Technika.
- Mendels, F.; Heneghan, C.; Thiran, P. J. 1999. Identification of the Optic Disk Boundary in Retinal Images Using Active Contours, in *Proceedings of Irish Machine Vision and Image Processing Conference*, 103–115.
- Mitchell, D. G.; Cohen, M. 2004. *MRI Principles* (2nd Edition). Philadelphia: Elsevier Saunders.
- Mitra, S.; Mitra, P.; Pal, S. K. 2001. Evolutionary Modular Design of Rough Knowledge-based Network Using Fuzzy Attributes, *Neurocomputing* 36(1): 45–66. ISSN 0925-2312
- Mitra, S.; Pal, S. K.; Mitra, P. 2002. Data Mining in Soft Computing Framework: A Survey, *IEEE Transactions on Neural Networks* 13(1): 3–14. ISSN 1045-9227
- Moreau, Y.; Antal, P.; Fannes, G.; De Moor, B. 2003. Probabilistic Graphical Models for Computational Biomedicine, *Methods of Information in Medicine* 41(2): 161–168. ISSN 0026-1270
- Morris, D. T.; Donnison, C. 1999. Identifying the Neuroretinal Rim Boundary Using Dynamic Contours, *Image and Vision Computing* 17(13): 169–174. ISSN 0262-8856
- Mukherjee, J.; Kumar, A. M.; Das, P. P.; Chatterji, B. N. 2002. Use of Medial Axis Transforms for Computing Normals at Boundary Points, *Pattern Recognition Letters* 23(14): 1649–1656. ISSN 0167-8655
- Netravali, A. N.; Haskell, B. G. 1995. *Digital Pictures Representation, Compression, and Standards* (2nd Edition). New York: Plenum Press.
- New York Eye and Ear Infirmary. 2010. *Retinal Imaging: A Historical Perspective*. Retrieved 01 14, 2010, from New York Eye and Ear Infirmary: http://www.nyee.edu/aric_03.html

- Noda, E.; Freitas, A. A.; Lopes, H. S. 1999. Discovering Interesting Prediction Rules with a Genetic Algorithm, in *Proceedings of the Congress on Evolutionary Computations*, 2, 1322–1329.
- Osarech, A. 2004. Automated Identification of Diabetic Retinal Exudates and the Optic Disc. Bristol: University of Bristol.
- Otsu, N. 1979. A Threshold Selection Method from Gray-level Histograms, *IEEE Transactions on Systems, Man, and Cybernetics* 9(1): 62–66. ISSN 1094-6977
- Pal, S. K. 2001. Soft Computing Pattern Recognition: Principles, Integrations, and Data Mining, in *Proceedings of the Joint Workshop on New Frontiers in Artificial Intelligence*, 261-271.
- Pal, S. K.; Mitra, P. 2004. *Pattern Recognition Algorithms for Data Mining*. Danvers: CRC Press.
- Parsons, R. E.; Marin, M. L.; Veith, F.; Sanchez, L.; Lyon, R.; Suggs, W.; Schwartz, F. 2005. Fluoroscopically Assisted Thromboembolectomy: An Improved Method for Treating Acute Arterial Occlusions, *Annals of Vascular Surgery* 10(3): 201–210. ISSN 1615-5947
- Paunksnis, A. 2009. Informacinės klinikinių sprendimų palaikymo ir gyventojų sveikatinimo priemonės e. Sveikatos sistemos. Kaunas: Kauno medicinos universiteto klinikos.
- Paunksnis, A. 2006. Informacinės technologijos žmogaus sveikatai – klinikinių sprendimų palaikymas (e-sveikata). IT sveikata. Kaunas: Kauno medicinos universiteto klinikos.
- Peters, R. 1997. Mathematical Morphology for Angle-valued Images, in *Proceedings on Non-Linear Image Processing*, 8(3026), 84–94.
- Pinz, A.; Bernogger, S.; Datlinger, P.; Kruger, A. 1998. Mapping the Human Retina, *IEEE Transactions on Medical Imaging* 17(4): 606–619. ISSN 0278-0062
- Quinn, R. 1980. *Radiography in Modern Industry* (4th Edition). Columbus: American Society for Nondestructive Testing.
- RadiologyInfo. 2010. *Chest X-ray*. Retrieved 01 14, 2010, from RadiologyInfo: <http://www.radiologyinfo.org/en/info.cfm?pg=chestrad>
- Rao, S. S. 1984. Optimization: Theory and Applications. New York: Wiley.
- Rencz, A. N. 1999. *Remote Sensing for the Earth Sciences* (3rd Edition). Hoboken: Wiley.
- Russ, J. C. 2006. *The Image Processing Handbook*. Boca Raton: CRC Press.
- Saarinen, S.; Bramley, R.; Cybenko, G. 1993. Ill-conditioning in Neural Network Training Problem, *SIAM Journal on Scientific Computing* 14(3): 693–714. ISSN 1064-8275

- Shanker, S. 2001. What Children Know When They Know What a Name Is: The Non-Cartesian View of Language Acquisition, *Current Anthropology* 42(4): 481–513. ISSN 0011-3204
- Shapiro, P. G.; Frawley, W. J. 1991. *Knowledge Discovery in Databases*. California: AAAI Press.
- Shih, F. 2009. Image Processing and Mathematical Morphology: Fundamentals and Applications. New York: CRC Press.
- Sinthanayothin, C.; Boyce, J.; Cook, H.; Williamson, T. 1999. Automated Localization of the Optic Disc, Fovea, and Retinal Blood Vessels from Digital Colour Fundus Images, *British Journal of Ophthalmol* 83(8): 902–910. ISSN 1468-2079
- Smith, W. S. 1997. *Scientist & Engineer's Guide to Digital Signal Processing*. San Diego: California Technical Publishing.
- Soares, J. V.; Leandro, J. J.; Cesar, R. M.; Jelinek, H. F.; Cree, M. J. 2006. Retinal Vessel Segmentation Using the 2-D Gabor Wavelet and Supervised Classification, *IEEE Transactions on Medical Imaging* 25(9): 1214–1222. ISSN 0278-0062
- Soille, P. 1999. *Morphological Image Analysis*. Berlin: Springer-Verlag.
- Staal, J.; Abramoff, M. D.; Niemeijer, M.; Viergever, M. A.; van Ginneken, B. 2004. Ridge-based Vessel Segmentation in Color Images of the Retina, *IEEE Transaction on Medical Imaging* 23(4): 501–509. ISSN 0278-0062
- Stewart, C.; Tsai, C.; Roysam, B. 2003. The Dual-bootstrap Iterative Closest Point Algorithm with Application to Retinal Image Registration, *IEEE Transaction on Medical Imaging* 22(11): 1379–94. ISSN 0278-0062
- Suraj, Z.; Delimata, P. 2006. Data Mining Exploration System for Feature Selection Tasks, in *Proceedings of the 2006 International Conference on Hybrid Information Technology*, 284–286.
- Tan, E.; Reinstra, M.; Wiesfield, M. 2008. Long-term Outcome of the Atrioventricular Node Ablation and Pacemaker Implantation for Symptomatic Refractory Atrial Fibrillation, *Europace* 10(4): 412–418. ISSN 1099-5129
- Taniar, D. 2007. *Research and Trends in Data Mining Technologies and Applications*. Hershey: IGI Publishing.
- The Advanced Fertility Center of Chicago. 2010. *Early Pregnancy Ultrasound Findings and Pictures at 5 to 6 weeks*. Retrieved 01 14, 2010, from The Advanced Fertility Center of Chicago: www.advancedfertility.com/ultrasol1.htm
- The MathWorks. 2010. *Morphology Fundamentals: Dilation and Erosion*. Retrieved 01 18, 2010, from The MathWorks: <http://www.mathworks.com/access/helpdesk/help/toolbox/images/f18-12508.html>

Thitiporn, C.; Guoliang, F. 2003. An Efficient Blood Vessel Detection Algorithm for Retinal Images Using Local Entropy Thresholding, in *Proceedings of the 2003 International Symposium on Circuits and Systems*, 5, 25–28.

Thrush, A.; Hartshorne, T. 1999. *Peripheral Vascular Ultrasound: how, why and when*. London: Churchill Livingstone.

Tobin, W. K.; Chaum, E.; Govindasamy, P. V.; Karnowski, P. T.; Sezer, O. 2006. Characterization of the Optic Disk in Retinal Imagery Using a Probabilistic Approach, *Progress in Biomedical Optics and Imaging* 7(2): 1–10. ISSN 1605-7422

Todd, A. 2000. *How MRI Works*. Retrieved 01 14, 2010, from How Stuff Works: <http://www.howstuffworks.com/mri.htm/printable>

Tolias, Y.; Panas, S. 1998. A Fuzzy Vessel Tracking Algorithm for Retinal Images Based on Fuzzy Clustering, *IEEE Transactions on Medical Imaging* 17(2): 263–273. ISSN 0278-0062

Tsai, C.; Majerovics, A.; Stewart, C.; Roysam, B. 2003. Disease-Oriented Evaluation of Dual-Bootstrap Retinal Image Registration, in *Proceedings of MICCAI*, 754–761.

Vardavoulia, M.; Aandreadis, I.; Tsalides, P. 2002. Vector Ordering and Morphological Operations for Colour Image Processing: Fundamentals and Applications, *Pattern Analysis and Applications* 5(3): 271–287. ISSN 1433-7541

Vatsavai, R. R.; Shekhar, S.; Burk, T. 2005. A Semi-Supervised Learning Method for Remote Sensing Data Mining, in *Proceedings of the 17th IEEE International Conference on Tools with Artificial Intelligence*, 207–211.

Veikutis, V.; Beneitis, R.; Širvinskas, E.; Jakuška, P.; Siudikas, A.; Mickevičius, T. 2008. Thermovision in Cardiac Surgery Practice: New Viewpoint and Possibilities, in *Proceedings of the Biomedical Engineering*, 51–54.

Vermer, A. K.; Vos, M. F.; Lemij, G. H.; Vossepoel, M. A. 2004. A Model Based Method for Retinal Blood Vessel Detection, *Computers in Biology and Medicine* 34: 209–219. ISSN 0010-4825

Williams, R. 2008. *Non-Designer's Design Book* (3rd Edition). Berkeley: Peachpit Press.

Witten, H.; Frank, E. 2005. *Data Mining: Practical Machine Learning Tools and Techniques* (2nd Edition). San Fransisco: Morgan Kaufmann.

Wygant, I. O.; Zhuang, X.; Kuo, P. S.; Yeh, D. T.; Oralkan, O.; Khuri-Yakub, B. T. 2005. Photoacoustic Imaging Using a Two-dimensional CMUT Array, in *Proceedings of the IEEE Ultrasonics Symposium*, 4, 1921–1924.

Xu, J.; Chutatape, O.; Sung, E.; Zheng, C.; Kuan, T. C. 2007. Optic Disk Feature Extraction via Modified Deformable Model Technique for Glaucoma Analysis, *Pattern Recognition* 40(7): 2063–2076. ISSN 0031-3203

- Ye, J. 2007. Least Squares Linear Discriminant Analysis, in *Proceedings of the 24th International Conference on Machine Learning*, 1087–1093.
- Young, T. I.; Gerbandis, J. J.; van Vliet, J. L. 2003. *Morphology-based Operations*. Retrieved 03 10, 2005, from Image Processing Fundamentals: <http://www.ph.tn.tudelft.nl/Courses/FIP/noframes/fip-Morpholo.html>
- Zana, F.; Klein J. 1999. A Multimodal Registration Algorithm of Eye Fundus Images Using Vessels Detection and Hough Transform. *IEEE Transactions on Medical Imaging*, 18(5), 419–428. ISSN 0278-0062
- Zhang, E. Z.; Laufer, J. G.; Pedley, R. B.; Beard, P. C. 2009. In Vivo High-resolution 3D Photoacoustic Imaging of Superficial Vascular Anatomy, *Physics in Medicine and Biology* 4: 1035–1046. ISSN 0031-9155
- Zupan, B.; Keravnou, E.; Lavrac, N. 1997. *Intelligent Data Analysis in Medicine and Pharmacology*. Dordrecht: Kluwer Academic Publishing.
- Žitkevičius, E. 2007. Medicininių vaizdų analizė ir tyrimas spektriniais metodais. Vilnius: Technika.

The List of Scientific Author's Publications on the Subject of the Dissertation

Articles in reviewed publications

Lekas, R.; Jakuška, P.; Kriščiukaitis, A.; Veikutis, V.; Dzemyda, G.; Mickevičius, T.; Morkūnaitė, K.; Vilké, A.; Treigys, P.; Civinskienė, G.; Andriuškevičius, J.; Vanagas, T.; Skauminas, K.; Bernatoniene, J. 2009. Monitoring Changes in Heart Tissue Temperature and Evaluation of Graft Function after Coronary Artery Bypass Grafting Surgery, *Medicina* 45(3): 221–225. ISSN 1648-9144 (*ISI Web of Science*)

Treigys, P.; Šaltenis, V.; Dzemyda, G.; Barzdžiukas, V.; Paunksnis, A. 2008b. Automated Optic Nerve Disc Parameterization, *Informatica* 19(3): 403–420. ISSN 0868-4952 (*ISI Web of Science*)

Treigys, P.; Šaltenis, V. 2007. Neural Network as Ophthalmologic Disease Classifier, *Information Technology and Control* 36(4): 365–371. ISSN 1392-124X (*ISI Web of Science*)

Treigys, P.; Dzemyda, G.; Barzdžiukas, V. 2008a. Automated Positioning of Overlapping Eye Fundus Images, in *Lecture Notes in Computer Science*,

5101/2008, 1: 197–202. ISSN 0302-9743 (*Conference Proceedings Citation Index, SpringerLINK, Compendex, MatSciNet, GeoRef, INSPEC*)

Treigys, P. 2005b. Kraujagyslių šalinimas spalvotose akies dugno nuotraukose, *Informacijos mokslai* 34: 227–232. ISSN 1392-0561 (*CEEOL, LISA*)

Articles in other publications

Šaltenis, V.; Treigys, P. 2005. Kraujagyslių tinklo išskyrimas akies dugno nuotraukose, iš *Biomedicininė inžinerija*, 265–268.

Treigys, P. 2005a. Automatinis regos nervo disko atpažinimas akių dugno nuotraukose, iš *Informacinės technologijos*, 2, 796–800.

Treigys, P.; Dzemyda, G.; Veikutis, V. 2009. Investigation of Thermal Anisotropy from Thermovisual Video Data, in *GraVisMa: Computer Graphics, Vision and Mathematics*, 45.

Treigys, P.; Šaltenis, V.; Dzemyda, G.; Barzdžiukas, V. 2006. Automated Optic Nerve Disk Parameterization, in *Proceedings of 6th Nordic Conference on eHealth and Telemedicine*, 67–68.

Veikutis, V.; Kazakevičius, T.; Dzemyda, G.; Mickevičius, T.; Morkūnaitė, K.; Pečkauskas, A.; Vilkė, A.; Puodžiukynas, A.; Šileikis, V.; Zabiela, V.; Treigys, P.; Marcinkevičius, V. 2008b. Radiodažninės energijos destruktinio poveikio ir miokardo pažaidos ypatumai naudojant standartinius intrakardinius elektrodus, iš *Biomedicininė inžinerija*, 55–58.

ANNEXES

Annex A. Analysis Results of the OND Parameters

Table A1. Analysis data for the first image

Parameters:	C_x	C_y	R_x	R_y	E_{Area}	E_{Angle}
1	1251.7	969.44	147.13	121.64	56225	1.06
2	1241.4	971.68	120.03	109.86	41427	0.95
3	1250.9	963.24	148.74	119.24	55719	0.90
4	1242.9	974.86	145.32	136.85	62477	0.92
5	1244.8	967.56	136.01	119.99	51270	1.15
6	1247.3	960.28	138.59	122.31	53253	1.09
7	1243.7	973.21	148.87	130.52	61043	1.13
8	1252.0	970.23	142.19	122.82	54864	1.10
9	1240.9	965.24	133.73	151.12	48365	1.15
10	1244.3	966.35	128.35	113.45	45746	1.22
11	1246.1	968.93	135.27	121.02	51429	1.07
12	1246.5	968.39	143.76	125.84	56834	1.18
13	1241.8	976.00	151.4	1.34.24	63833	1.11
14	1243.7	967.75	129.66	117.47	47850	1.22
15	1247.6	964.61	135.97	122.6	52370	1.06
Average	1245.7	968.51	139.00	122.2	53514	1.06

Parameters:	C_x	C_y	R_x	R_y	E_{Area}	E_{Angle}
Sigma	3.6112	4.3043	8.8818	7.3645	6235.5	0.10
Max	1251.8	975.95	151.36	136.85	63833	1.22
Min	1240.9	960.28	120.03	109.86	41427	0.90
Software	1245.2	975.19	144.72	134.86	61314	1.14
Sigma from average	0.1366	1.5508	0.6442	1.7193	1.2510	0.5840
Overfits physician boundary	-	-	-	-	-	-
Overfits physician average	-	1	1	1	1	1
4th physician sigma from average	0.94	1.72	0.70	2.59	1.70	2.26
Excluding 4th physician						
Sigma from average	0.19	1.75	0.68	2.15	1.42	0.51
Overfits physician boundary	-	-	-	1	-	-
Overfits physician average	-	1	1	1	1	1

Table A2. Analysis data for the second image

Parameters:	C_x	C_y	R_x	R_y	E_{Area}	E_{Angle}
1	793.95	1086.4	165.86	150.26	78295	0.42
2	796.2	1090.9	167.78	147.15	77562	0.33
3	797.65	1090.1	164.31	147.13	75947	0.63
4	795.05	1078.3	186.02	171.34	100131	0.70
5	798.36	1090.9	165.03	150.49	78023	0.76
6	799.24	1090.7	167.36	158.27	83215	0.33
7	794.49	1084	184.66	169.78	98494	0.71
8	799.15	1085.8	176.3	163.94	90800	0.50
9	795.05	1082.3	169.37	152.02	80889	0.61
10	802.2	1090.6	161.64	150.59	76471	0.40
11	792.04	1080.5	185.11	164.71	95785	0.71
12	797.36	1087.4	167.35	157.36	82731	0.64
13	795.29	1092	169.87	149.64	79857	0.44
14	799.4	1091.4	163.85	149.17	76785	0.36

Parameters:	C_x	C_y	R_x	R_y	E_{Area}	E_{Angle}
15	797.57	1089.9	163.8	148.38	83423	0.48
Average	796.87	1087.4	170.55	155.35	83423	0.54
Sigma	2.6238	4.3454	8.3438	8.3466	8541	0.15
Max	802.21	1091.6	186.02	171.34	100131	0.76
Min	792.04	1078.3	161.64	147.13	75948	0.60
Software	801.92	1086	184.68	171.54	99525	0.60
Sigma from average	1.93	0.32	1.69	1.94	1.89	0.42
Overfits physician boundary	-	-	-	1	-	-
Overfits physician average	1	-	1	1	1	1
4th physician sigma from average	0.72	2.55	2.13	2.26	2.30	1.14
Excluding 4th physician						
Sigma from average	1.84	0.55	2.05	2.36	2.32	0.51
Overfits physician boundary	-	-	-	1	1	-
Overfits physician average	1	-	1	1	1	1

Table A3. Analysis data for the third image

Parameters:	C_x	C_y	R_x	R_y	E_{Area}	E_{Angle}
1	722.49	1127.3	141.74	127.56	56801	0.57
2	723.34	1129.7	147.52	134.3	62227	0.67
3	719.44	1124.8	142.23	130.82	58454	0.67
4	727.9	1128.3	146.54	130.59	60120	0.54
5	722.18	1130	143.42	130.89	58975	0.70
6	722.82	1127.6	143.52	127.36	57424	0.67
7	724.88	1127.9	146.87	131.59	60716	0.58
8	725.66	1125.9	146.01	130.16	59705	0.51
9	721.58	1123.5	147.1	129.86	60012	0.76
10	723.1	1130	142.81	128.21	57522	0.46
11	727.44	1128.9	147.34	129.74	60054	0.70
12	725.84	1127.7	146.46	132.86	61131	0.64

Parameters:	C_x	C_y	R_x	R_y	E_{Area}	E_{Angle}
13	723.29	1127.3	145.26	131.4	59964	0.56
14	725.38	1129.9	149.3	126.79	59478	0.63
15	723.2	1129.8	144.5	129.18	58643	0.71
Average	723.9	1127.9	145.38	130.09	59415	0.63
Sigma	2.2588	2.0084	2.2345	2.0671	1471	0.08
Max	727.86	1130.4	149.32	134.27	62227	0.76
Min	719.44	1123.5	141.74	126.79	56801	0.46
Software	726.83	1141.6	126.12	120.52	47752	0.00
Sigma from average	1.30	6.80	8.62	4.63	7.93	1.30
Overfits physician boundary	-	1	1	1	1	-
Overfits physician average	1	1	-	-	-	-
4th physician sigma from average	1.98	0.25	0.62	0.47	0.74	1.05
Excluding 4th physician						
Sigma from average	1.57	6.58	8.36	4.45	7.67	7.51
Overfits physician boundary	-	1	1	1	1	1
Overfits physician average	1	1	-	-	-	-

Table A4. Analysis data for the fourth image

Parameters:	C_x	C_y	R_x	R_y	E_{Area}	E_{Angle}
1	2245.8	1044.9	144.93	123.41	56190	1.51
2	2242.1	1042.4	145.65	122.63	56112	1.53
3	2243.8	1042.6	142.92	120.54	54122	1.55
4	2233.4	1042.7	164.79	151.68	78525	-1.17
5	2243.8	1043.3	143.51	122.94	55427	1.54
6	2244.1	1045.2	145.07	121.59	55415	1.47
7	2244	1045.9	143.24	122.2	54990	1.36
8	2243	1040.8	154.43	139.76	67805	-1.57
9	2242.1	1043	145.25	121.27	55337	1.44
10	2244	1044.6	142.64	119.39	53501	1.51

Parameters:	C_x	C_y	R_x	R_y	E_{Area}	E_{Angle}
11	2244.7	1043.6	147.49	121.89	56478	1.49
12	2245.9	1036.5	156.04	126.83	62174	-1.55
13	2241.7	1043.4	143.4	118.13	53418	-1.56
14	2243.6	1041.9	146.62	121.78	56094	1.52
15	2244.1	1043.1	143.7	120.45	54377	1.48
Average	2243.1	1042.9	147.35	124.97	57998	0.70
Sigma	2.9349	2.2179	6.2513	8.9366	6795.4	1.36
Max	2245.9	1045.9	164.79	151.68	78525	1.55
Min	2233.4	1036.5	142.64	118.13	53418	-1.57
Software	2240.6	1047.4	158.13	147.85	73449	-1.43
Sigma from average	0.84	2.02	1.72	2.56	2.27	1.57
Overfits physician boundary	-	1	-	-	-	-
Overfits physician average	-	1	1	1	1	-
4th physician sigma from average	8.73	0.12	4.35	5.27	5.45	1.47
Excluding 4th physician						
Sigma from average	2.53	1.94	2.92	4.75	4.37	1.75
Overfits physician boundary	1	1	1	1	1	-
Overfits physician average	-	1	1	1	1	-

Table A5. Analysis data for the fifth image

Parameters:	C_x	C_y	R_x	R_y	E_{Area}	E_{Angle}
1	861.02	1119.1	142.96	133.72	60057	1.51
2	864.13	1119.9	144.85	130.05	59181	-1.51
3	866.13	1121.1	141.17	128.47	56976	-1.39
4	867.17	1117	146.274	132.38	60819	-1.47
5	870.99	1121.9	143.73	141.56	63920	0.01
6	867.32	1120.3	144.83	128.21	58335	-1.55
7	863.26	1122.4	141.57	132.68	59010	1.53
8	861.79	1118.7	151.08	137.83	65419	1.24

Parameters:	C_x	C_y	R_x	R_y	E_{Area}	E_{Angle}
9	864.4	1114.6	147.87	126.71	58863	1.44
10	867.15	1120.1	144.54	125.26	56879	-1.50
11	864.2	1117.1	150	128.92	60752	1.35
12	861.69	1120	149.32	134.39	63043	1.38
13	863.15	1118.7	145.34	129.51	59134	1.55
14	865.39	1121.1	145.16	128.46	58582	-1.55
15	864.46	1118.2	143.62	129.76	58547	-1.52
Average	864.82	1119.3	145.49	131.19	59968	-0.03
Sigma	2.6338	2.0615	2.9446	4.3276	2459.4	1.47
Max	870.99	1122.4	151.08	141.56	65419	1.55
Min	861.02	1114.6	141.17	125.26	56879	-1.55
Software	872.27	1123.3	158.32	156.36	77770	0.87
Sigma from average	2.83	1.92	4.36	5.82	7.24	0.62
Overfits physician boundary	1	1	1	1	1	-
Overfits physician average	1	1	1	1	1	1
4th physician sigma from average	0.90	1.18	0.24	0.26	0.32	1.15
Excluding 4th physician						
Sigma from average	2.88	1.86	4.23	5.64	7.03	0.55
Overfits physician boundary	1	1	1	1	1	-
Overfits physician average	1	1	1	1	1	1

Table A6. Analysis data for the sixth image

Parameters:	C_x	C_y	R_x	R_y	E_{Area}	E_{Angle}
1	2303	978.6	158.3	153.4	76302	-0.96
2	2302	975.6	156.7	150.6	74148	0.31
3	2303	977	159.4	155.7	77985	-1.13
4	2305	977	163.1	158.4	81199	-0.61
5						
6	2303	978.5	159.3	154.1	77126	-1.27

Parameters:	C_x	C_y	R_x	R_y	E_{Area}	E_{Angle}
7	2306	978.8	160.4	155.5	78378	-0.96
8	2305	977.5	160.5	154.6	77939	-0.88
9	2304	973.6	168.9	153.9	81627	-1.31
10	2304	976	161.3	154.3	78186	-0.93
11	2304	977.7	156	151.4	74199	-1.12
12	2306	974.5	164.3	156.1	80543	-1.14
13	2304	976.3	165.7	154.7	80532	-0.91
14	2306	979.3	153.22	145.12	69854	-1.10
15						
Average	2304	977	160.5	153.7	77540	-0.92
Sigma	1.261	1.711	4.208	3.249	3.329	0.41
Max	2306	979.9	168.9	158.4	81627	0.31
Min	2302	973.6	153.2	145.1	99854	-1.31
Software	2310	982.6	158	156.3	77543	-0.62
Sigma from average	4.282	3.306	0.614	0.792	0.001	0.74
Overfits physician boundary	1	1	-	-	-	-
Overfits physician average	1	-	-	1	1	-
4th physician sigma from average	0.68	0.03	0.57	1.60	1.12	3.15
Excluding 4th physician						
Sigma from average	4.26	3.17	0.55	0.97	0.09	0.79
Overfits physician boundary	1	1	-	1	-	-
Overfits physician average	1	1	-	1	1	1

Annex B. Parameters of Thermal Camera

Table B7. Thermal camera ThermaCamTM – T400 specification

Video and optics data	Angle of view	25° x 18.75°
	Minimal focusing distance	0.4 m (1.31 ft)
	Focal length	18.04 mm (0.710 inch)
	IFOV (thermal resolution)	1.36 mRad
	Lens identification	Automatic
	Aperture	1.3
	Thermal sensitivity	<0.08 ⁰ C (<0.17 ⁰ F) @ + 30 ⁰ C (+86 ⁰ F)
	Frame rate	Depends on geographical location: <ul style="list-style-type: none"> • 9Hz • 30Hz
	Focusing	Automatic or manual
Detector	Detector type	Uncooled focal plane array microbolometer
	Spectral interval	7.5–13 μm
	Resolution	320 by 240 pixels
	Display	3.5“ (inch) (320 by 24 pixels)
	Display type	Touch LCD
	Colour depth	16K colours
	Aspect ratio	3:2
Video	Camera resolution	1.3Mpixels
	Video focusing	Predefined
	Video format	5:4
	Video frame rate	10 Hz
	Video colour depth	24 bits
	Illumination	1000 cd

Annex C. Lesion Area Dynamics With Respect to Time

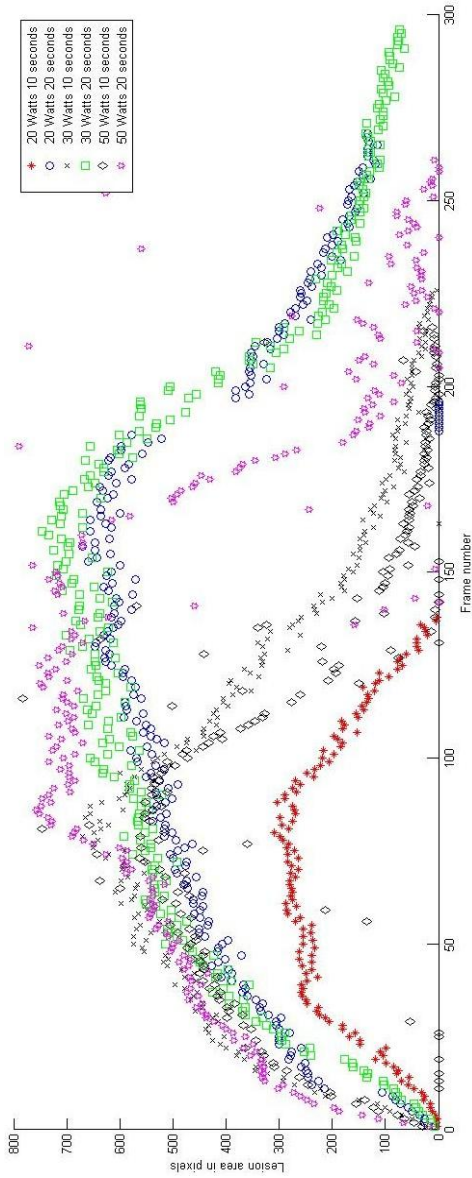


Fig. C1. Pulmonary vein lesion area dynamics with respect to time

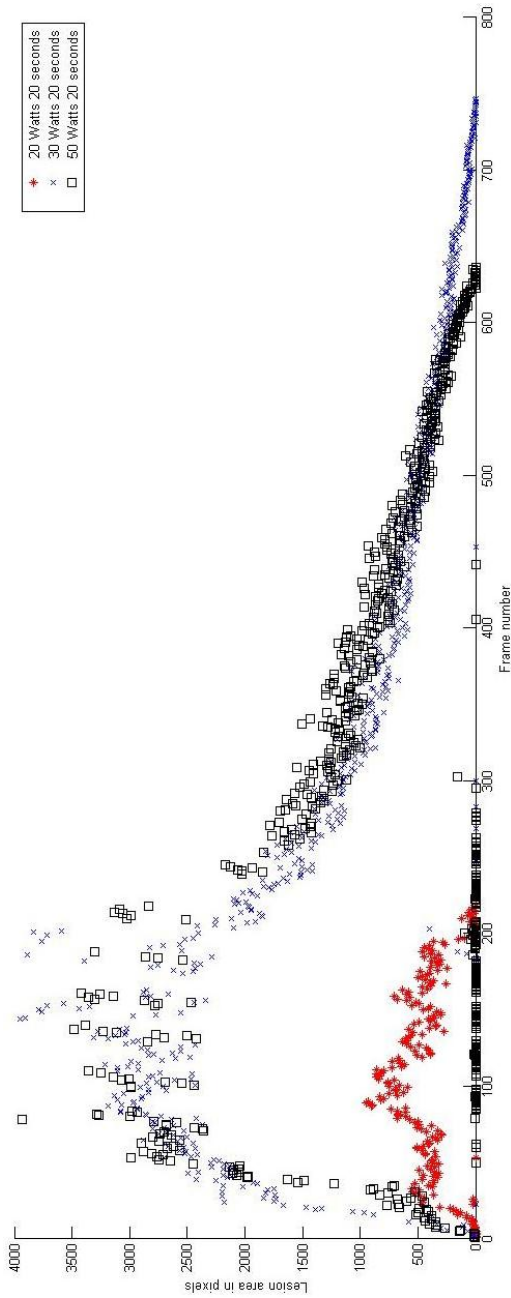


Fig. C2. Atria tissue lesion area dynamics with respect to time

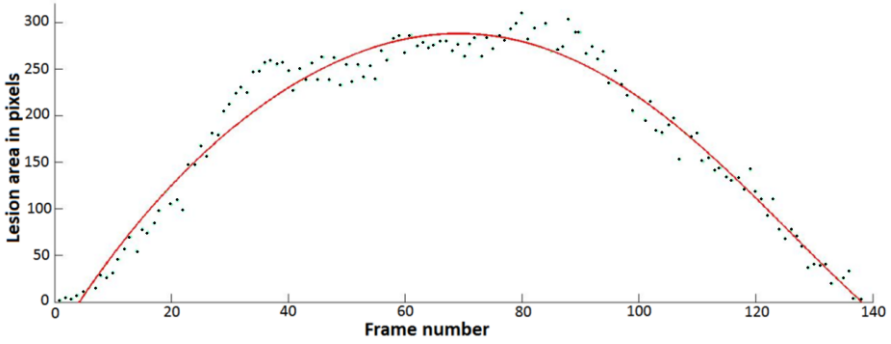


Fig. C3. Approximation of data points by a cone.
Case: pulmonary vein; parameters: 20 Watts 10 seconds

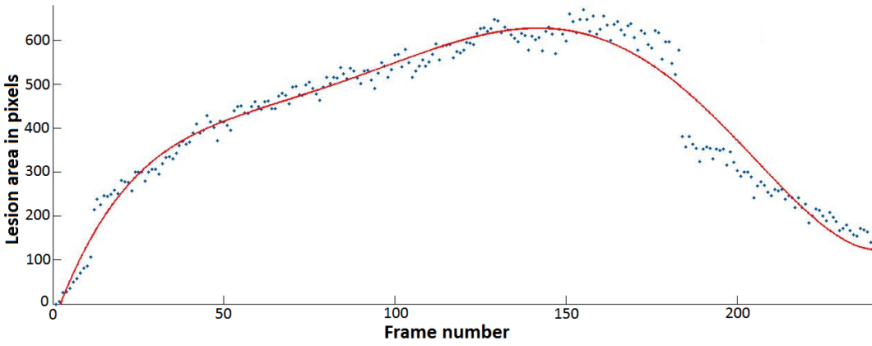


Fig. C4. Approximation of data points by a cone.
Case: pulmonary vein; parameters: 20 Watts 20 seconds

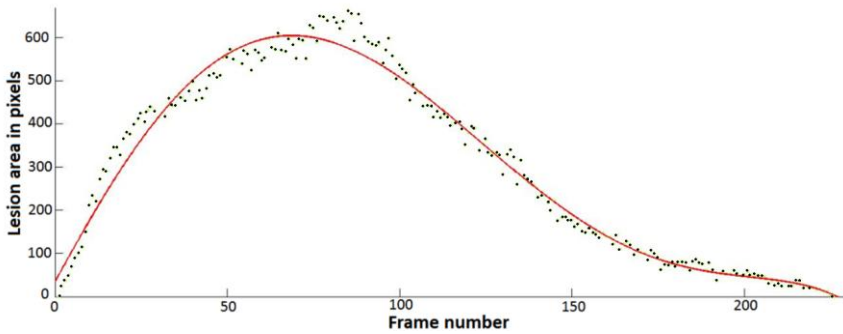


Fig. C5. Approximation of data points by a cone.
Case: pulmonary vein; parameters: 30 Watts 10 seconds

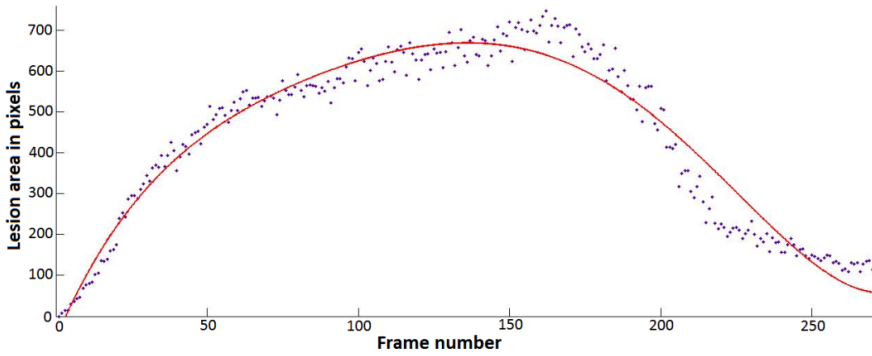


Fig. C6. Approximation of data points by a cone.
Case: pulmonary vein; parameters: 30 Watts 20 seconds

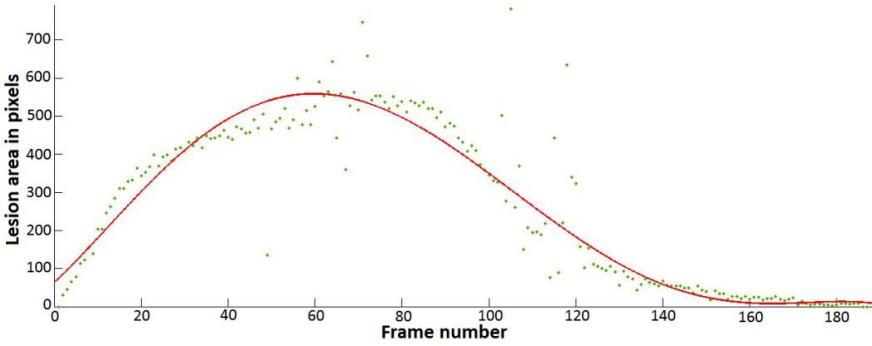


Fig. C7. Approximation of data points by a cone.
Case: pulmonary vein; parameters: 50 Watts 10 seconds

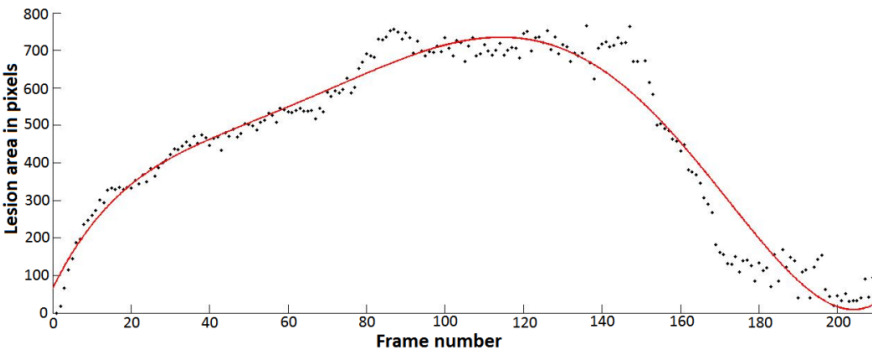


Fig. C8. Approximation of data points by a cone.
Case: pulmonary vein; parameters: 50 Watts 20 seconds

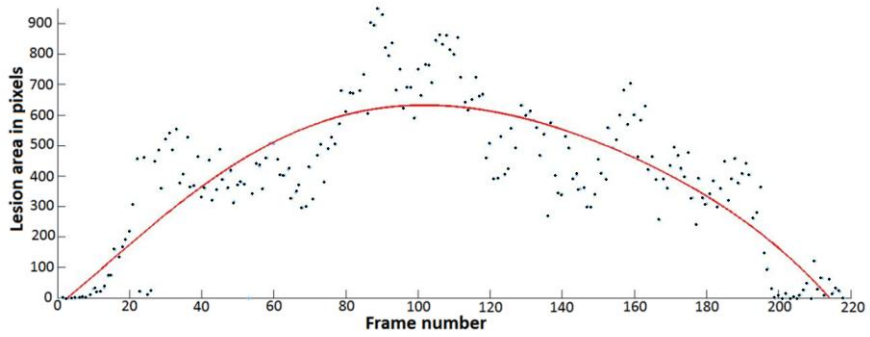


Fig. C9. Approximation of data points by a cone.
Case: atria; parameters: 20 Watts 20 seconds

Povilas TREIGYS

DEVELOPMENT AND APPLICATION OF METHODS
IN THE GRAPHICAL OPHTHALMOLOGICAL AND THERMOVISUAL
DATA ANALYSIS

Doctoral Dissertation

Technological Sciences,
Informatics Engineering (07T)

Povilas TREIGYS

GRAFINIŲ OFTALMOLOGINIŲ IR TERMOVIZINIŲ DUOMENŲ
ANALIZĖS METODŲ KŪRIMAS IR TAIKYMAS

Daktaro disertacija

Technologijos mokslai,
Informatikos inžinerija (07T)

2010 03 24. 11,5 sp. I. Tiražas 30 egz.
Vilniaus Gedimino technikos universiteto
leidykla „Technika“, Saulėtekio al. 11,
10223 Vilnius, <http://leidykla.vgtu.lt>
Spausdino UAB „Biznio mašinų kompanija“,
J. Jasinskio g. 16A, 01112 Vilnius